ATOMISTIC STUDY OF THE STRUCTURE, THERMODYNAMICS, AND MORPHOLOGICAL EVOLUTION OF URANIUM-ZIRCONIUM ALLOYS

A Dissertation
Presented to
The Academic Faculty

by

Alex Moore

In Partial Fulfillment
of the Requirements for the Degree
Doctor of Philosophy in the
School of Mechanical Engineering

Georgia Institute of Technology
August 2016

ATOMISTIC STUDY OF THE STRUCTURE, THERMODYNAMICS, AND MORPHOLOGICAL EVOLUTION OF URANIUM-ZIRCONIUM ALLOYS

Approved by:

Dr. Chaitanya S. Deo, Advisor
School of Mechanical Engineering
Georgia Institute of Technology

Dr. Yan Wang
School of Mechanical Engineering
Georgia Institute of Technology

Dr. Weston M. Stacey, Jr.
School of Mechanical Engineering
Georgia Institute of Technology

Dr. Hamid Garmestani
School of Material Science and Engineering
Georgia Institute of Technology

Dr. David L. McDowell
School of Mechanical Engineering
Georgia Institute of Technology

Date Approved: [April 28, 2016]

CONTENTS

ACKNOWLEDGEMENTS

Many thanks to Idaho National Laboratory (INL), the Domestic Nuclear Detection Office (DNDO), the Department of Energy Nuclear Energy University Program (DOE-NEUP), and the National Science Foundation (NSF) for their financial support. Thank you to my family and friends for their continued support.

LIST OF TABLES

Page

LIST OF FIGURES

Page

SUMMARY

Metallic uranium alloys are considered a promising nuclear fuel for the new generation of fast reactors. Metallic alloys have advantages over the traditional ceramic nuclear fuels in the areas of thermal conductivity, burn-up, ease of fabrication, favorable plutonium breeding efficiency, fuel-recycling, and other thermo-physical and neutronic properties. However, metallic fuels undergo various physical phenomena whose fundamental processes are unexplained. One such phenomenon is the complex microstructure and phase separation following fabrication and irradiation of the metallic fuels. In order to help understand the complex microstructure, atomistic simulations were conducted on U-Zr alloys, a promising option for the new generation of metallic fuels, to investigate their structure, thermodynamics, and microstructure evolution.

A semi-empirical modified embedded atom method (MEAM) potential was developed for application to the high temperature body-centered-cubic uranium-zirconium alloy (γ-U-Zr) phase. The potential was constructed to ensure that the basic properties (e.g. elastic constants, bulk modulus, and formation energies), the thermal properties (e.g. thermal expansion, Vegards law, and melting point), and the mixing thermodynamics (e.g. enthalpy of mixing) were in agreement with first principles calculations and experimental results. The potential was then used to examine some of the high temperature thermodynamics and structure, and was able to obtain new values for the isothermal compressibility, adiabatic index, and the Grüneisen parameters for the U-Zr phase at temperature.

In many metallic alloys, complex microstructures form as a consequence of local atomic ordering that depends on the processing path. This research uses an atomistic approach to study microstructural morphology and evolution by investigating how temperature and alloy concentration affect ordering behaviors that lead to observed microstructures. Atomic simulations conducted with the MEAM potential show the thermodynamic driving force to the lamellar structure for the melt-casted U-rich alloys and the finely acicular microstructure for the water-quenched U-rich alloys. In addition, when the U-rich U-Zr alloy is equilibrated at a lower temperature, the lamellar/acicular microstructures begin to spheroidize, as observed in experiments. In the intermediate Zr concentration region, the ordering seen is able to facilitate the structure to the partially ordered δ-UZr_2 phase seen experimentally. Lastly, the Zr-rich region is able to successfully show the thermodynamic driving force to the acicular, Widmanstätten, and martensitic needles type microstructures observed experimentally. These simulations are able to successfully replicate some of the fundamental thermo-physical and microstructural characteristics following fabrication and irradiation of the U-Zr metallic fuels.

Lastly, a sensitivity analysis of the modified embedded atom method (MEAM) potential was performed in order to examine and understand the uncertainty in the parameters and formalism of the interatomic potential. The sensitivity analysis was conducted using one-at-a-time (OAT) sampling of the parameters and how they affected the ground state, thermal, and alloy structural and thermodynamic properties. The performed analysis was able to uncover the properties that can be easily varied or adjusted like the lattice constant, and the properties that had little variance like the heat

capacity. The observed analysis on the ground state properties was found to correspond well with previously published results, after which the thermal and alloy properties were examined. A new method of categorizing changes in the alloy properties was developed that allows for the discrimination of bonding behaviors, determining if the strength of the bonding between atoms changed or if the manner in which they were bonded together changed.

CHAPTER 1

INTRODUCTION

Since the Clementine reactor in 1949, the first nuclear fast reactor, metallic alloy fuels have been of interest to the nuclear community, and a number of experimental fast reactors have employed nuclear metallic fuel, including the Experimental Breeder Reactor (EBR) series, the Los Alamos Molten Plutonium Reactor Experiment (LAMPRE) series, the Dounreay Fast Reactor (DFR), and the Fermi reactors [1].

Generally ceramic nuclear fuel is used in the Light Water Reactors (LWR) and Pressurized Water Reactors (PWR); however, recently there has been increased research in using metallic fuels in a LWR [2]. Metallic fuels have already been shown to have many benefits when used in non-water cooled reactors. Metallic alloys have advantages over the conventional ceramic nuclear fuels in the areas of thermal conductivity, burnup, ease of fabrication, favorable plutonium (Pu) breeding efficiency, fuel-recycling and other thermo-physical and neutronic properties [3, 4]; yet, recently they are being noticed for additional significant benefits. Metal alloy fuels demonstrate superior performance over ceramic fuels in that they behave in a benign manner during core off-normal events, maintain integrity in high burn-up conditions, have low-loss fuel recycling during reprocessing, have proliferation-resistant recycling, and have passive reactor safety feedback mechanisms [1, 5]. However, metallic fuels undergo various physical phenomena whose fundamental processes are poorly understood, such as fuel solid/gaseous fission swelling, constituent redistribution, fuel-cladding interactions and phase separation during fabrication.

Metallic Fuel Advantages

Nuclear metallic alloy fuels are believed to have a very promising future in the new advanced fast reactor designs and research for several reasons. First, they do not require plutonium to be separated during reprocessing, which is a benefit in regard to national security threats. One of the largest concerns for nuclear national security is terroristic efforts to obtain material in order to create a nuclear device. However, the metallic fuel reprocessing, as opposed to ceramic fuel reprocessing, would ensure that key isotopes and elements required for a supercritical nuclear device would not have to be separated from the bulk and therefore could not be a target or opportunity for terroristic efforts. Another benefit is that reprocessing of metallic fuel allows for reduced fuel cycle cost.

Secondly, the metallic fuels have the potential for the highest fissile atom density, resulting in a higher burn-up potential of nuclear fuel. This would allow reactors to operate longer before refueling; create an opportunity to breed more plutonium during reactor operation, resulting in high utilization of fuel resources; and allow for smaller reactors with a high power density.

Third, nuclear metallic alloy fuels have favorable thermodynamic properties, promoting safety and energy harvesting. They have a high thermal conductivity leading to lower fuel and cladding temperatures and less stored energy.

Metallic fuels also have favorable neutronic properties. At the reactor operating conditions, many of the metallic fuels are in the body-centered-cubic (bcc) phase, resulting in very isotropic neutron cross-sections, which are particularly important for small fast nuclear reactors.

Lastly, metallic fuels have passive safety features during core off-normal events. For example, during a loss-of-flow accident, fission gases and thermal expansion cause the fuel to expand to the cladding, whereupon the fuel at the fuel/cladding interface will transform to the molten phase, removing reactivity from the core.

There are some drawbacks to the use of metal alloy nuclear fuels as well. They have high fission gas release and swelling during irradiation and a lower melting point than the traditional ceramic nuclear fuels. They can also react with water. Nonetheless, some of these disadvantages have actually been realized to be beneficial, such as the low melting point. The low melting point allows for the fuel to go into the molten phase, which reduces reactor reactivity, acting as a passive safety feature (this process is described further in the Fuel Disadvantage Section below).

Metallic Fuel Disadvantages

Each nuclear fuel type has its advantages and disadvantages, and no single fuel type will perform better than the others in all scenarios. There are a few concerns that need to be considered when using metallic fuels in particular, such as fuel swelling, fission gas release, fuel redistribution, cladding interactions, coolant interactions, and complex microstructures.

Fuel swelling and irradiation growth are drastic phenomena that metallic fuels undergo when irradiated. Swelling in the fuel means that the fuel maintains a similar shape but the volume increases, while irradiation growth means a change in shape with no noticeable change in volume. At the onset of operation, metallic fuels will swell rapidly due to fission gas bubbles, until the bubbles become interconnected and make a path for the gas to escape. After the bubbles are interconnected, the swelling behavior of metallic fuels is very slow and is caused by the solid fission products taking up lattice positions in the fuel. The addition of the solid fission

product accumulation leads not only to slow swelling, but also to a loss in thermal conductivity. Furthermore, grain boundary tearing at the fuel edges has been seen to cause large irregular shaped cavities. Both the irradiation growth and grain boundary tearing are known to result in reactivity loss [6].

The fuel cladding mechanical interaction (FCMI) is a large concern when using metallic fuels. As irradiation of the fuel progresses, the irradiation/thermal creep by fission gas pressure loading can eventually cause a stress-rupture of the cladding [6, 7]. Until the 1960's, the burn-up of the metallic fuels in fast reactors was limited by the FCMI (Ogata 1996). A technical breakthrough from Argonne National Laboratory (ANL) drastically decreased the FCMI and allowed the burn-up potential of the metallic fuels to be realized [8]. Reducing the smear density down to approximately 75% provided enough space for the fuel to swell inside the cladding until the fission gas pores became interconnected and fuel swelling due to fission gasses stopped.

Fuel-cladding chemical interactions (FCCI) must also be considered when using metallic fuels. The creep rupture at high burn-up is known to be accelerated by FCCI. Experiments have shown that there is fuel-cladding interdiffusion, in which uranium, plutonium, and some lanthanide fission products react and can penetrate into the cladding. The result of this interdiffusion is cladding wall thinning, a brittle cladding layer between the fuel and cladding, and a eutectic composition approached in the fuel which causes a lower melting point in that region [6, 9, 10].

Another concern when using metallic fuels is the fuel constituent restructuring of uranium and zirconium that has been experimentally witnessed in the U-Zr type metallic fuels. The uranium and zirconium redistribution occurs soon after reactor operation begins from U and

Zr interdiffusion. However, the inhomogeneity associated with the restructuring, while changing some of the mechanical and neutronic properties of the fuel, has not noticeably affected the overall fuel lifetime, but a lowered solidus temperature has been noticed in some fuel regions [6, 11].

All nuclear metallic fuels have a lower melting temperature than the nuclear ceramic fuels. The solidus temperature for uranium metals can be increased when alloyed to another metal with the same bcc high temperature phase. Common metals alloyed to uranium are zirconium, niobium, and molybdenum. For reactor operation the fuels must be kept below their melting temperature. However, since the thermal conductivity of these metallic fuels is higher than that of the ceramic fuels, the heat flux from the fuel pin is higher, which leads to a lower temperature gradient across the fuel pin and allows for a high power density to be achieved while remaining below the fuel melting temperature. Nevertheless, this low melting temperature can cause problems during fast transients.

Depending on the fuel temperature and the zirconium redistribution, the fuel could have multiple phases during reactor operation, causing changes in both mechanical and neutronic properties.

The swelling and low melting point of metallic fuels is a benefit during off-normal core events. The interconnected porosity of swollen metallic fuel coupled with the low melting point during a transient event allows for the thermal expansion of the fuel due to temperature induced phase transformations; this phase transformation prevents the fuel from stressing the cladding, and allows the fuel to flow onto itself in the open porosity [12].

Metallic alloy fuel microstructure tends to be much more complex than ceramic. Depending on the processing path undergone, drastically different phases and precipitate morphologies may be present (this is described further in the Uranium-Zirconium Microstructures Fuel Section below).

However, the metallic fuels still need additional research before they can be fully understood. One of the barriers obstructing the advancement of metallic fuels is the lack of appropriate tools needed for computational simulations. Computational simulation is a tool that can be used to give insight into physical phenomena, as well as give understanding to the atomistic mechanisms that result in the overall mechanical and thermal properties of the system. Computational simulation not only gives insight into experimental results, but also, once developed, allows for the necessary predictions of metallic fuel property changes under a variety of conditions. In addition, computational simulation combined with experimentation will not only assist in the operation and design of a reactor, but also provide the necessary information and comprehension for optimizing fabrication and reprocessing of the fuels.

Uranium (U)

Uranium is an actinide that has three distinct stable solid phases. The transition of these phases can be attributed to the behavior of the de-localized f-orbital-electrons. The ground state uranium phase is the α (orthorhombic) phase. As temperature increases, uranium will go through transitions to the β (tetragonal) and the γ (body-centered-cubic) phases respectively. The α and β phases of uranium have unwanted an-isotropy of expansion, but the γ phase has seemingly isotropic expansion which is desirable in reactor environments. The transition temperatures of

uranium from α to β, β to γ, and γ to liquid are 940.85 K ± 1.3 K, 1047.95 K ± 1.6 K, and 1405.95 K ± 0.8 K respectively [13].

Zirconium (Zr)

Zirconium is also a transition metal and has two distinct solid phases. The ground phase of zirconium is hexagonally closed-packed (hcp or α-Zr), while the high temperature phase is body-centered-cubic (bcc or β-Zr). The transition temperature from α-Zr to β-Zr occurs at 863 °C. Another important characteristic of zirconium is its high melting point of 1855 °C, which makes zirconium useful when alloying to uranium, as it raises the melting point of the alloy.

Uranium-Zirconium (U-Zr)

Zirconium is one of the principal structural metals for fuel cladding and other core components because of its high temperature bcc phase (above 865 ºC), high melting temperature, very low thermal neutron absorption cross-section, relatively low cost, and high fission product yield. For these reasons it was considered a good option to alloy with uranium to construct a metallic alloy fuel. However, the choice of which element to alloy to uranium for a good metallic fuel has mostly been decided by trial and error, often making a compromise between mechanical properties and corrosion resistance. After many experiments and tests, uranium-zirconium (U-Zr), along with a few other alloys, appears to be a promising option as a nuclear fuel for fast reactors.

A detailed history of the use of U-Zr based alloys as fuel for fast reactors is provided by Carmack et al. [9] and by Hofman and Walters [3]. As described by Carmack et al. [9], the early

U.S. fast reactor designs favored metal alloy fuel due to its high fissile density and compatibility with sodium. Furthermore, it was discovered that the low smear density of the metallic fuel facilitated the operation at much higher burnup [9]. Metal fuel was selected for use in many of the first reactors in the U.S., including the EBR-I and the EBR-II in Idaho, the FERMI-I reactor, and the DFR in the U.K. [1, 8, 9]. Metallic U–Pu–Zr alloys were the reference fuel for the U.S. Integral Fast Reactor (IFR) program. An extensive database on the performance of advanced metal fuels was generated as a result of the operation of these reactors and the IFR program. First generation (often called Mark-I in the literature [9]) fuel was unalloyed, highly enriched uranium metal that was rolled and swaged to the desired final shape. The second (Mk-II) and third (Mk-III) core loadings of EBR-I were centrifugally cast U–Zr alloy and centrifugally cast U–Zr alloy coextruded with Zircaloy-2 cladding, respectively. The EBR-II operational and fuel qualification data includes the irradiation of over 30,000 Mk-II driver fuel rods [14, 15], 13,000 Mk-III/IIIA/IV (U–10Zr alloy) driver fuel rods, and over 600 U–Pu–Zr fuel rods [1, 7] from 1964 to 1994. Thus, it can be seen that the U-Zr alloy system is of integral interest to fast reactor fuel development, both as an early fuel for these reactors and as the main component of advanced (U-Pu-Zr) fuel designs. In this paper, the thermodynamics of the entire U-Zr alloy system is studied; however the fuel forms are generally fabricated from high U content alloys (e.g., U-10%Zr).

Uranium-zirconium has a bcc structure for reactor operating temperatures; therefore, the bcc structure is particularly important to analyze. It is also important to note that the uranium-zirconium alloy goes through a δ (C32 crystal structure) to γ (bcc) phase transition for 65%-75% zirconium around 890 K.

In 1955, Summers-Smith [16] presented a phase diagram for the U-Zr alloy system as well as measurements of lattice constants of quenched alloys. While the phase diagram has been modified significantly since then, several researchers [17-19] have reproduced the lattice constants.

Thermodynamics of the γ-U-Zr bcc alloy was investigated by experimental and computational techniques. Fedorov and Smirnov [20, 21] used an electrochemical cell to estimate the experimental electromotive force (emf) values, heat capacity, and the molar enthalpy and entropy of mixing of the high temperature γ-phase of the U-Zr system. In 1981, Chiotti et al. [22] used the emf values and heat capacities obtained from Fedorov to construct the Gibbs energy of mixing and enthalpy of mixing for the high temperature U-Zr solid solution. Kanno et al. [23] used the Knudsen effusion mass-spectrometric technique to measure vapor pressures and thermodynamic activities of liquid and solid solutions of U-Zr in the temperature range of 1700 K-1850 K. The molar Gibbs energy was then obtained using the partial molar Gibbs energies and activity coefficients. It can be seen from Chiotti et al. [22] and Kanno et al. [23] that the Gibbs energy of mixing values, and therefore the enthalpy of mixing values, remain relatively similar throughout the stable γ-U-Zr solid solution phase region. Shevchuck et al. [24] estimated the Gibbs energy of mixing from Darken's equation using diffusion data at 1000°C. Leibowitz et al. [25] and Xiong et al. [26] constructed Gibbs energy curves to fit the previous thermodynamic experimental data and phase diagram for the U-Zr system.

The most recent phase diagram was constructed by H. Okamoto [27] and was made from a compilation of experimental papers on uranium-zirconium. Figure 1 shows the binary U-Zr phase diagram.

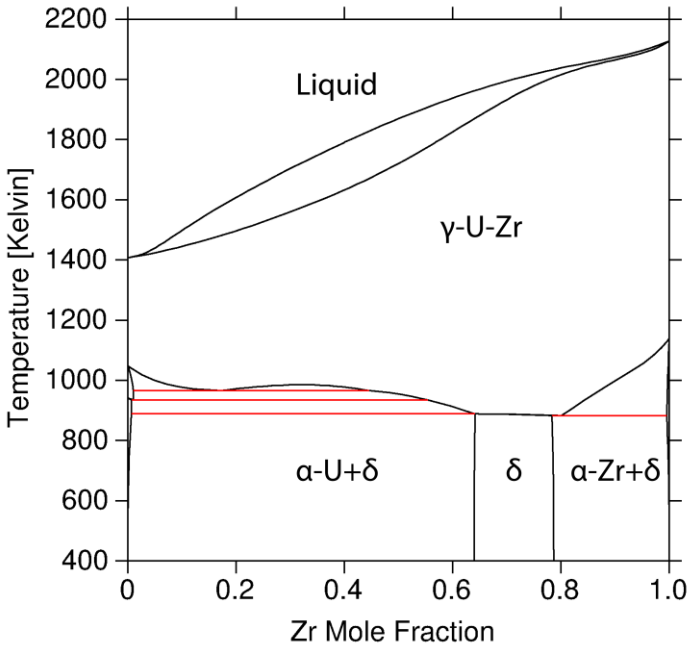

Figure 1**:** Binary U-Zr phase diagram, with important major phase regions indicated, from Thermo-Calc® and the TCBin database [28, 29], which uses the previously published thermodynamics and phase diagrams [27, 30, 31].

The γ-U-Zr phase is the high temperature phase in which the metallic U-Zr fuel has isotropic properties and the main phase of interest for high temperature fast reactors.

Uranium-zirconium (including U-Pu-Zr and U-ZrH) fuel is already considered to be one of the best options for use in the TRIGA pool type reactors and the Generation IV SFR's reactors (EBR-II, SABR, S-PRISM and more). Uranium-zirconium in reactor operating conditions is in the bcc phase. The bcc phase gives the metallic fuel the desired isotropic thermal expansion, but has less experimental data than the lower temperature phases. This research focuses on this bcc metallic phase.

δ-U-ZR_2 Partially Ordered (C32) Phase

The δ-phase of uranium-zirconium is an important phase for non-high temperature conditions. The U-Zr alloy transitions from a δ (partially ordered C32 crystal structure) to γ (bcc) phase around 65%-75% Zr and 890 K. The δ-UZr_2 phase is a modified C32 (AlB_2)-type crystal structure, and is the only stable intermetallic phase in the U-Zr system. This C32 intermetallic crystal structure has been found in a few uranium metallic alloys, such as UZr_2, UHg_2, U_3Si_5, $U_2Ti_{0.82}Zr_{0.18}$, U-Hf, and U_2Ti [18, 32-39]. The δ-UZr_2 phase was proposed to be a modified partially ordered C32 phase by Silcock [40] and Boyko [38] using x-ray diffraction analysis.

Table 1: Structure of the δ-U-Zr crystal system.

Pearson Symbol	hP3
Space Group	P6/mmm
Prototype	Al-B2
Strukturbericht Designation	C32

Uranium-Zirconium Microstructures

Microstructural evolution in metallic alloys involves complex atomic processes occurring over a wide range of temporal and spatial scales. Underlying the evolution of microstructure are unit mechanisms involving atoms or groups of atoms that diffuse in order to satisfy local thermodynamic constraints. Complex microstructures form as a consequence of local atomic ordering that depends on the processing path. An example of such complex microstructure formation is the uranium-zirconium (U-Zr) system, where ordering and phase separation effects are observed and cause microstructures to be highly dependent on processing paths. Figure 2

shows the binary U-Zr phase diagram with important major phase regions indicated. A U-Zr microstructural characteristic is the uranium separation or decomposition from the U-rich U-Zr alloy to form the α-U and δ-UZr_2 phases in various formations. Five representative microstructures are schematically shown in conjunction with the phase diagram.

For example, if the U-rich alloy is air-cooled from the melt, it results in a lamellar microstructure. The same alloy, quenched from the high temperature bcc phase, forms a more acicular structure, while an alloy with a slightly higher Zr concentration, quenched from the miscibility gap, results in spherical decomposition. The lamellar microstructure of U-rich U-Zr alloys has been noticed by Basak et al., McKeown et al., and Kim et al. [41-43]. In each case, this lamellar microstructure formed when the alloy was heated above its melting temperature and then cooled at a modest rate, not quenched [41-43]. However, if the sample was very rapidly quenched, there is evidence that the bcc γ-U phase may hold instead of decomposing [17], and if cooled quickly, may either decompose into α-U and δ-UZr_2 phases or form a supersaturated α'-phase in a Widmanstätten morphology with fine interleaving lamellae [44, 45].

The Zr-rich U-Zr alloys also decompose. Previous publications [46-49] have classified some of the resulting microstructures of this decomposition as acicular, Widmanstätten, disc, globular, rhomboidal, and more complex decompositions. If water-quenched from the bcc solid solution region, the Zr-rich U-Zr can remain in the bcc phase [46, 47] with possible martensitic α-Zr needles or bainitic α-Zr precipitates [46]. However, if air-cooled, Zr-rich alloys result in an acicular decomposition, and if furnace-cooled, in either a Widmanstätten or rhomboidal microstructure after decomposition of the α-Zr [46, 47]. If the sample is annealed in the α-Zr, γ-U-Zr temperature region, either a globular or rhomboidal, or both, α-Zr forms in the δ-UZr_2 phase [46-49].

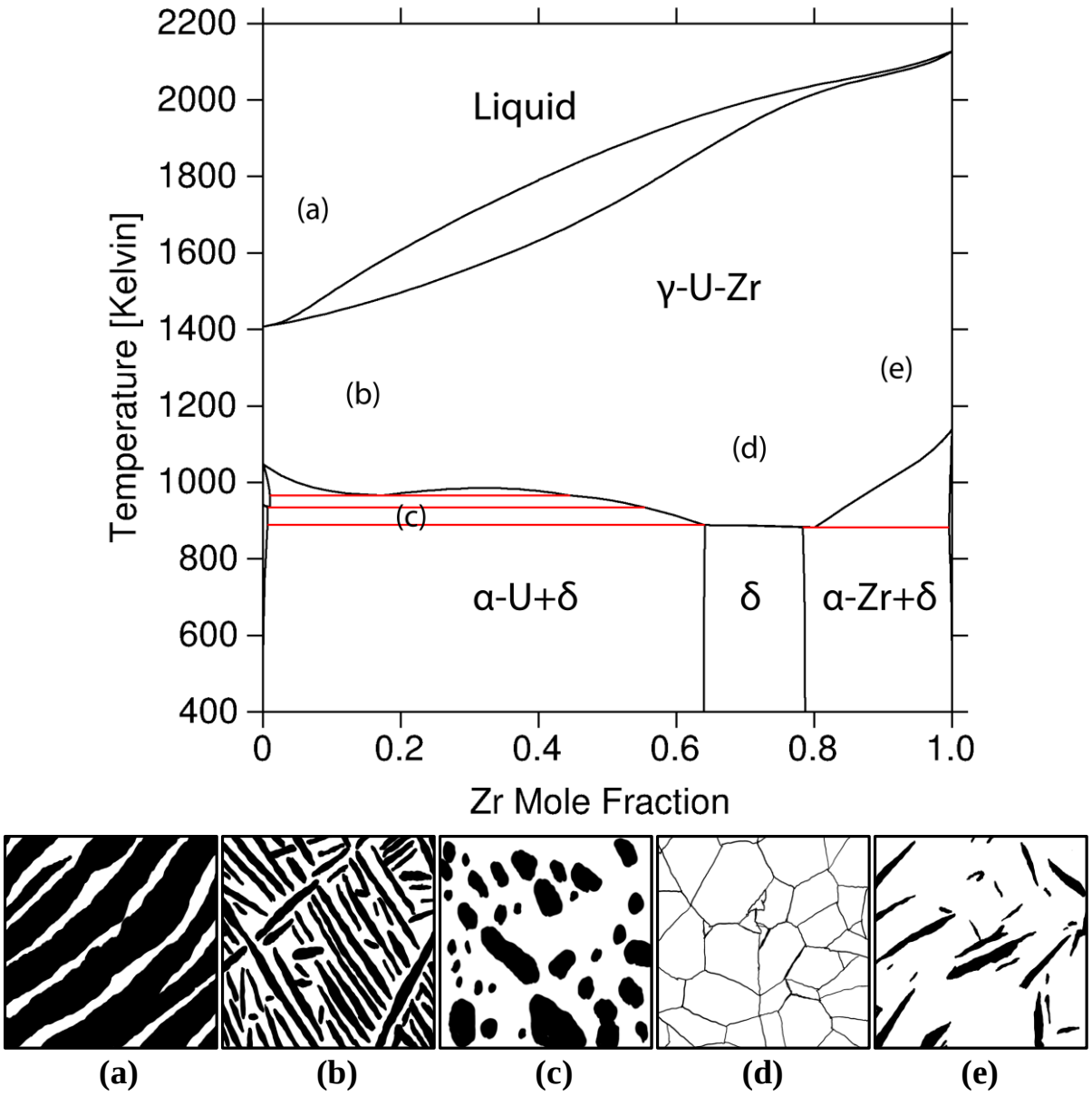

Figure 2: Binary U-Zr phase diagram, with representations of observed microstructures if cooled with a given rate from a temperature range.

(a): (U-rich) melt to low air-cooled: results in lamellar

(b): (U-rich) bcc quenched: results in acicular

(c): (U-rich) α-U, γ-U-Zr phase region quenched: results in spherical decomposition

(d): (Intermediate) bcc quenched: results in equiaxed

(e): (Zr-rich) bcc quenched: results in bcc with martensitic needles

Evidently, atomistic configurations in the bcc and liquid phases, where atomic diffusion is significant, is key in the research of microstructure and morphological evolution of the U-Zr system. Neither U, Zr, nor their alloys lend themselves easily to atomistic analysis.

Using atomistic simulations, we attempt to understand these microstructural effects through analyzing small configurations of U-Zr alloys and looking for thermodynamic driving forces and unit mechanisms of ordering and phase separation. U-Zr interactions are described by a recently developed interatomic potential that is capable of computing several thermodynamic properties of the U, Zr, and U-Zr metals and alloys [50].

Previous U-Zr Simulations

The first published density functional theory (DFT) simulation of the U-Zr system was performed by Landa et al. [51] who employed the Korringa-Kohn-Rostoker method within the atomic-sphere approximation (KKR-ASA) combined with the coherent potential approximation (CPA) in order to investigate the compositional disorder. Effective cluster interactions that were used in the Monte Carlo simulations were obtained using the screened generalized perturbation method (SGPM). The first and second nearest neighbor (hereafter referred to as 1NN, 2NN, ...) effective pair interactions (EPI) obtained by Landa et al. [51] showed significant negative values, indicating a strong tendency of phase separation of the γ-U-Zr system at 0 K.

In 2010, Bozzolo et al. [52] constructed a Bozzolo-Ferrante-Smith (BFS) potential that utilizes the equivalent-crystal theory (ECT) to examine the heat of formation, cohesive energies, and lattice parameters. This is done by utilizing the pure element cohesive energy, the bulk modulus, and the equilibrium lattice parameter, as well as the strain energy, the chemical energy for the compositions, and a reference chemical energy to obtain the formation energy of the system. The parameters needed for the BFS potential were obtained using the Linearized Augmented Plane Wave method (LAPW). The results obtained for 0 K were similar to that obtained by Landa et al. [51]. Then in 2011 and 2012, the BFS potential was used to investigate lanthanide migration and possible cladding interactions [53, 54].

In 2013, Xie et al. [55] and Xiong et al. [26] called into question the enthalpy of mixing obtained by Landa et al. and Bozzolo et al. by showing that the spin orbit-coupling (SOC) and the introduction of the DFT+U significantly changed the enthalpy of mixing and produced better matches to the experimental energetics and thermodynamics.

In 2013, Moore et al. [56] introduced a preliminary bcc U-Zr modified embedded atom method (MEAM) potential; however, it was unable to capture much of the experimental high temperature thermodynamics, and in 2015, Moore et al. [50] published a U-Zr MEAM potential designed to mimic experimental thermodynamics. It successfully replicated the enthalpy of mixing obtained by Chiotti et al. [22], as well as the elastic constants, defect formation energies, lattice constants, thermal expansion values, melting point temperatures, and enthalpy of fusion.

The objective of the current work is to create an atomistic model using the MEAM to describe the structure and thermodynamics of the γ-U-Zr alloys at temperatures where these alloys are stable. Unlike most first principles calculations, interatomic potentials based on

mostly classical descriptions can be used to calculate relevant larger scale atomistic properties at temperature. In comparison to recent literature on the *ab initio* based calculations of U-Zr alloys [26, 51, 55, 57], very few properties of the γ-phase have been calculated at temperature due to its propensity to destabilize at 0 K. Recent calculations often have needed to account for the instability through fixed volume or geometry constraints. The translation of first principles calculations at the ground state to the high temperature phase involve assumptions about structure and thermodynamic equilibria. Direct calculations of the γ-U-Zr phase at temperatures where it is stable are currently not possible through most *ab initio* techniques, due to computational limitations.

The created MEAM potential is the first interatomic potential for the U-Zr system able to describe the γ-U-Zr phase at temperature. The MEAM potential enables atomistic results to be compared to experimental results, allowing the atomistic mechanisms contributing to the experimental results to be witnessed and understood for the first time. The creation of a MEAM potential will allow for the study of the larger scale atomistic simulations of separation/ordering phenomena, defect properties, radiation damage, void/bubble energetics, coalescence, and plasticity. In addition, the MEAM potential can be expanded to include fission products, cladding, and other minor actinides, permitting the study of ternary metallic fuel, fuel-cladding interactions, and how fission products can affect fuel properties.

Semi-empirical interatomic potentials can be fit to both first principles and experimental data and employed to simulate high temperature properties. In classical simulations, atoms are represented by point-like centers, which interact through many-body interactions defined by a set of equations, i.e., the interatomic potential. In that way, the highly complex description of electron dynamics is replaced by an effective model whose main features (such as the hard core

of particles and internal degrees of freedom) are described by a set of parameters and analytical functions, which depend on the mutual positions of the atoms in the configuration. These parameters and functions give complete information about the system energy, as well as about the forces acting on each particle.

Very few interatomic potentials for actinoid metals have been developed. Itinerant f-electron behavior has proved difficult to describe. Directional effects of the electron cloud need to be considered in the potential description. Of the actinoid metals, interatomic descriptions of uranium [56, 58-65] and plutonium atomic interactions are available [66, 67]. Uranium has been described by a charge optimized multi-body (COMB) potential [61], embedded atom method (EAM) potentials [62-64], and a few MEAM potentials [56, 58, 59] which have been developed for various phases of U. The potentials for uranium are often designed to better match a particular U phase or attempt a more inclusive potential by making compromises when fitting properties of the phases. There have also been two previous binary U alloy potentials, U-Mo [64] and U-Al [62], developed using the EAM potential method. In addition, a MEAM potential has been formulated for Pu [67]. This Pu potential has been used to calculate the stability of Pu phases, the phase diagrams of Pu alloys, defect properties, and radiation damage effects [68-76].

The introduction of the many-body EAM potentials [77] allowed a single potential formalism to mimic a wide variety of metals with differing crystal structures as well as oxide, liquid and gaseous phases with reasonable agreement with experimental or first principles simulations [77-82]. However, it was observed that the EAM potentials lead to elastic constants that were inconsistent with experiment when simulating materials with significant directional bonding [83]. Therefore, the MEAM [84] was constructed to simulate the properties of metals with significant directional bonding. These MEAM potentials have been used to investigate a

wide variety of phenomena (e.g., irradiation damage cascades, crystal interfaces, phase and alloy thermodynamics, diffusion, plasticity, etc.) in pure metals and alloys [85-103].

Chapter 2: "Computational Theory and Analysis" describes the simulation methods. A detailed description of the MEAM potential equations and parameters is presented in Chapter 3: "Interatomic Potential" and Chapter 4: "MEAM Parameters". Chapter 5: "Structural Properties of Elemental Phases of U and Zr" describes the structural properties for the U and Zr phases at ground state. In this section, the elemental lattice parameters, elastic moduli, and point defect energies of U and Zr phases are calculated and compared to an extensive literature survey. Chapter 6: "Thermodynamics of Pure Elements" describes the thermodynamics of the pure U and Zr elements, where the heat capacity, melting temperature, and heat of fusion are calculated and compared to reported experimental values. Chapter 7: "BCC and Liquid Phases of U and Zr" uses RDFs and BADFs to examine the thermal structure of the bcc and liquid phases of U and Zr and compare it to previously published results. Chapter 8: "Structural Properties of U-Zr Alloys" describes the structural properties of the γ-U-Zr alloy. In this section, the γ-U-Zr lattice constants and thermal expansion values versus concentration are compared to existing experimental values. Chapter 9: "U-Zr Solid Solution Thermodynamics" describes the γ-U-Zr solid solution thermodynamics. In this section, the γ-U-Zr enthalpy and Gibbs energy of mixing are presented followed by a description of the calculation of the heat capacity, volumetric heat capacity, isothermal compressibility, and the Grüneisen parameter. Subsequently in Chapter 10: "Discussion of U-Zr Thermodynamics", the U-Zr system thermodynamics of our results and previous results are compared and the discrepancies explained. Then in Chapter 11: "Ordered/Disordered U-Zr", the created interatomic MEAM potential is used in molecular dynamics and Monte Carlo simulations, independently as well as in conjunction, to analyze the

ordering behaviors of the U-Zr system. Ordering analysis is conducted by using a short range ordering parameter, radial distribution functions, and bond order distribution functions, as well as some visual analysis. After which, the ordering, separation, and precipitate morphology in U-Zr alloys are studied in Chapter 12: “Ordering, Separation, and Precipitate Morphology”. Wherever possible we compare our results with experimental or simulation results. Lastly, a MEAM sensitivity analysis is presented in Chapter 13: “MEAM Sensitivity Analysis of Thermal Properties”.

CHAPTER 2

COMPUTATIONAL METHODS & ANALYSIS TECHNIQUES

Molecular Statics (MS) and Molecular Dynamics (MD) Calculations

Molecular statics (MS) simulations (energy minimization) and molecular dynamics (MD) simulations were performed using the "in-house" code DYNAMO (predecessor to LAMMPS or PARADYN). The process of an energy minimization simulation corresponds to relaxing (or moving) the atomic positions until zero net force is acting on the system at 0 K (minimum energy configuration). Molecular statics with DYNAMO uses the equations of motion from Newton's second law to relax the atoms. Molecular dynamics simulation consists of a numerical systematic solution to the classical equations of motion. Similarly to molecular statics, molecular dynamics calculates the force on each atom from the gradient vector of the potential energy at each atom's location. Molecular dynamics computes the phase-space trajectory, in which the atoms are allowed to interact for a period of time with forces being exerted on each atom, giving snapshots of the motion of the atoms. The forces on each atom are calculated using the MEAM interatomic potential. Temperature in a molecular dynamics simulation corresponds to an average atom velocity.

The MD simulations performed in this research, unless otherwise specified, were conducted with a supercell consisting of 10x10x10 unit cells (2000 atoms) run under an isothermal–isobaric (NPT) ensemble, in which the atoms, pressure, and temperature are held constant, with periodic boundary conditions. A Nose-Hoover thermostat [104, 105] was applied in the MD simulation to keep the system at a constant temperature.

The MD simulations must be run long enough to reach the equilibrium value, and then for additional time to ensure a good statistical average. The total MD simulation time was 100 picoseconds using a 2 femtosecond time step, with ensemble property averaging over the last 35 picoseconds.

Density Functional Theory (DFT) Calculations

Where necessary, *ab initio* calculations were performed in order to calculate defect formation energies of the Zr crystal phases. The first principles Zr study was conducted using the projector augmented wave (PAW) method [106] within the density functional theory (DFT) [107, 108] in the Vienna *ab initio* Simulation Package (VASP) [106, 109, 110]. The Perdew–Burke–Ernzerhof (PBE) [111] generalized gradient approximation (GGA) is used to describe the exchange–correlation. In addition, a Zr PAW pseudopotential with the $4d_2 5s_2$ valence electronic configuration and a core represented by [Kr] is utilized. The Zr hexagonal-close-packed (hcp) and the bcc structures were analyzed with a gamma-centered k-point mesh of 20x20x20 and all symmetry restrictions removed, resulting in 4004 k-points in the irreducible Brillouin zone. Accurate precision was used with a cutoff energy of 500 eV to minimize wrap around errors in the grid.

Monte Carlo (MC) Calculations

The Monte Carlo (MC) simulation used is based on the Metropolis Monte Carlo algorithm [112, 113]. The MC method allows for the study of order-disorder and segregation phenomena in the equilibrated system. The MC method is not based on the equations of motion, like the MD simulation, but the energetics of the states. This type of MC simulation is good for evaluating effects that would take a long time to witness during a molecular dynamics

simulation. In addition, this type of MC simulation provides insight into the possible range of thermodynamic properties which could change due to atomistic ordering effects.

Order-disorder transitions proceed through substitution between atoms followed by small atomic displacements. These order-disorder transitions are commonly found in metals and alloys. The MC approach is used to drive the atoms toward their equilibrium state at a finite temperature.

The MC simulation started with the ending positions of each atom after the previous MD simulation. Then a series of configuration transformations were performed to achieve a thermo-dynamically equilibrated state. The MC code uses a canonical (or NVT) ensemble, which means that the number of atoms, volume, and temperature is conserved.

In each MC step, one of the following two configuration changes is attempted with an equal probability:

1. A randomly selected atom is displaced from its original position in a random direction with a distance between 0 and r_{max}. This step accounts for the positional relaxation process (adjustment of bond lengths and angles). r_{max} was chosen to be 0.35 Å.
2. Two randomly selected atoms with different elemental types are exchanged. This step accounts for the compositional relaxation process.

In order to determine if the configurational change to the system is accepted, the energy between the new and old configurations is evaluated. If the new configuration has a lower energy, the configurational change is always accepted. However, if the new configuration has a

higher energy than the old configuration, the configurational change is accepted with a probability P_{XY}.

$$P_{XY} = \exp\left(\frac{-\Delta E}{k_B T}\right) \quad (1)$$

Where k_B is the Boltzmann's constant, ΔE is the change in energy between the new and old configurational states, and T is the temperature. Initially, during the approach to the low energy equilibrated states, the potential energy and the configurational acceptance rate will rapidly decrease following an exponential decay progression. Once the MC simulation has reached the condition of oscillating around the low energy equilibrated states, the probability of configurational transformation acceptance remains stable proportionately to the Boltzmann's distribution of the equilibrium ensemble. The 0 K MC simulations are performed with no Boltzmann's distribution of accepting positive energy changes; therefore, only changes that result in a decrease in the energy of the system are accepted.

The MC runs were also conducted on a bcc 10x10x10 periodic supercell for a total of 2000 atoms, unless otherwise specified. The simulation size chosen allowed the precipitation morphology to develop in a recognizable shape, while keeping computational time reasonable. In order to test the simulation size effect, the MD and MC simulations were performed on bcc 7x7x7, 10x10x10, and 15x15x15 supercells of U-20at.%Zr at 1100 K. The three different sizes lead to the same energy per atom and separation morphology, the only difference being morphological dimensions.

Molecular Statics/Dynamics (MS/MD) - Monte Carlo (MC) Iterative Method

The MC simulations with an NVT ensemble rearranges the atoms to have a lower free energy. This restructuring of the atoms creates a problem since rearranging the atoms should cause a volume change. Running a MS or a MD simulation with an NPT ensemble corrects the volume problem. However, the corrected volume changes how the structure rearranges during an MC simulation. Therefore, an iterative MC-MS and MC-MD simulation is proposed, which should eventually settle to the state that minimizes the free energy through a series of atom switching and thermal motion, if continued. A finite number of MC-MS and MC-MD iterations is proposed to approximate the minimal free energy structure.

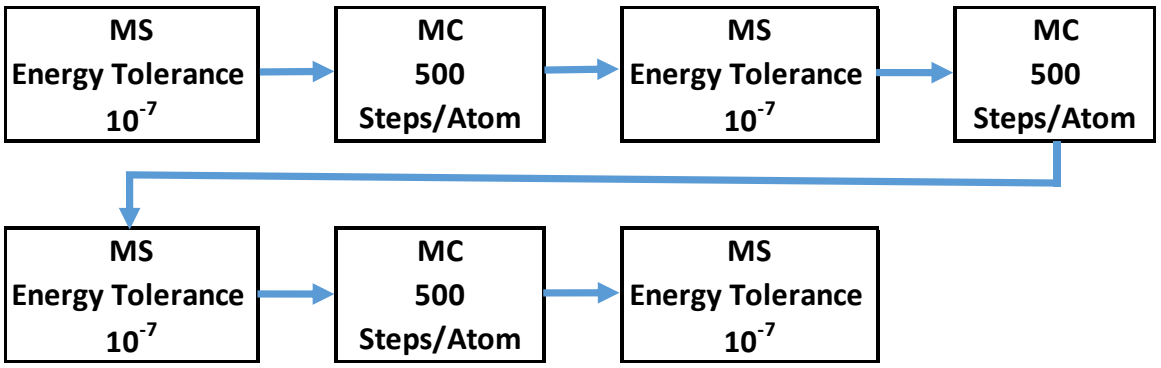

Figure 3: Flow diagram of the proposed finite iterative MS and MC simulations.

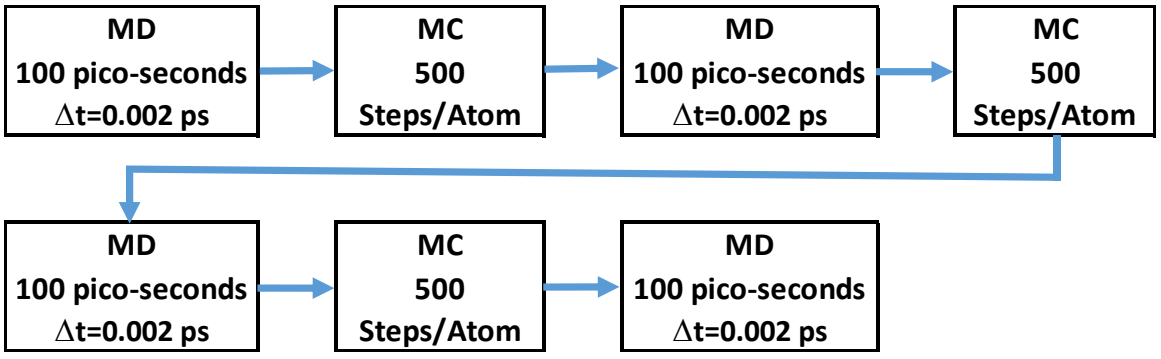

Figure 4: Flow diagram of the proposed finite iterative MD and MC simulations [56].

Radial Distribution Function (RDF) and Bond Angle Distribution Function (BADF) Analysis Techniques

The radial distribution function (RDF) is a useful tool for atomic analysis of crystal systems. The radial distribution function gives a normalized equation of the distance between atoms in the lattice. The RDF is calculated by determining the average number density of an atom to another within a spherical shell as a function of radial distance. The RDF can be described by the function g(r), which gives the probability of finding a particle in the distance r from another particle.

$$g(r) = \frac{1}{4\pi N r^2 \rho_0} \sum_{j=1}^{N} \sum_{\substack{i=1 \\ i \neq j}}^{N} \delta(r - r_{ij}) \quad (2)$$

The calculation of g(r) can give useful information about the average thermal scatter (by looking at the width of the peaks) and the phase of the system (by looking at the distance between the peaks and the relative magnitudes), and it can even give information on the chemical ordering in a complex system when elemental partial radial distance functions are used.

The bond angle distribution function (BADF) is another useful tool for atomic analysis of crystal systems. The BADF gives a normalized equation of the bond angles between atoms located within a certain distance, and can be described by the function $g_3(\theta)$, which gives the probability of finding a bond angle θ between the local atoms.

The unnormalized bond angle distribution function can be found using the Kirkwood superposition of pair distribution functions [114]. We define the unnormalized Kirkwood-approximation $G_3^{\alpha\beta\gamma}(\theta, r_1, r_2)$ between αβγ in three dimensions as

$$G_3^{\alpha\beta\gamma}(\theta, r_1, r_2) = sin\theta \int_0^{r_1} \int_0^{r_2} dr\ dr' r\ r' g^{\alpha\beta}(r)\ g^{\alpha\gamma}(r')\ \times$$

$$g^{\beta\gamma}\left(\sqrt{r^2 + r'^2 - 2rr'cos\theta}\right)\ , \qquad (3)$$

where g(r) is the pair distribution functions, θ is the bond angle between αβγ, r_1 is the maximum bond distance between αγ, and r_2 is the maximum bond distance between αβ.

After which normalization can be applied to the triplet correlation function to obtain the Kirkwood approximation of the BADF.

$$g_3^{\alpha\beta\gamma}(\theta, r_1, r_2) = \frac{G_3^{\alpha\beta\gamma}(\theta, r_1, r_2)}{\int_0^{\pi} d\theta\ G_3^{\alpha\beta\gamma}(\theta, r_1, r_2)} \qquad (4)$$

CHAPTER 3

INTERATOMIC POTENTIAL THEORY AND FORMALISM

The electron density functional theory's concept of electron density's replacement of wave functionals led to the creation of the EAM potential and the MEAM potential. The EAM potential is based on the assumption that an atom can be embedded into a homogenous electron gas, and that the resulting change in potential energy is a functional of the embedded atom electron density that can be approximated with an embedding function.

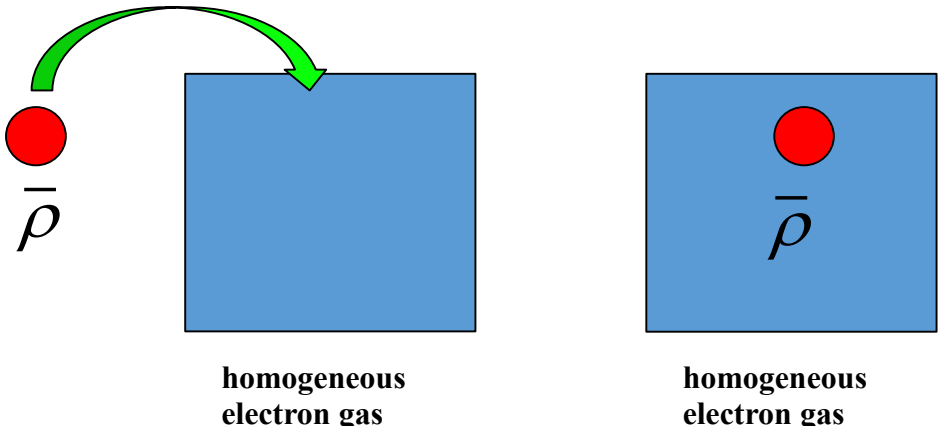

Figure 5: Physical representation of the basics of the embedding function [115].

However, the electron density in a crystal is not homogenous. Therefore, the EAM potential changes the background electron density to the electron densities for each atom and supplements the embedding energy by a repulsive pair potential to represent atoms' core-core interactions.

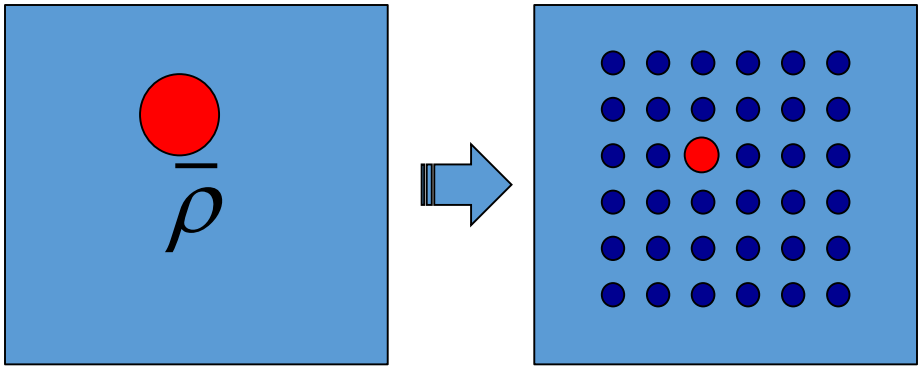

Figure 6: Physical representation of the embedding function into a lattice [115].

The EAM potential uses a simple linear superposition of the atoms' electron densities as the background electron density.

$$\bar{\rho}_i = \sum_j \rho_j^a(R_{ij}) \quad (5)$$

$$R_{ij} = |r_i - r_j| \quad (6)$$

In the equations above, R_{ij} is the distance between atoms i and j, ρ_j^a is the atomic electron density, and r_i is the position of atom i.

The EAM potential is a semi-empirical potential developed by Daw and Baskes in 1983 [77, 116] and has been used to successfully model a variety of face centered cubic (fcc) metals. The EAM inter-atomic potential does not simply depend on atom locations, but includes many body effects that depend on the local environment.

The potential energy of a crystal system, using the EAM potential, can be calculated using the embedding function F, the electron densities ρ_i, and the pair interaction potential ϕ.

$$U = \sum_i F(\bar{\rho}_i) + \frac{1}{2}\sum_{i,j} \phi(R_{ij}) \quad (7)$$

Modified Embedded Atom Method (MEAM) Interatomic Potential

However, the EAM potential has problems simulating materials with significant directional bonding, and cannot be used when simulating these materials. Criteria for significant directional bonding in materials were created using the Cauchy relation or Cauchy discrepancy which relates the C_{12} and the C_{44} elastic moduli for symmetrically cubic materials. The Cauchy relation stated that the transverse expansion elastic constant (C_{12}) is equal to the shear modulus elastic constant (C_{44}), or $C_{12}=C_{44}$ [117], if the crystal and the atoms have cubic symmetry. This condition is not satisfied for most metals. Therefore, materials with $C_{12}/C_{44} - 1 < 0$ (Cauchy discrepancy) are said to have a significant amount of directional bonding and cannot be described by EAM [117].

The MEAM potential builds on the EAM potential by allowing the background electron density to depend on the local environment, whereas the EAM potential uses a linear superposition of spherically averaged electron densities.

The MEAM inter-atomic potential is a semi-empirical potential proposed by Baskes et al. [84] that has been successfully used to reproduce the physical properties of various metals with different crystal structures. The MEAM potential is useful because it has the ability to replicate physical properties while keeping the computational power and time, which are necessary to complete the simulations, down to an acceptable level.

The MEAM potential for a single element contains 13 adjustable parameters (A, B^0, B^1, B^2, B^3, t^1, t^2, t^3, α, δ, Ec, C_{min}, and C_{max}) used to obtain the physical properties seen by experiments or *ab initio* simulations. However, the MEAM potential becomes more complex for binary and tertiary alloys. A binary alloy has 13 adjustable parameters for each element and at

least 14 adjustable parameters (δ, α, r_e, ρ_U, ρ_{Zr}, Δ, $C_{min}^{(1,1,2)}$, $C_{min}^{(1,2,1)}$, $C_{min}^{(1,2,2)}$, $C_{min}^{(2,1,2)}$, $C_{max}^{(1,1,2)}$, $C_{max}^{(1,2,1)}$, $C_{max}^{(1,2,2)}$, $C_{max}^{(2,1,2)}$) for the binary alloy interactions.

A MEAM potential is presented for the high temperature bcc γ-U phase. MEAM potentials add an angular component to the older EAM potential to account for directional bonding.

With the MEAM potential, the total energy E of a system of atoms is given by

$$U = \sum_i F_i(\overline{\rho}_i) + \frac{1}{2}\sum_{i,j\neq i} \phi_{ij}(R_{ij}) S(R_{ij}) \ , \qquad (8)$$

where F_i is the embedding function, ρ_i is the background electron density at site i, S_{ij} is the radial screening function, and $\varphi_{ij}(R_{ij})$ is the pair interaction function between atoms i and j at a distance, R_{ij}.

Embedding Function

The embedding function describes the energy it takes to add (or embed) the atom to the crystal structure. The embedding function for the MEAM potential is defined by

$$F_i(\bar{\rho}_i) = A_i E_{ci} \left(\frac{\bar{\rho}_i}{\overline{\rho_i^e}}\right) ln\left(\frac{\bar{\rho}_i}{\overline{\rho_i^e}}\right), \qquad (9)$$

where A_i is an adjustable parameter, Ec_i is the cohesive energy, and $\rho^e{}_i$ is the electron density evaluated at equilibrium in the reference structure.

Universal Binding Energy Relationship (UBER)

The reference state energies are found from the universal binding energy relationship (UBER), which uses a reference structure to create the pair potential. The UBER describes

cohesion and adhesion of unrelaxed surfaces, chemisorption, and diatomic molecules [118]. The UBER in the MEAM is normally fit through a few parameters.

The pair potential, instead of being given explicitly, is given as a functional of an embedding atom function and a universal function ($\mathrm{E^u(R)}$) that is able to reproduce the universal equation of state (EOS) [119] for the potential energy of a reference crystal structure. The universal function ($\mathrm{E^u(R)}$) describes the uniform expansion or contraction in the reference structure.

The value of the energy per atom for the equilibrium reference structure is obtained from the zero-temperature universal EOS by Rose et al. [119] as a function of nearest-neighbor distance R.

$$E^u(R_{ij}) = -E_c\left[1 + a^* + \delta(a^*)^3\frac{r_e}{R_{ij}}\right]e^{-a^*} \quad (10)$$

$$a^* = \alpha\left(R_{ij}/r_e - 1\right) \quad (11)$$

$$\alpha = (9B\Omega/E_c)^{1/2} \quad (12)$$

The repulse and attract parameters of the MEAM potential are the short range attraction and repulsion forces in the universal EOS (the cubic repulsion/attraction term in the Rose rnergy). In this work a single value of δ is used in the repulsive and attractive parts of the universal EOS.

Reference State & Pair Potential

The universal EOS combined with a reference structure can be back-calculated to a pair potential. This is done by equating the reference structure to the pair potential as shown in Equation (13).

$$E^u(R_{ij}) = F\left[\overline{\rho^0}(R_{ij})\right] + \frac{1}{2}\sum_{i,j}\phi(R_{ij}) = -E_c\left[1 + a^* + \delta(a^*)^3\frac{r_e}{R_{ij}}\right]e^{-a^*} \quad (13)$$

The equation can be re-written in the first nearest neighbor MEAM form of

$$E^u(R_{ij}) = F\left[\overline{\rho^0}(R_{ij})\right] + \left(\frac{Z_1}{2}\right)\phi(R_{ij}), \quad (14)$$

where Z_1 is the number of 1NN atoms. The equation can be rearranged to obtain the pair potential as follows

$$\phi(R_{ij}) = \left(\frac{2}{Z_1}\right)\left\{E^u(R_{ij}) - F\left[\overline{\rho^0}(R_{ij})\right]\right\}, \quad (15)$$

where $\bar{\rho}^0$ is the background electron density for the reference structure.

Background Electron Density

The background density depends on the local environment, in particular the atoms' angular relation to one another. These angular contributions are split into partial electron densities. The background electron density ($\bar{\rho}$) is composed of a spherically symmetrical partial electron density $\bar{\rho}_i^{(0)}$ and angular partial electron densities $\bar{\rho}_i^{(1)}$, $\bar{\rho}_i^{(2)}$, and $\bar{\rho}_i^{(3)}$, and has the following form.

$$\left(\rho_i^{(0)}\right)^2 = \left[\sum_{j\neq i}\rho_j^{a(0)}(R_{ij})\right]^2 \quad (16)$$

$$\left(\rho_i^{(1)}\right)^2 = \sum_{\alpha}\left[\sum_{j\neq i}\frac{R_{ij}^{\alpha}}{R_{ij}}\rho_j^{a(1)}(R_{ij})\right]^2 \quad (17)$$

$$\left(\rho_i^{(2)}\right)^2 = \sum_{\alpha,\beta}\left[\sum_{j\neq i}\frac{R_{ij}^{\alpha}R_{ij}^{\beta}}{R_{ij}^2}\rho_j^{a(2)}(R_{ij})\right]^2 - \frac{1}{3}\left[\sum_{j\neq i}\rho_j^{a(2)}(R_{ij})\right]^2 \quad (18)$$

$$\left(\rho_i^{(3)}\right)^2 = \sum_{\alpha,\beta,\gamma}\left[\sum_{j\neq i}\frac{R_{ij}^{\alpha}R_{ij}^{\beta}R_{ij}^{\gamma}}{R_{ij}^3}\rho_j^{a(3)}(R_{ij})\right]^2 - \frac{3}{5}\sum_{\alpha}\left[\sum_{j\neq i}\frac{R_{ij}^{\alpha}}{R_{ij}}\rho_j^{a(3)}(R_{ij})\right]^2 \quad (19)$$

In these equations, $\rho_j^{a(h)}$ represents the atomic electron densities of atom j at the distance R_{ij} relative to the site i.

The atomic electron densities are given by

$$\rho_j^{a(h)}(R_{ij}) = \rho_0 \, S_{ij} \, f_{cut}(R_{ij}) \, exp\left[-\beta^{(h)}\left(\frac{R_{ij}}{r_e} - 1\right)\right], \qquad (20)$$

where $\beta^{(h)}$ is the partial electron density decay, r_e is the nearest neighbor distance, S_{ij} is the screening factor, f_{cut} is the cut-off function, and ρ_0 is a scaling factor which plays no role for pure elements, but has a significant role for alloy systems.

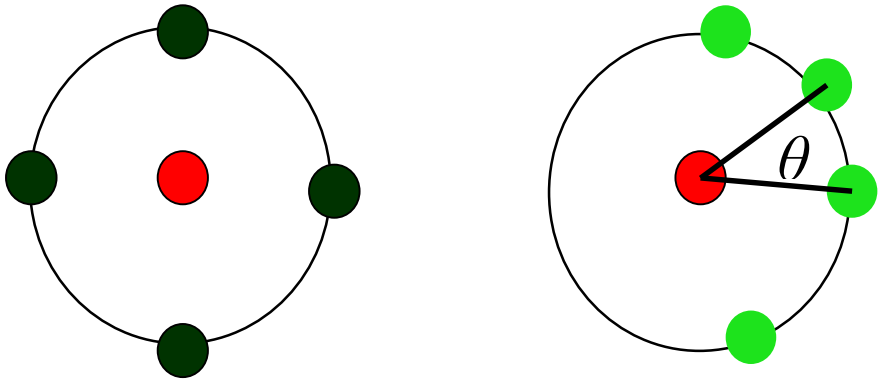

Figure 7: Physical interpretation of directional bonding by partial electron densities [120].

The geometric manner in which $\rho_i^{(l)}$ is defined allows us to consider the partial background electron densities in a similar manner to the specific angular momentum contributions to the background electron densities known as electron orbitals (spdf). The partial background electron densities are orthogonal and can also be written in terms of Legendre polynomials, i.e.,

$$\left(\rho_i^{(l)}\right)^2 = \sum_{j\neq i}\sum_{k\neq i} \rho_j^{a(l)}(R_{ij})\rho_k^{a(l)}(R_{ik})P_l^0\left(cos\left(\theta_{ikj}\right)\right) \qquad (21)$$

where P_l^0 are the Legendre polynomials.

$$P_0^0(z) = 1 \quad (22)$$

$$P_1^0(z) = z \quad (23)$$

$$P_2^0(z) = z^2 - \frac{1}{3} \quad (24)$$

$$P_3^0(z) = z^3 - \frac{3}{5}z \quad (25)$$

The total background electron density can be obtained from the weighted partial background electron densities through an intermediate term Γ, i.e.,

$$\bar{\rho}_i = \rho_i^{(0)}\sqrt{1+\Gamma} \quad (26)$$

$$\Gamma = \sum_{l=0}^{3} t_i^{(l)} \left(\frac{\rho_i^{(l)}}{\rho_i^{(0)}}\right)^2 \quad (27)$$

where $t_i^{(l)}$ is the weighting factor for each of the partial electron densities. For convenience $t_i^{(0)} = 1$. Setting one value helps to visualize changes in the weighted parameters since the electron density is weighted by the t parameters.

Screening Function

Screening between two atoms (i and j) is defined as the product of screening factors, S_{ijk}, due to the neighboring atoms (k) that contribute to screening, leading to

$$S_{ij} = \prod_{k \neq i,j} S_{ijk} \; . \quad (28)$$

Consider a two-dimensional model of screening, leading to an ellipse method of describing screening. If the atoms i and j lie on the x-axis and the atom k is somewhere in the

x,y plane that does not lie on top of either atom, an ellipse model can be used to describe the regions of screening.

Atom screening can be visualized using the ellipse model seen in Figure 8. In this model, atoms i and j are being screened by atom k. The amount of screening is separated into three regions: completely screened, partially screened, and non-screened.

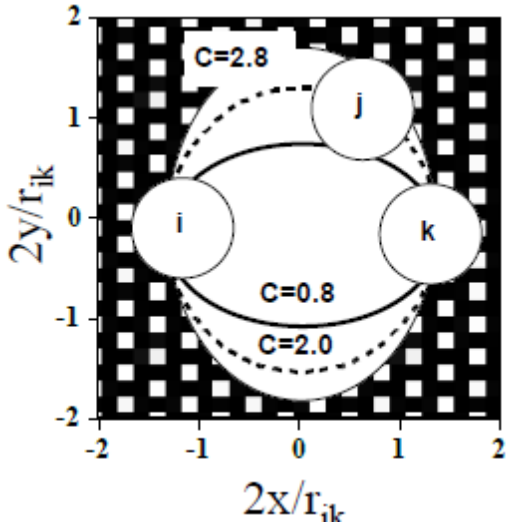

Figure 8: Visual representation of MEAM screening with an ellipse [120].

From this two-dimensional interpretation of screening, an equation can be made to represent the ellipse.

$$x^2 + \left(\frac{1}{C}\right) y^2 = \left(\tfrac{1}{2} R_{ij}\right)^2 \quad (29)$$

The ellipse parameter C is determined by a function of ratios between atoms i,j, and k given by

$$C = \frac{2(X_{ik}+X_{kj}) - (X_{ik}-X_{kj})^2 - 1}{1-(X_{ik}-X_{kj})^2}, \quad (30)$$

where $X_{ik} = \left(R_{ik}/R_{ij}\right)^2$ and $X_{kj} = \left(R_{kj}/R_{ij}\right)^2$. The screening factor S_{ikj} is defined as

$$S_{ikj} = f_c[(C - C_{min})/(C_{max} - C_{min})] \quad (31)$$

where C_{min} and C_{max} determine the extent of the screening and fc is the cut-off function.

Cut-Off Function

The cut-off function describes the smooth, gradually decreasing distance effect on the interactions between the atoms. The smooth cut-off screening function (fc) is defined by

$$f_c(x) = 1, \quad x \geq 1$$

$$[1-(1-x)^6]^2, \quad 0 < x < 1,$$

$$0, \quad x \leq 0 \qquad (32)$$

$$x = \left(\frac{R_{ij}^{cut-off} - R_{ij}}{\Delta R_{ij}}\right) \qquad (33)$$

where ΔR_{ij} is the width of the cut-off region and $R^{cut\text{-}off}$ is the maximum cut-off distance. Normally, the MEAM cut-off function employs $(1\text{-}x)^4$ rather than the $(1\text{-}x)^6$; however, the power was changed to the sixth when fitting the stacking fault energy for Zr.

2nd Nearest Neighbor (2NN) MEAM

The main difference between the 1NN MEAM and the 2NN MEAM is that the 2NN MEAM attempts to incorporate 2NN atomic interactions, which are weaker than 1NN interactions, into the pair interaction term ϕ. The 1NN MEAM is able to neglect the 2NN interactions through the use of a strong many-body screening function. However, the 2NN MEAM is able to include 2NN interactions by adjusting the many-body screening function so that it becomes less severe.

Screening can play a large role on many parameters as temperature changes. Thermal vibration can cause atoms to drift in and out of various screening regions. When implementing

the 1NN MEAM, the screening parameters are selected to ensure that the first nearest neighbors are entirely un-screened. This "strong" screening allowed for the neglect of 2NN interactions, with only 1NN interactions being considered. The strong screening was taken into account by the many body screening function from a large minimum initial screening distance (C_{min}).

However, for 2nd NN MEAM potentials the start initial minimum distance that screening starts (C_{min}) is reduced, leading to a screening function that is less "strong" and incorporates second nearest-neighbor interactions. The UBER relationship for 2NN MEAM is slightly different due to the fact that the second nearest neighbor energy contributions have to be added.

$$E^u(R_{ij}) = F\left[\overline{\rho^0}(R_{ij})\right] + \frac{1}{2}\sum_{i,j}\phi(R_{ij}) \quad (34)$$

$$E^u(R_{ij}) = F\left[\overline{\rho^0}(R_{ij})\right] + \left(\frac{Z_1}{2}\right)\phi(R_{ij}) + \left(\frac{Z_2 S}{2}\right)\phi(aR_{ij}) \quad (35)$$

$$E^u(R_{ij}) = -E_c\left[1 + a^* + \delta(a^*)^3\frac{r_e}{R_{ij}}\right]e^{-a^*} \quad (36)$$

$$a^* = \alpha\left(R_{ij}/r_e - 1\right) \quad (37)$$

$$\alpha = (9B\Omega/E_c)^{1/2} \quad (38)$$

Here, Z_2 is the number of 2NN atoms, "a" is the ratio between the second and first nearest-neighbor distances, and S is the screening function on the second nearest-neighbor interactions. It should be noted that the screening function S is a constant for a given reference structure, if a value is given to C_{max} and C_{min}.

By introducing another pair potential, ψ(R), the equation above can be rewritten as shown in Equation (39) and Equation (40).

$$E^u(R_{ij}) = F\left[\overline{\rho^0}(R_{ij})\right] + \left(\frac{Z_1}{2}\right)\psi(R_{ij}) \quad (39)$$

$$\psi(R_{ij}) = \phi(R_{ij}) + \left(\frac{Z_2 S}{Z_1}\right)\phi(aR_{ij}) \quad (40)$$

The function, ψ(R) can be calculated from the equation as a function of R. Then, the pair potential ϕ(R) is calculated using Equation (41).

$$\phi(R_{ij}) = \psi(R_{ij}) + \sum_{n=1}(-1)^n \left(\frac{Z_2 S}{Z_1}\right)^n \psi(a^n R_{ij}) \quad (41)$$

The summation in Equation (41) is performed until the correct value of energy is obtained for the equilibrium reference structure [121].

2nd Nearest Neighbor (2NN) MEAM Alloy

To describe an alloy system, the pair interaction between different elements should be determined. In the 2NN MEAM, a perfectly ordered binary intermetallic compound, where one type of atom has a different atom type as its first nearest-neighbors, is considered to be a good reference structure for creating the alloy pair potential. The B1 (NaCl type) reference structure is used for the U-Zr MEAM potential. For the B1 reference structure, the total energy per atoms (for half i atoms and half j atoms), $E_{ij}^{u}(R)$, is given by

$$E_{ij}^{u}(R) = \frac{1}{2}\left\{F_i(\bar{\rho}_i) + F_j(\bar{\rho}_j) + Z^{ij}\phi_{ij}(R) + \frac{1}{2}Z_2^{ij}\left(\phi_{ii}(aR) + \phi_{jj}(aR)\right)\right\}, \quad (42)$$

where Z^{ij} is the number of 2NN atoms in the reference structure. ϕ_{ii} and ϕ_{jj} are pair interactions between i atoms and between j atoms, respectively, and "a" is the ratio between the second and first nearest-neighbor distances. The procedure of computing ρ_i and ρ_j is not different from that in 1NN MEAM except that the contribution from the second nearest-neighbors should also be considered. The pair interactions between the same types of atoms can be computed from the descriptions of individual elements [121], i.e.,

$$\phi_{ij}(R) = \frac{1}{Z_{ij}}\left\{2E_{ij}^{u}(R) - F_i(\bar{\rho}_i) - F_j(\bar{\rho}_j) - \frac{1}{2}Z_2^{ij}\left(\phi_{ii}(aR) + \phi_{jj}(aR)\right)\right\} \quad (43)$$

The cohesive energy for the alloy is determined by the elemental cohesive energies and a formation parameter Δ_{ij} , i.e.,

$$E_{ij}^{0} = \frac{\left(E_i^0 + E_j^0\right)}{2} - \Delta_{ij} \quad (44)$$

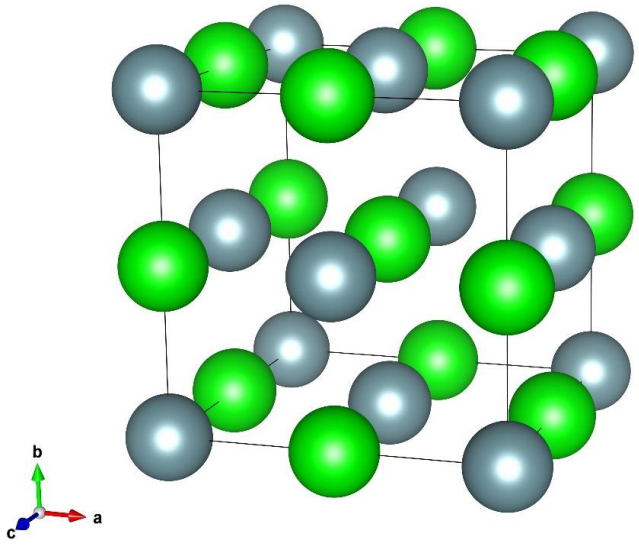

Figure 9: Unit cell of the B1 U(green)-Zr(grey) reference crystal structure.

Table 2: Structure details of the B1 U-Zr reference crystal structure.

Pearson Symbol	cF8
Space Group	Fm3m
Prototype	Na-Cl
Strukturbericht Designation	B1

CHAPTER 4

URANIUM, ZIRCONIUM, AND THE URANIUM-ZIRCONIUM ALLOY MEAM PARAMETERS

The semi-empirical MEAM potential was constructed to match known *ab initio* and experimental values of the elemental elastic constants and defect formation energies.

The old MEAM [56] potential was modified to match the experimental high temperature γ-U-Zr properties, while maintaining the elemental base properties at 0 K and at temperature.

Table 3: Elemental parameters for MEAM potential.

Elemental Parameters for MEAM Potential								
Elem.	lat	E_C	α	A	$\beta^{(0)}$	$\beta^{(1)}$	$\beta^{(2)}$	$\beta^{(3)}$
U	fcc	5.27	5.1	0.98	4.8	6	6	6
	$t^{(1)}$	$t^{(2)}$	$t^{(3)}$	a_{lat}	δ	ρ^0	C_{min}	C_{max}
	2.5	4	1.0	4.28	.105	1.2	1.0	1.9
Elem.	lat	E_C	α	A	$\beta^{(0)}$	$\beta^{(1)}$	$\beta^{(2)}$	$\beta^{(3)}$
Zr	bcc	6.2	4.1	0.48	2.8	2	7	1
	$t^{(1)}$	$t^{(2)}$	$t^{(3)}$	a_{lat}	δ	ρ^0	C_{min}	C_{max}
	3	2	-7	3.535	-.03	0.8	0.7	0.99

Table 4: B1 U-Zr alloy and screening parameters.

B1 U-Zr Alloy and Screening Parameters			
r_e	Δ	α	δ
2.85	0.8	4.8	0.05
C_{min}(U,Zr,U)	C_{min}(Zr,U,U)	C_{min}(Zr,Zr,U)	C_{min}(Zr,U,Zr)
0.8	0.5	0.5	0.5
C_{max}(U,Zr,U)	C_{max}(Zr,U,U)	C_{max}(Zr,Zr,U)	C_{max}(Zr,U,Zr)
2.5	2	2.8	2.8

In the table above, the middle atom listed in the screening notion is the screening atom, while the first and last atoms are the atoms being screened.

It should be noted that, in addition to the MEAM parameters, the cut-off function formation may need to be changed to match the form seen in Chapter 3: “Interatomic Potential”.

Fitting the MEAM Potential Parameters

While either the force matching method [63, 122-124] or particle swarm optimization (PSO) [61, 62, 85, 125] has been commonly used to fit EAM and MEAM potentials, both can have difficulties when used with high temperature transition metals. Therefore, the potentials were iterated by using knowledge of the system.

To construct a high temperature MEAM potential, it is still necessary to begin with the 0 K density functional theory (DFT) or experimental results in order to ensure that the basis of the potential matches the known elastic constants and defect formation energies. The procedure for fitting a 1NN MEAM potential is described by Baskes et al. [84, 126]. After a 1NN MEAM has been made, the transition to a 2NN MEAM involves iterating the screening parameter C_{min}, A, and the partial electron density parameters t^1, t^2, t^3, β^0, β^1, β^2 and β^3.

It is useful to fit properties based on symmetry of the defects, elastic constants, or interface, as well as the symmetry of the phase. In addition, as noted previously, different crystal structure properties are dependent on different parameters, making the fitting of multiple phases useful as well. The electron orbital in spherical harmonics can help visualize some of the symmetries of the orthogonal Legendre polynomials. This knowledge combined with the sensitivity tables in Chapter 13 “MEAM SENSITIVITY AND UNCERTAINTY ANALYSIS FOR THE U-ZR SYSTEM” enables the fitting of new elemental and alloy systems employing knowledge of the sensitivity of the desired property to the variation of each parameter.

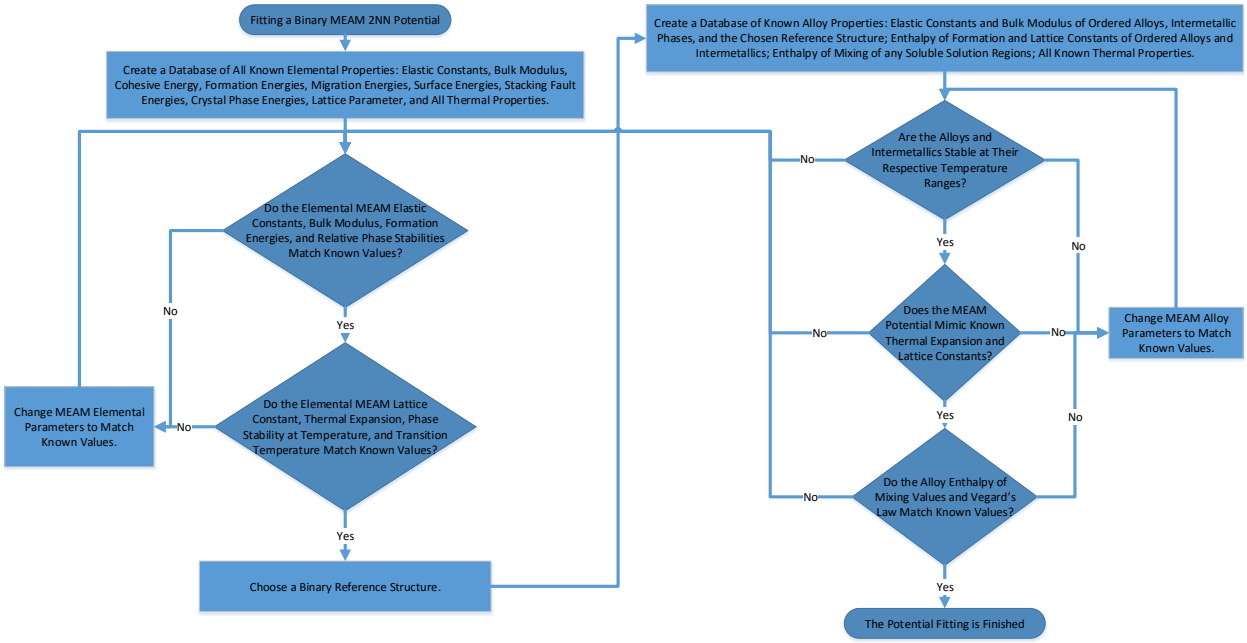

Figure 10: MEAM potential fitting flow diagram, showing the process of fitting a MEAM binary alloy system.

The first step in determining which parameters to change is to determine the cause of the enthalpy of mixing curve problem (seen in Figure 31b). The MEAM enthalpy of mixing curves are not known for varying drastically with temperature. Therefore, since all of the preliminary MEAM potentials [56] were constructed to match the low temperature decomposition curve for γ-U,β-Zr which shows a positive trend, the high temperature enthalpy of mixing curve showed a similar positive trend. With some trial and error, it was determined that the t^3 parameter (f-electron orbital symmetry) was a large contributor to the misshapen uranium-rich concentration section of the enthalpy of mixing curve, and the alloy α parameter allowed for the downward shift of the enthalpy of mixing curve. It was initially thought that some of the alloy screening parameters could change the shape of the enthalpy of mixing curves to fit the experimental results, but the elemental partial electron density parameters turned out to be the largest contributor to the enthalpy of mixing curve's shape. The determination of which parameters

needed to be changed and their effect on the system properties can be found in Chapter13: "MEAM Sensitivity and Uncertainty Analysis".

CHAPTER 5

STRUCTURAL PROPERTIES OF THE ELEMENTAL PHASES OF URANIUM AND ZIRCONIUM

Lattice parameters, elastic constants, and defect formation energies of elemental bcc U, face-centered-cubic (fcc) U, bcc Zr, and hcp Zr are calculated using the MEAM potential (Chapter 4: "MEAM Parameters") developed in this work. For the Zr metal, DFT calculations of defect formation energies are also conducted in order to develop a comprehensive understanding.

The defect formation energies in an atomistic crystal system are calculated from

$$E_{vac}^{f} = E_{bulk}\left(N-1\right) - \frac{N-1}{N} E_{bulk}\left(N\right) , \qquad (45)$$

$$E_{\text{int}}^{f} = E_{bulk}\left(N+1\right) - \frac{N+1}{N} E_{bulk}\left(N\right), \qquad (46)$$

where E(N) is the energy of the system in question and N is the number of atoms in that system.

Uranium Elastic Constants and Defect Formation Energies

The MEAM lattice constants, elastic constants, and formation energies for bcc U, which are shown in Table 5, are in good agreement with previous DFT and experimental values. In addition, the lattice constants and elastic constants for fcc U in Table 6 also show agreement with most of the previous values. However, for fcc U the lattice constant and elastic constant C_{11} are a little low and C_{44} a little high compared to most of the previous values.

The molecular statics was used to obtain the ground state material properties with an energy convergence criterion of 10^{-6}. Elastic constants were calculated at 0 K via analysis of the changes in internal energy due to small strains enforced on the simulation cell. The internal

energy of a crystal system under strain was expanded in a Taylor series in powers of the strain tensor with respect to the initial energy of the unstrained crystal. Then, each elastic constant was computed from the application of a unique strain on the crystal and the resulting change in internal energy [58]. This methodology is outlined by Söderlind [127].

The fitting of the base uranium parameters was constructed based on *ab initio* uranium bcc and fcc simulations. The resultant potential while stable for the orthorhombic (A20) α-U phase, is unable to mimic the lattice constants quantitatively. Therefore a phase which is not the ground state phase is used for the base of the MEAM potential. The fcc crystal structure was chosen as the reference structure of uranium because it was relatively simple compared to using a bcc reference structure, where screening parameters are a larger concern.

Experimental bulk modulus values for uranium were obtained by Yoo et al. [128] using in situ diamond-anvil cell x-ray/laser heating experiments. In these experiments, it was observed that the γ-U phase was stable at high pressures. The bulk modulus values were obtained using a temperature-independent Birch-Murnaghan EOS fit to volume compression data. The resulting Murnaghan EOS fit to the data with B=135.5 GPa and B'=3.79 for α-U and B=113.3 GPa and B'=3.37 for γ-U. In addition, using Debye-Gruneisen quasiharmonic theory, free energy calculations show that the softer bulk modulus of the γ-phase, compared to the α phase, stabilizes the γ-phase at high temperatures [51, 128, 129].

Matter et al. [130], using a positron annihilation coincidence count rate at the peak of the angular correlation curve (CCR) in uranium, was able to estimate the mono-vacancy formation energy of γ-U. The trapping model was then applied to the collected data in the γ-phase, resulting in a 1.20 ± 0.25 eV mono-vacancy formation energy. However, due to errors

introduced by impurities and the thermal positron CCR techniques, Matter et al. reported the mono-vacancy formation energy is most likely between 1-1.3 eV.

Table 5: bcc Uranium Properties: Comparison of lattice constant, elastic constants and point defect energies.

Date	Reference	Comments	a [Å]	C_{11}[GPa]	C_{12} [GPa]	C_{44} [GPa]	$C'=(C_{11}-C_{12})/2$ [GPa]	B [GPa]	Vacancy Formation [eV]	Interstitial Formation [eV]	[100] Split Interstitial [eV]
2015	Current work	MEAM	3.438	102	117	48	-8	115	1.16	1.6	0.6
2014	Söderlind et al. [57]	FPLAPW (+/-SOC) / LDA+U (+/-SOC)	3.454, 3.437 / 3.583, 3.482	-	-	-	-	150, 137 / 66, 130	-	-	-
2013	Moore et al. [56]	MEAM	-	111	117	15	-3	117	1.34	-	0.89
2013	Beeler et al. [131]	PBE-GGA	3.427	86	155	37	-34.5	132	1.38	1.54	0.5
2013	Smirnova et al. [124]	EAM	3.542	-	-	-	-	92	2.2-3.0	-	-
2012	Beeler et al. [58]	MEAM	3.503	111	117	15	-3	115	1.38 (0K) 1.8-2.3 (800-1300K)	-	0.38-0.75 (800-1300K)
2012	Smirnova et al. [63]	EAM	3.493	-	-	-	-	95	1.52	-	-
2012	Y. Li et al. [61]	COMB3, PW91-GGA	3.509, 3.43	160, 95	122, 156	46, 35	19, -30.5	135, 136	-	-	-
2012	J.H. Li et al. [132]	PW91-GGA	3.455	103	142	46	-19.5	129	-	-	-
2011	Ru-Song Li et al. [60]	GGA+SP	3.373	103.9	120.1	30.7	-8.1	114.7	-	-	-
2010	Beeler et al. [133]	PBE, PW91	3.4283, 3.4383	-	-	-	-	133.6, 133.0	1.384, 1.323	-	-
2010	Shang et al. [134]	PW91-GGA	3.438	83.5	158.6	37.9	-37.6	132.8	-	-	-
2008	Taylor [135]	PW91-GGA	3.43	161	184	56	-11.5	176	-	-	-
2008	Xiang et al. [136]	PBE-GGA	3.4	-	-	-	-	122.6	1.08	-	-
2001	Crocombette et al. [137]	PW-LDA	3.37	-	-	-	-	170	-	-	-
1998	Yoo et al. [128]	Birch-Murnaghan or Compressibility*	3.198 (59Gpa, 2300K)	-	-	-	-	113.3	-	-	-
1980	Matter et al. [130]	PAS*	-	-	-	-	-	-	1.20 ± 0.25	-	-

Note: The * means experimental result.

Table 6: fcc Uranium Properties: Comparison of lattice constant, elastic constants, and point defect energies.

Date	Reference	Comments	a [Å]	C_{11} [GPa]	C_{12} [GPa]	C_{44} [GPa]	$C'=(C_{11}-C_{12})/2$ [GPa]	B [GPa]	Vacancy Formation Energy, E_v^f [eV]
2015	Current work	MEAM	4.280	128	130	50	-6	121	1.3
2013	Moore et al. [56]	MEAM	-	91.1	128.6	23.3	-18.8	118	1.15
2013	Beeler et al. [131]	PBE-GGA	4.433	46	144	40	-49	111	-
2012	J.H. Li et al. [132]	PW91-GGA	4.443	71	144	26	-36.5	111	-
2011	Ru-Song Li et al. [60]	GGA+SP	4.323	59	34.5	10.2	12.25	135	-
2010	Shang et al. [134]	PW91-GGA	4.438	13.6	165.6	20.2	-76	114.7	-
2008	Taylor [135]	PW91-GGA	4.48	184	267	28	-41.5	239	-
2001	Crocombette et al. [137]	PW-LDA/FLAPW	4.30	-	-	-	-	154	-
2000	Jones et al. [138]	LCGTO-FF/FLAPW) (LDA +/-SO	4.305, 4.314/ 4.311, 4.315	-	-	-	-	160, 142 / 148, 228	-
2000	Jones et al. [138]	LCGTO-FF/ FLAPW) (GGA +/-SO	4.410, 4.430/ 4.417, 4.421	-	-	-	-	101, 110 / 125, 99	-

Zirconium Elastic Constants and Defect Formation Energies

The MEAM and first principles lattice constants and elastic constants for hcp and bcc Zr is presented in Table 7 and

Table 8 respectively, along with an extensive literature review of previous research. Next the vacancy formation energy for Zr is presented in Table 9. The elastic constants are obtained using the same kind of methodology used to determine the uranium elastic constants above.

The Zr MEAM potential was made to fit both the hcp α-Zr and the bcc β-Zr phases; however, special care was taken to ensure the fitting of the β-Zr thermal properties. The more

complex bcc structure was chosen to be the reference structure of Zr to allow the MEAM potential to mimic both hcp and bcc structure behaviors.

In the past, there have been a multitude of reported α-Zr lattice constants, bulk moduli, and elastic constants, obtained in a variety of ways. Most of the previously documented values show decent consistency and reliability. However, the DFT-PBE and the MEAM potential, both optimized for the β-Zr phase, show a slightly less than average α-Zr bulk modulus.
The MEAM hcp Zr lattice constant "a" and the bulk modulus values are a little low compared to compared to most of the previous values seen in Table 7, while the other lattice constant and elastic constants are in good standing with the previous values. The MEAM bcc Zr elastic constant C_{12} is a little low and C_{44} a little high compared to most of the previous values seen in Table 8, while the rest of the properties are in good standing with the previous values. The reduced C_{12} for the bcc Zr MEAM potential causes the shear constant ($C'=(C_{11}-C_{12})/2$) to be positive instead of negative, indicating an overstability of the bcc Zr configuration at 0 K. However, this compromise was made to ensure the bcc stability of the higher temperature phase. The Zr MEAM potential is also able to replicate the vacancy formation energy of the hcp and bcc phases seen in Table 9. There existed little previously known vacancy formation energy values of the bcc Zr phase.

Table 7: hcp Zirconium Properties: Comparison of lattice constants and elastic constants.

Date	Reference	Comments	a [Å]	c [Å]	B [GPa]	C_{11} [GPa]	C_{12} [GPa]	C_{13} [GPa]	C_{33} [GPa]	C_{44} [GPa]	$C_{66}=.5(C_{11}-C_{12})$ [GPa]
2015	Current Work	DFT-PBE	-	-	83	144	-	-	166	33.4	-
2015	Current Work	MEAM	3.1427	5.137	83.7	126.1	69.9	77.1	173.3	23.3	28.1

2012	Blomqvist et al. [139]	GPAW-GGA-PBE	3.237	5.157	91	157	51	62	158	15	53
2011	Wang et al. [140]	DFT-PBE-GGA with Electron-Phonon Coupling (EPC)	3.236	5.168	96, 97.4	146.7	68.5	71	163.3	26	39.1
2010	Zhu et al. [141]	PW91/UPP	3.223	5.175	96	160	-	66	182	18	-
2008	Hao et al. [142]	DFT-PBE	3.24	5.178	93.4	141.1	67.6	64.3	166.9	25.8	36.8
2008	Liu et al. [143]	Ultrasonic and Synchrotron*	-	-	95.3	-	-	-	-	-	-
2007	Vérité et al. [144]	DFT-PBE-LDA DFT-PBE-GGA	3.16, 3.24	5.132, 5.226	114, 101	141, 147	-	-	197, 166	16, 24	15, 32
2007	Mendelev and Ackland [145]	EAM (3 Potentials)	3.231, 3.220, 3.234	5.186, 5.215, 5.168	-	196, 165, 147	88, 65, 69	81, 63, 74	212, 180, 168	47, 48, 44	54, 50, 39

Table 7 continued: hcp Zirconium Properties: Comparison of lattice constants and elastic constants.

2006	Schnell et al. [146]	Tight Binding (TB-E, TB-T)	-	-	-	133, 142	80, 71	73, 71	148, 147	7, 8	26.5, 35.5
2006	Kim et al. [147]	MEAM	-	-	-	151.5	71.8	66.1	160.6	34.1	39.9
2005	Zhao et al. [148]	X-ray diffraction, Birch-Murnaghan EOS*	3.233	5.146	92, 94	-	-	-	-	-	-
2005	Greeff [149]	DFT-GGA	3.232	5.182	-	-	-	-	-	-	-
2004	Ikehata et al. [150]	DFT-PBE	3.232	5.182	93.4	139.4	71.3	66.3	162.7	25.5	34.1
2002	Domain et al. [151]	PW91/UPP-LDA, PW91/UPP-GGA	3.16, 3.23	5.10, 5.18	105, 92	145, 142	73, 64	83, 64	177, 164	22, 29	36, 39
2002	Clouet et al. [152]	FP-LMTO	-	-	-	153.1	63.4	76.5	171.2	22.4	44.9
2002	Yamanaka et al. [153]	XPS*	3.232	5.147	-	-	-	-	-	-	-
1999	Pasianot and Monti [154]	EAM	3.232	5.149	-	143.4	72.8	65.3	164.7	32.0	35.3
1995	Fast et al. [155]	DFT-LDA	-	-	-	156	65	76	182	25	45.5
1994	Baskes and Johnson [126]	MEAM	-	-	-	152	74	63.2	153.3	33.2	39
1993	Cleri and Rosato [156]	Tight-Binding Potential	3.232	5.147	97.5, 93.6, 95.8	130.1, 164.4	69.0, 62.1	65.7, 47.3	174.4, 189.8	26.1, 36.8	30.6, 51.2
1992	Wei and Chou [157]	DFT-LDA	-	-	-	144	74	67	166	33	35
1991	Willaime and Massobrio [158]	EAM (Potentials WM1 and WM2)	3.202	5.218	97, 101	154, 162	70, 77	65, 65	-	34, ,30	42, 42.5
1989	Oh and Johnson [159]	EAM	3.231	5.125	97.1	147.9	66.3	66.2	182.7	39.2	40.8
1983	Brandes [160]	Compilation of Experimental Publications	-	-	-	144	74	67	166	33	35
1982	H. W. King [161]	Compilation of Experimental Publications at 298K	3.2317	5.1476	-	-	-	-	-	-	-
1979	Hearmon [162]	-	-	-	98.4	144	74	67	166	33.4	35
1973	Jamieson and Olinger [163]	Compressibility & X-ray Diffraction*	3.231	5.148	97.6	-	-	-	-	-	-
1972	Vaidya and Kennedy [164]	Static Compressibility*	-	-	102	-	-	-	-	-	-
1972	Menon and Rao [165]	Keating's Approach	-	-	-	143.65	73.06	65.90	179.76	31.73	35.29
1970	Bezdek et al. [166]	Dispersion Relations using Inelastic Neutron Scattering*	-	-	-	136.5	49.5	-	191.9	33.4, 27.6	43.5
1970	Fisher et al. [167]	Ultrasonic Pulse Superposition Method with Crook's Method* at 298K	-	-	95.31	143.68	73.04	65.88	165.17	32.14	35.32
1969	Allard [168]	-	3.231	5.148	-	143.4	65.3	65.3	164.8	32	39.05

1964	Fisher and Renken [169]	Ultrasonic Wave Interference*	-	-	97	155.4 (4K) 143.4 (298K)	67.2 (4K) 72.8 (298K)	64.6 (4K) 65.3 (298K)	172.5 (4K) 164.8 (298K)	36.3 (4K) 32.0 (298K)	44.1 (4K) 35.3 (298K)

Note: The * means experimental result.

Table 8: bcc Zirconium Properties: Comparison of lattice constant and elastic constants.

Date	Reference	Comments	a [Å]	B [GPa]	C_{11} [GPa]	C_{12} [GPa]	C_{44} [GPa]	$C'=(C_{11}-C_{12})/2$ [GPa]
2015	Current Work	DFT-PBE	-	85	-	-	34	-
2015	Current Work	MEAM	3.582 (1273K)	80.8	93.6	72.4	70.6	10.6
2011	Wang et al. [140]	DFT-PAW-GGA-PBE	3.574	90.2	86.6	92.3	26.6	-2.85
2008	Hao et al. [142]	DFT-PAW-GGA-PBE	3.58	-	-	-	-	-
2007	Mendelev and Ackland [145]	EAM (3 Potentials)	3.592, 3.562, 3.576	-	114, 96, 50	98, 109, 94	63, 42, 50	8, -6.5, -22
2005	Zhao et al. [148]	X-ray Diffraction and Birch-Murnaghan EOS*	3.627 (973K)	66 (973K)	-	-	-	-
2005	Greeff [149]	DFT-GGA	3.577	-	-	-	-	-
2004	Ikehata et al. [150]	DFT-PBE	3.58	-	84.2	91.4	32.3	-3.6
1993	Ahuja et al. [170]	DFT-LDA	-	-	-	-	32.8	-
1991	Heiming et al. [171]	Force Const. Dispersion Curves from Neutron Spectrometer* at 1213K, 1508K, and 1908K	3.574	-	104, 97, 100	93, 82 70	38, 40, 35	5.5, 7.5, 15
1989	Oh and Johnson [159]	EAM	3.58	-	-	-	-	-

Note: The * means experimental result.

Table 9: Zirconium vacancy formation energies.

Structure	Date	Reference	Comments	E_v^f [eV]
αZr (hcp)	2015	Current Work	DFT-PBE	1.7
	2015	Current Work	MEAM	1.65
	2012	Wen and Woo [172]	EAM	1.78-1.90
	2010	Mendelev and Bokstein [173]	EAM	2.41
	2007	Vérité et al. [144]	DFT-PBE-LDA DFT-PBE-GGA	2.29, 2.17
	2007	Woo and Liu [174]	EAM	1.7858
	2005	Domain and Legris [175]	DFT-PW-GGA	1.86
	1999	O Le Bacq et al. [176]	DFT-LDA-FPLMTO	2.07
	1999	Pasianot and Monti [154]	EAM	1.74
	1991	Willaime and Massobrio [158]	EAM	1.55-2.14
	1988	Hood [177]	PAS*	1.8-1.9 with 1.5 lower bound
βZr (bcc)	2015	Current Work	DFT-PBE	1.8
	2015	Current Work	MEAM	2.07
	1991	Willaime and Massobrio [158]	EAM	2.1

Note: The * means experimental result.

CHAPTER 6

THERMODYNAMICS OF URANIUM AND ZIRCONIUM

Melting

The melting temperature of the MEAM potential is determined using the thermodynamics of a two dimensional solid-liquid interface. In order to find the melting temperature for the MEAM potential, a solid/liquid interface is created (Figure 11). This interface can be simulated at various temperatures to obtain the melting temperature, which is determined by the temperature at which the solid and liquid phases can co-exist together with a stable interface.

The melting temperature was calculated using the moving interface method [58, 178] via an NPT ensemble with a solid/liquid interface and by analyzing the evolution of the interface. Initially, a 20x5x5 supercell of both γ-U and β-Zr were equilibrated at 1200 K in an NPT ensemble to generate a crystal system at high temperature. Next, half of the supercell was held at 1200 K, while the other half was equilibrated at 1600 K for U and 3000 K for Zr in an NPT ensemble, restricting supercell shape change to the x-direction. This created an interface of a crystal system and a liquid system. Then the solid/liquid interface system was equilibrated using an NPT ensemble at various temperatures for 1 ns. When the temperature of the system was equilibrated below the melting temperature, the solid phase propagated throughout the supercell and resulted in a solid crystal structure after 1 ns. However, when the temperature was above the melting temperature, the liquid phase propagated throughout the supercell.

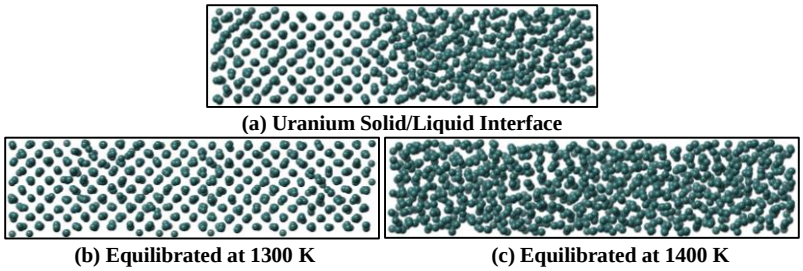

Figure 11: (a) Schematic of the γ-liquid uranium interface, where the γ-U left-hand side is equilibrated at 1200 K and the liquid right-hand side is equilibrated at 1600 K. The melting point is then identified using the γ-liquid uranium interface that was created. The periodic system was held in an NPT ensemble then equilibrated at specific temperatures, enabling the analysis of the γ-liquid uranium interface evolution to either the γ-U phase or the liquid-U phase. (b) Atomic configuration after the γ-liquid uranium interface had been equilibrated at 1300 K (below the MEAM potential melting point) for 1 ns, resulting in the domination of the f phase. (c) Atomic configuration after the γ-liquid uranium interface had been equilibrated at 1400 K (above the MEAM potential melting point) for 1 ns, resulting in the domination of the liquid-U phase.

This solid/liquid interface method allows for the melting temperature to be determined within a temperature range, since it is very difficult for a MD simulation to find the exact temperature where the liquid/solid interface remains stationary. The MEAM Zr potential was found to have a melting temperature between 2150 K and 2175 K, compared to the 2128 K experimental value [179]. The MEAM U potential was found to have a melting temperature between 1325 K and 1350 K, compared to the 1408 K experimental value [179].

Enthalpy

In addition to melting temperature, the enthalpy of fusion can also be obtained by calculating the change in the enthalpy of a liquid system at the melting temperature versus the enthalpy of the solid system at the melting temperature. These calculations determined that uranium has an 8.52 kJ/mol enthalpy of fusion and a 2.66% volume change upon melting, and zirconium has a 14.85 kJ/mol enthalpy of fusion and a 3.16% volume change upon melting. Uranium's volume change upon melting is close to the 2.2% experimental value obtained by Rohr et al. [180]. In addition, zirconium's volume change upon melting is reasonably consistent with the 3.9% experimental value from Efimov et al. [181].

There have been some inconsistencies in the value of the enthalpy of fusion for uranium, both taken experimentally and when constructing alloy phase diagrams. The experimental data are given in Table 10. The MEAM results compare favorably with the more recent experimental work.

Table 10: Uranium enthalpy of fusion.

Date	Reference	Value [kJ/mol]	Date	Reference	Value [kJ/mol]
2015	Current Work	8.52	1964	Levinson* [182]	8.326
2014	Fernández and Pascuet [59]	6.5	1963	Savage and Seibel* [183]	12.134
2012	Beeler et al. [58]	8.66	1963	Rand and Kubaschewski* [184]	10.46
1976	Marchidan and Ciopec* [185]	7.029	1960	Kelly* [186]	13.598
1974	Stephens* [187]	9.142	1956	Stull and Sinke* [188]	15.48
1973	Hultgren et al.* [189]	8.518	1954	Rauh and Thorn* [190]	19.665
1972	Radenac and Berthaut* [191]	7.276			

Note: The * means experimental result.

Zirconium's enthalpy of fusion experimental measurements have been much more consistent than uranium's. The experimental data are given in Table 11.

Table 11: Zirconium enthalpy of fusion.

Date	Reference	Value [kJ/mol]	Date	Reference	Value [kJ/mol]
2015	Current Work	14.85	1987	Guillermet* [192]	21
2013	Arblaster* [193]	15.6	1985	Katz et al.* [194]	14.674
2009	Klein et al.* [195]	14.652	1983	Efimov et al.* [181]	14.567
2005	Mompean et al.* [196]	19.8	1976	Alock et al.* [197]	18.828
2003	Brunner et al.* [198]	13.319	1973	Hultgren et al.* [189]	15.33
2001	Rösner-Kuhn et al.* [199]	17.282	1972	Martynyuk and Tsapkov* [200]	21.5
2001	Korobenko et al.* [201]	13.957	1967	Elyutin et al.* [202]	21.087
1998	Chase and Joint Army Navy Air (JANAF)* [203]	20.92	1967	Hultgren et al.* [204]	16.945
1991	Korobenko and Savvatimski* [205]	12.771			

Note: The * means experimental result.

The heat of fusion value for Zr is also in good agreement with the most recent experimental data. Since these values were not fit, this shows the possible level of prediction offered by the MEAM potential.

The calculated enthalpy as a function of temperature is presented in Figure 12. The enthalpy versus temperature graphs were obtained by performing MD simulations at various temperatures in an NPT ensemble. Then, the enthalpy was calculated by taking the internal energy plus the pressure multiplied by the volume for each simulation. From these data, the average MEAM heat capacity at constant pressure can be calculated, as well as the enthalpy of fusion.

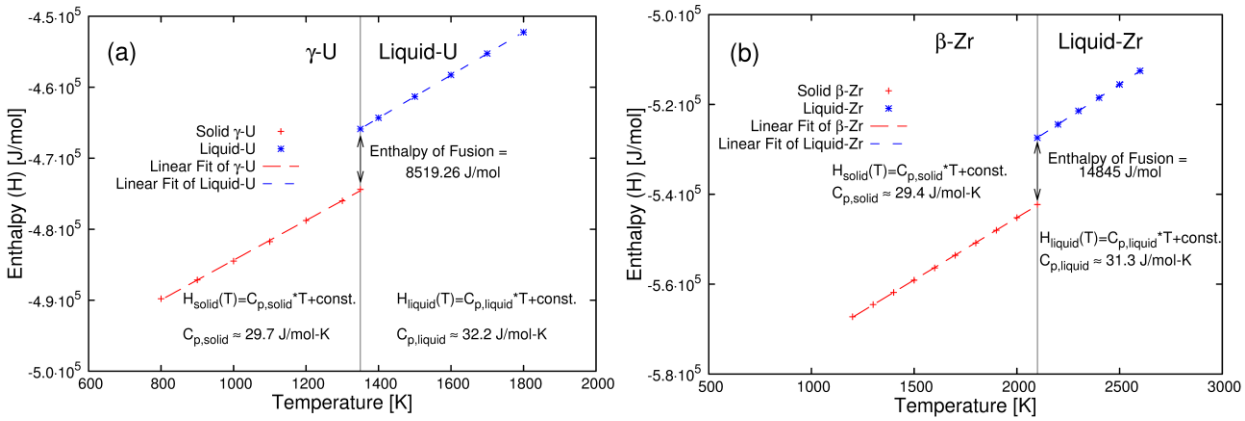

Figure 12: Enthalpy versus temperature for the (a) γ-U and liquid-U phases from 800 K to 1800 K and the (b) β-Zr and liquid-Zr phases from 1200 K to 2600 K obtained by MD using the MEAM potential. The slope in the enthalpy versus temperature of a given phase allows an approximate constant pressure heat capacity (C_p) to be calculated, while the jump in the enthalpy between the solid and liquid phases gives the enthalpy of fusion for the given MEAM potential.

Heat Capacity

The majority of the high temperature solid and liquid heat capacity contributions have been shown to be due to lattice effects, anharmonic effects, expansion, and defects (for solids); however, for metals, conduction electrons can also play a significant role. The MEAM heat capacity is obtained from the change in the enthalpy of the system over a change in temperature in an NPT ensemble with the pressure fixed. The MEAM potential is not fit to the heat capacity, but normally inherently fits the heat capacity for many metals. MD simulations in an NPT ensemble include the lattice vibrational effects, anharmonic effects, and expansion effects. The defect contribution is considered to be negligible compared to the electronic and lattice effects for the solid phase and therefore is not considered.

There has been a series of reported electronic heat capacity coefficients (γ_e) for the ground state α-U [185, 206-214] and α-Zr [215-217]; however, there have been no reported values for the higher temperature bcc phases. In the past, in order to overcome this problem, the ground state γ_e values were used to estimate the higher temperature phases [185, 218].

A rough estimate of the electronic heat capacity coefficient (γ_e) is developed using basic Fermi-Dirac statistics in the free electron model, where the density of states (DOS) around the Fermi energy is taken from Xie et al. [55]. The heat capacity from electrons is caused by the ground state conduction electrons being excited; therefore, the electronic heat capacity is proportional to the DOS at the Fermi energy since those electrons are likely to be the ones that become excited above the Fermi level.

$$C^{(electronic)} \approx \frac{\pi^2}{3} k_B^2 * T * D(\varepsilon_f) = \gamma_e * T \qquad (47)$$

In the equation above, ε_f is the Fermi energy, $D(\varepsilon_f)$ is the DOS at the Fermi energy, and γ_e is the electronic heat capacity coefficient.

The previous reported α-U γ_e's have been shown to be microstructurally dependent [206] with an average value between all of the experimental results [185, 206-214] of about 10.12 mJ/mol-K^2, and of about 2.77 mJ/mol-K^2 for α-Zr. The result for the γ-U γ_e's using Equation (47) was a lower value of 7.62 mJ/mol-K^2, while β-Zr resulted in nearly the identical value of 2.76 mJ/mol-K^2. Thus we expect that at around 1000 K the calculated MEAM molar heat capacity will be about 8 J/mol-K lower than experiment for U and 3 J/mol-K lower than experiment for Zr.

The heat capacity is then calculated by summing together the MEAM and electronic contributions. This is shown in Figure 13 and Figure 14 as a function of T. Figure 13 and Figure 14 show C_p for U and Zr respectively, calculated as described above, along with experimental values of C_p. The heat capacities for U (Figure 13) and Zr (Figure 14), with the addition of the conduction electronic effects, match the experimental heat capacities for the solid phases fairly well. However, the liquid heat capacity tends to be slightly under-predicted, which is most likely a result of a change in the electronic heat capacity contribution between the bcc solid phases and the liquid phase.

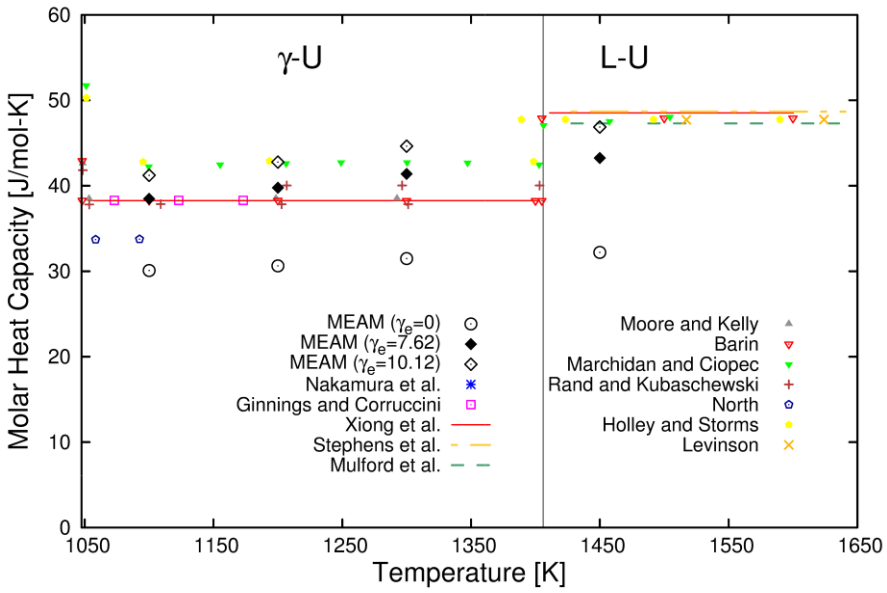

Figure 13: The constant pressure heat capacity versus temperature for the α-U, β-U, γ-U, and liquid-U phases [21, 26, 182, 184, 185, 218-224]. The γ_e represents the electronic heat capacity coefficient with which the molar heat capacity was calculated. Vertical lines represent the transition between phases at various temperatures. The experimental uranium heat capacity tends to show some variance in their values.

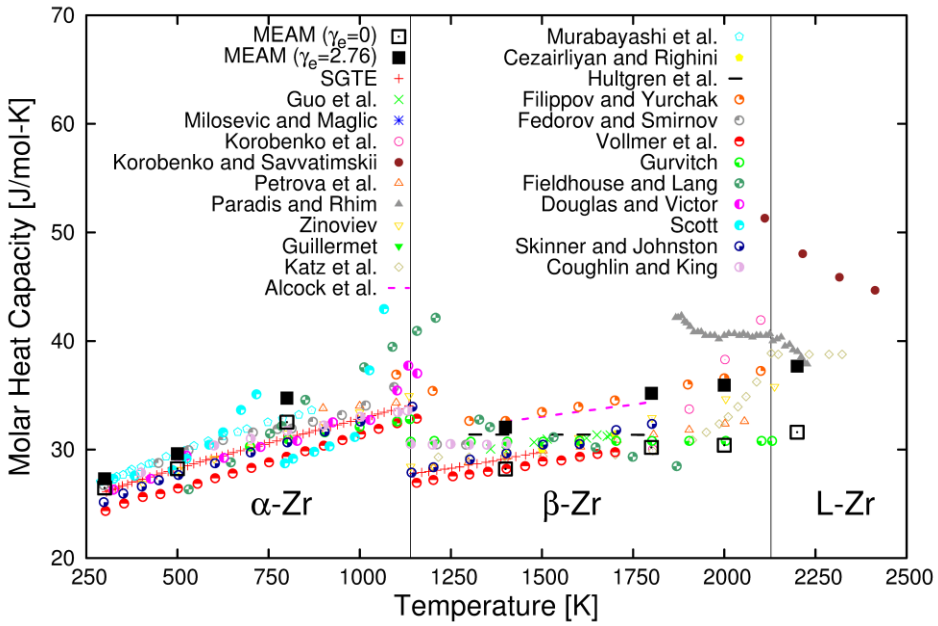

Figure 14: The constant pressure heat capacity versus temperature for the α-Zr, β-Zr, and liquid-Zr phases [21, 189, 192, 194, 197, 201, 225-244]. The γ_e represents the electronic heat capacity coefficient with which the molar heat capacity was calculated. Vertical lines represent the transition between phases at various temperatures.

CHAPTER 7

THERMAL STRUCTURE CHARACTERIZATION OF THE BCC AND LIQUID PHASES OF URANIUM AND ZIRCONIUM

In order to develop confidence in our methods, we start by simulating pure U in the γ-U and liquid-U phases and compare our results with EAM and quantum molecular dynamics (QMD) results [63, 245]. Elemental U is equilibrated at various temperatures in these configurations. The resulting structure is analyzed using the radial distribution function (RDF) g(r) and the bond-angle distribution function (BADF) $g_3(\theta)$. The RDF, g(r), is defined as the relative probability of finding an atom at a distance r from another atom, and the BADF, $g_3(\theta)$, is defined as the relative probability of finding a bond angle θ that an atom makes with its neighbors located within a maximum bond length [246]. The g(r) and the $g_3(\theta)$ are calculated at various temperatures for the pure elemental liquid and bcc U. The $g_3(\theta)$ was calculated using a 4.2 Å maximum bond length (R_m), which was determined by approximating the first minimum in g(r) (Figure 15). The effect that the maximum bond length has on the BADF can be seen in Figure 16.

Figure 16, showing the BADF as a function of radial distance, allows for discrimination of 1NN and 2NN. The 55 degree peak, which is the largest peak, is due to the angle between the 1NN and 2NN atoms. Then there are the 70 and 109 degree peaks, which are due to the angle between the 1NN atoms. The 90 and 173 degree peaks correspond to the angle between the 2NN atoms. Lastly, the 122 degree peak corresponds to the angle between the 1NN and 2NN atoms.

The melting transition to the liquid phase from the solid bcc phase is not forced, but is allowed to occur naturally. The transition to the liquid state can be determined using the $g_3(\theta)$ (Figure 17) as seen in the 1400 K and 2150 K for pure U. The bonding angles from the solid bcc

phase to the liquid phase change significantly. In the liquid phase, the bonds change to a more bimodal distribution with peaks around 55° and 110° ending with a trailing tail.

The g(r) (Figure 15) and the $g_3(\theta)$ (Figure 17) structural data obtained from the MD MEAM potential's runs for U is compared to those obtained using a QMD method by Hood et al. [245] and to the EAM potential by Smirnova et al. [63]. The MEAM and QMD g(r) both change smoothly with increasing temperature, indicating no solid-solid transitions. Similar to these studies, we find that the last peak in the $g_3(\theta)$ around 180°, characteristic of a cubic or tetragonal solid, disappears from the bcc solid to the liquid state for U. In addition, the liquid states also show a bond-angle short range ordering (SRO), resulting in a characterizable structure (Figure 18). The liquid structure is found to be a collection of tetrahedra with common vertices, whose bond-angle SRO decreases slowly as the temperature of the liquid increases.

The MEAM shows similar trends to the g(r) and the $g_3(\theta)$ of the QMD and EAM results. There are however a few discrepancies that can be attributed to the MEAM having a lower melting point than the EAM and the experimental melting point of 1407.95 K [13]. We estimate that the MEAM melting point is between 1325-1350 K [50], while the EAM has a melting point around 1500 K [63]. The QMD melting point was not given [245].

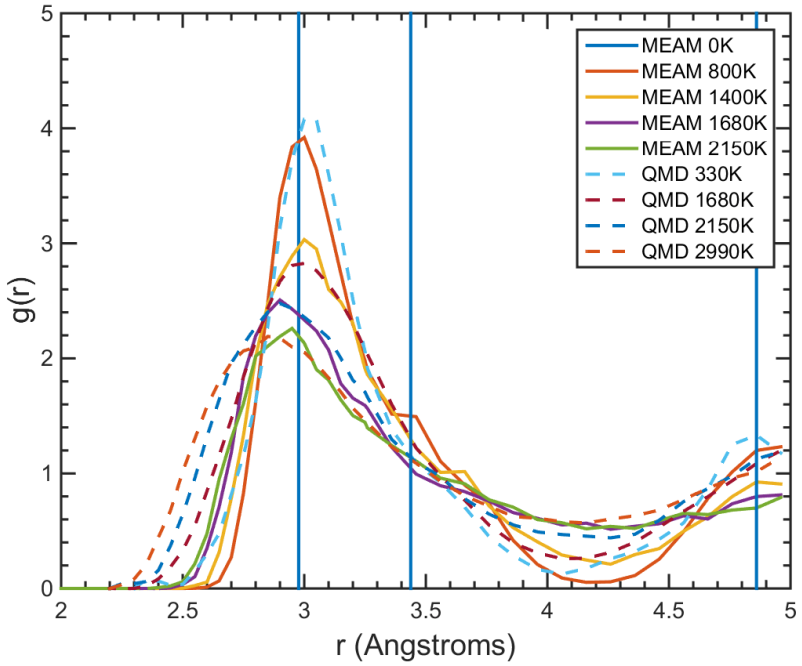

Figure 15: RDF g(r) for uranium calculated at different temperatures using the MEAM potential in MD simulations compared with the QMD results. The vertical lines are the RDF positions for the MEAM potential at 0 K.

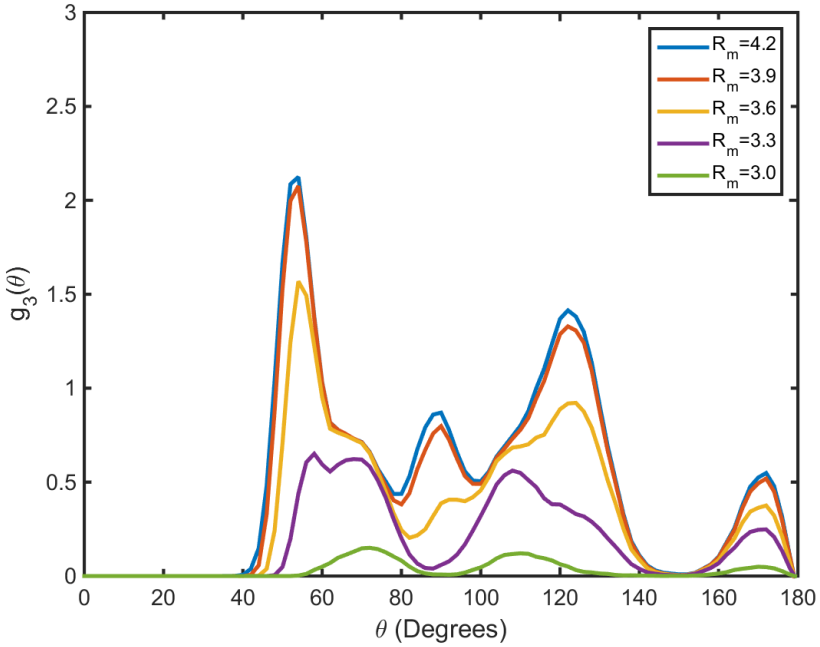

Figure 16: BADF $g_3(\theta,R_m)$ for the bcc U phase at 800 K, calculated for different values of the maximum bond length R_m.

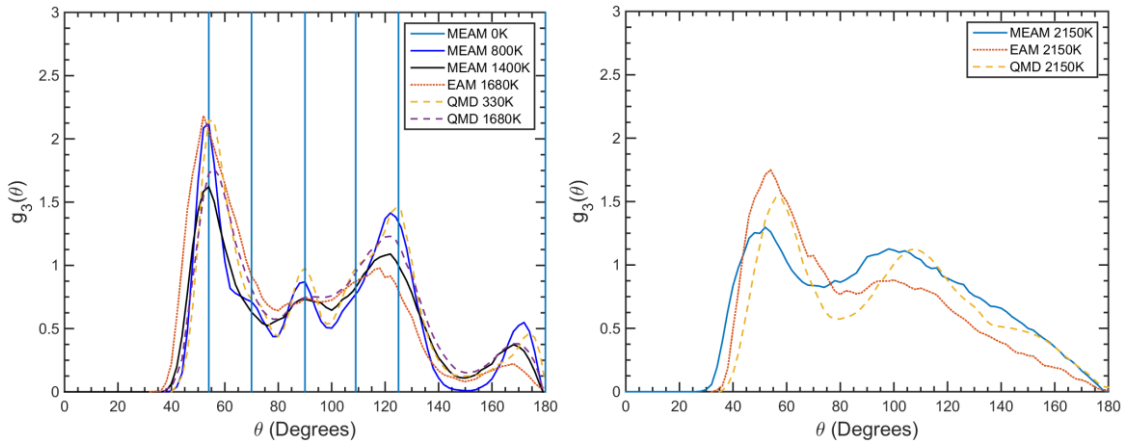

Figure 17: BADF $g_3(\theta)$ for (a) bcc uranium calculated at different temperatures and for (b) liquid uranium calculated at 2150 K using the EAM, MEAM, and QMD results. The vertical lines are the BADF positions for the MEAM potential at 0 K.

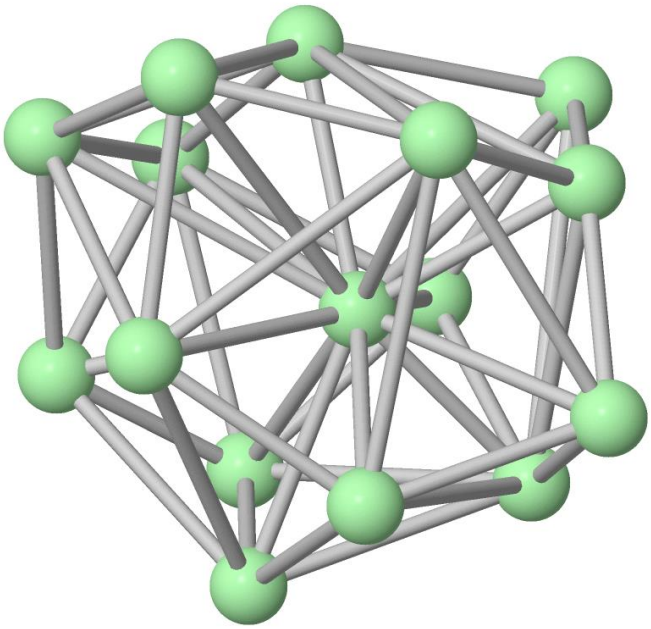

Figure 18: Snapshot of the liquid-U structure at 2300 K, showing the bonds within a 4.2 Å maximum bond length (R_m) of the central atom and the network of tetrahedrals characterizing the bonding in the liquid phase.

Similarly, the bcc and liquid phases of zirconium were also analyzed. However, previous publications of RDFs and BADFs for comparison were not found for these phases. The RDF (Figure 19) changes smoothly with increasing temperature indicating no solid-solid transitions between the 800 K-2150 K temperature range. Once again the melting transition was not forced, but was allowed to occur naturally. The transition to the liquid state can be determined using the $g_3(\theta)$ (Figure 20) as seen in the 3000 K for pure Zr. The bonding angles from the solid bcc phase to the liquid phase change significantly. Similarly to the uranium liquid phase, in the zirconium liquid phase, the bonds change to a more bimodal distribution with peaks around 55º and 110º ending with a trailing tail. The zirconium liquid phase was also found to be characterizable as a collection of tetrahedra with a common vertex (Figure 21).

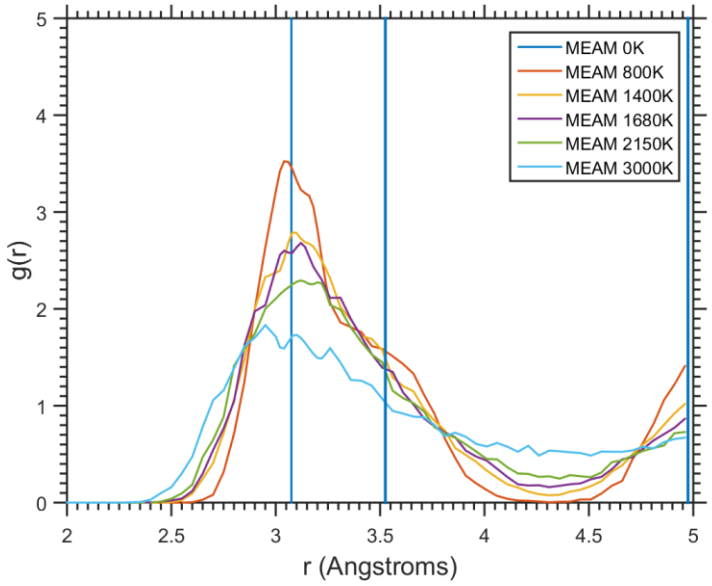

Figure 19: RDF g(r) for zirconium calculated at different temperatures using the MEAM potential in MD simulations. The vertical lines are the RDF positions for the MEAM potential at 0 K.

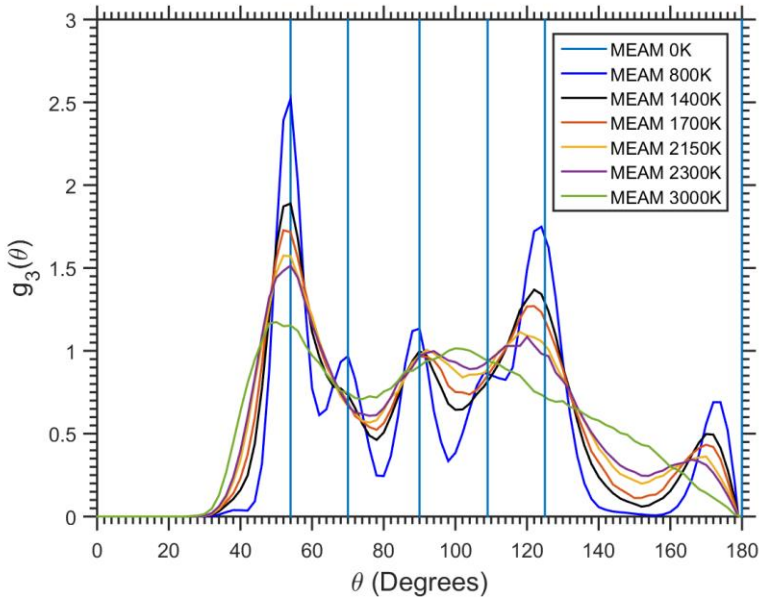

Figure 20: BADF $g_3(\theta)$ for bcc and liquid zirconium calculated at different temperatures. The vertical lines are the BADF positions for the MEAM potential at 0 K.

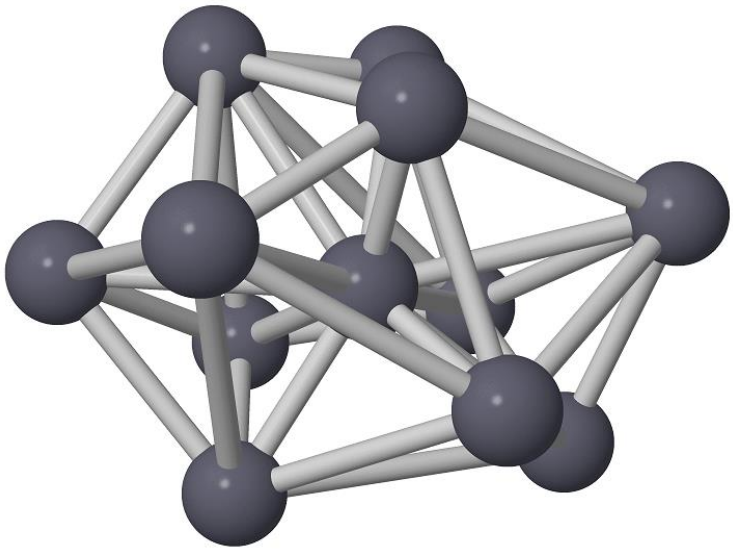

Figure 21: Snapshot of the liquid-Zr structure at 3000 K, showing the bonds within a 4.2 Å maximum bond length (R_m) of the central atom and the network of tetrahedrals characterizing the bonding in the liquid phase.

CHAPTER 8

STRUCTURAL PROPERTIES OF THE γ-U-ZR ALLOY

Lattice Constant

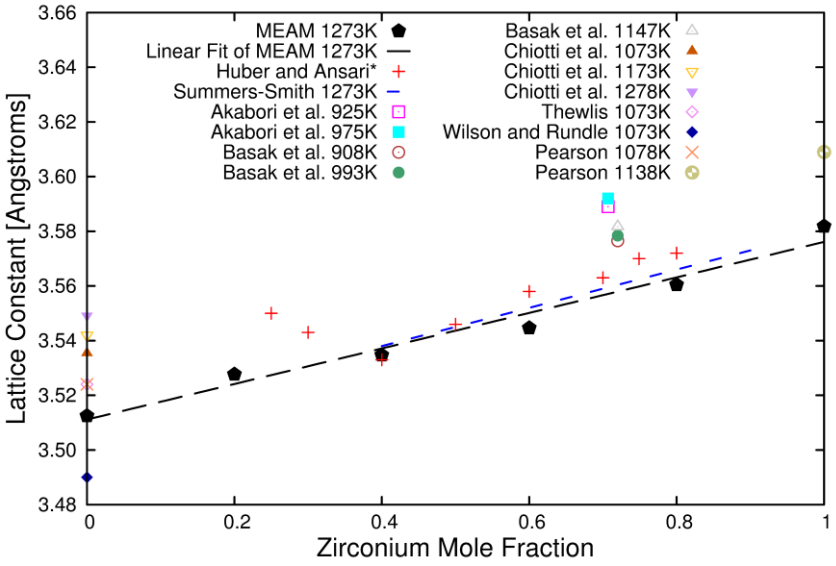

Figure 22: The lattice constant versus zirconium mole fraction for the γ-U-Zr alloys calculated by the current MEAM potential and previous experimental results [18, 19, 247-252]. The legend lists either the temperature from which the alloy was quenched (* indicates quenched from molten) or the temperature at which the lattice constant was obtained directly.

Figure 22 shows the results of the MD calculations and a comparison with experimental results [18, 19, 247-252]. The lattice constants for the MEAM potentials were obtained using the conventional time averaged unit cell box size during the 1273 K MD simulations held in an NPT ensemble. The unquenched MEAM lattice constants are seen to agree with Vegard's law as well as the experimental lattice constants. Summers-Smith [16] determined the lattice constant using powder x-ray diffraction analysis of arc-melted U-Zr that was homogenized and annealed at

1000 °C for 3 weeks. The lattice constants for the U-Zr 40 to 90 atomic percent (at. %) of the quenched bcc phase were found to vary linearly with composition, and were extrapolated using a linear fit to 3.51 Å at pure uranium and 3.58 Å at pure zirconium. Huber and Ansari [17] produced single-phase bcc solid solution U-Zr alloys using a rapid-quench-from-melt technique for compositions varying from 25 to 80 at.% Zr. Then, using x-ray diffraction, they obtained lattice parameters and were able to verify the sample was still in the bcc phase. However, they did note that the sample containing 40 at. % Zr or less had significantly broader bcc x-ray diffraction lines, which is where their lattice constants begin to deviate from the Summer-Smith values.

Akabori et al. [18] obtained the γ-U-Zr lattice constants for U-70.7 at.% Zr by using powder neutron diffraction analysis at temperature, which reduced the negative effects of surface oxidation and orientation dependence. Recently, Basak et al. [250, 253] examined the δ-phase and the transition from γ-phase to δ-phase and obtained the lattice constants from x-ray diffraction from U-50 weight percent (wt. %) Zr alloys quenched from 908 K, 993 K, and 1147 K.

Thermal Expansion

The thermal expansion coefficient was determined by the change in volume over a change in temperature per unit volume. The change in volume over a change in temperature was determined using multiple MD simulations held in an NPT ensemble above and below a midpoint temperature at which the thermal expansion was calculated. This process was repeated to obtain the thermal expansion values of the U-Zr alloy at 1000 K, 1100 K, 1200 K and 1300 K. The MEAM potential's parameter δ was varied to fit the experimental thermal expansion. Figure

23 shows the thermal expansion of the γ-U-Zr using the MEAM potential compared to experimental results obtained by other researchers. The Zr showed little variance of the thermal expansion coefficient within this temperature range; however, the U thermal expansion coefficient gradually increased with temperature. The experimental volumetric thermal expansion values were obtained by either quenched or at temperature lattice constants at differing temperatures.

Many of the thermal expansion values can be difficult to directly compare due to microstructural differences, phase changes, and different expansion reporting methods [18, 45, 49, 128, 240, 251, 254-259]. Bagchi et al. [49] showed that the U-Zr microstructure can play a large role in thermal expansion. For example, heat-treated alloys tend to show a significantly lower thermal expansion when compared to as-cast U-Zr.

The thermal expansion values shown in Figure 23 were obtained for a single crystal bcc solid solution (10x10x10 supercell) of the U-Zr alloy. The simulation was performed for 100 ps. Multiple simulations were performed and the average volume of the supercell calculated as a function of varying zirconium content. These were compared to four experimental calculations of thermal expansion: elemental U [251], elemental Zr [258], U-70.7 at. % Zr [18] and U-72.3 at.% Zr [250]. These experimental results were appropriate for comparison because they were obtained using experimental lattice constants at differing temperatures, which can be directly compared to the simulation of bulk thermal expansion values.

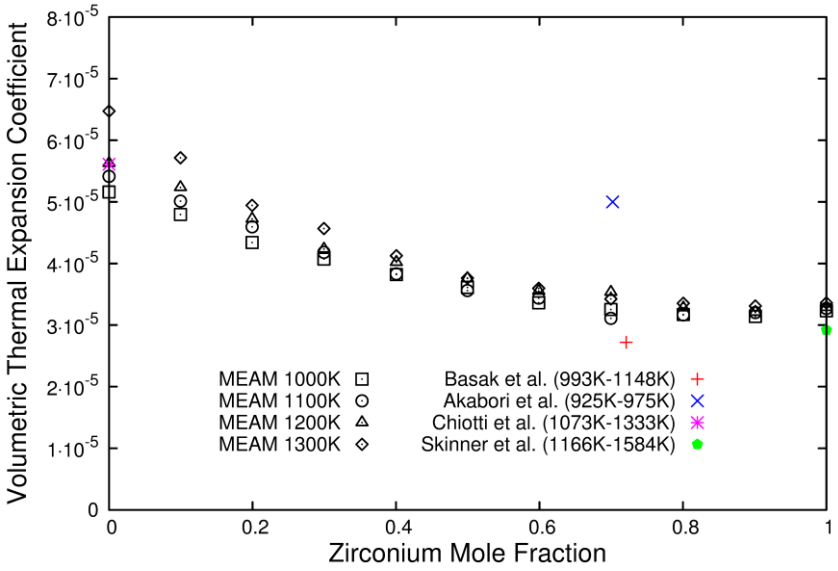

Figure 23: Instantaneous volumetric thermal expansion coefficient versus zirconium mole fraction for the γ-U-Zr alloys for the current MEAM potential between the temperatures 1000 K-1300 K, and the experimental instantaneous thermal expansion coefficients [18, 250, 251, 258].

CHAPTER 9

γ-U-ZR SOLID SOLUTION THERMODYNAMICS

Enthalpy

The enthalpy of mixing was obtained by using the basic definition of enthalpy and ensemble averages for volume (V), pressure (P), and internal energy (U). The pure U and Zr ensemble time-averaged properties at a given temperature were taken and set to the component properties (e.g. P_i, V_i, and U_i). The alloy's ensemble time-averaged properties for a given composition (X) and temperature were taken and set to the "mixed" properties (e.g. P_{mix}, V_{mix} and U_{mix}). This method allows for a representative model of the MEAM potential on the enthalpy of mixing, given by

$$\Delta H_{mix} = U_{mix} - \sum_i X_i U_i + P_{mix} V_{mix} + \sum_i X_i P_i V_i \qquad (48)$$

where, for the MD simulations held in a NPT ensemble, the pressures P_{mix} and P_i are approximately zero.

The predicted mixing enthalpy and Gibbs energy are given in Figure 24 and compared with the available experimental data. The graph illustrates the good agreement of the current MEAM potential with the experimental values given by Chiotti et al. [22]. In order to compare the MEAM potential results to experimental Gibbs energy values from Chiotti et al. [22], we used the entropy of mixing given by Chiotti et al. [22] and the MEAM heat of mixing to obtain Gibbs energy values. Due to simulation difficulties, the entropy of mixing for the MEAM potential is not directly calculated.

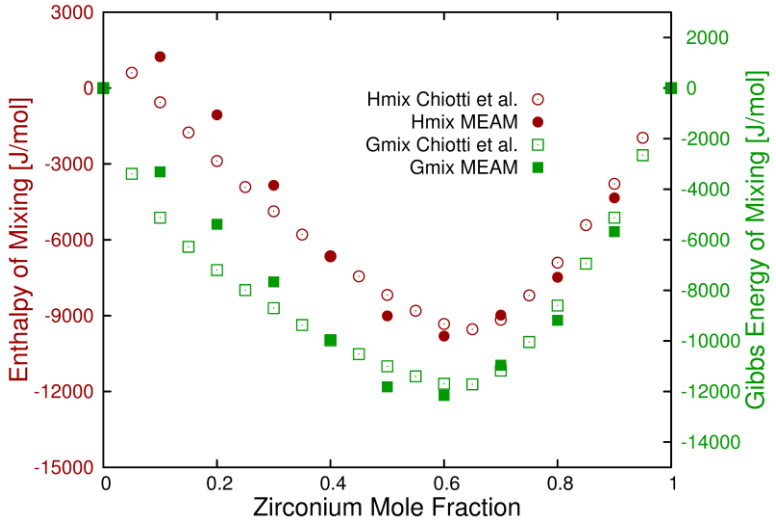

Figure 24: The enthalpy of mixing and Gibbs energy of mixing at 1100 K versus the zirconium mole fraction.

U-Zr Heat Capacity

The heat capacity for the U-Zr alloys is obtained in the same way the elemental heat capacities were obtained. However, alloying the metals creates an issue since they often show non-linear electronic heat capacity coefficient values with respect to mole fraction [260]. Therefore, the electronic heat capacity coefficient for the γ-U-Zr alloy was obtained by using Equation (47) with the DOS from Xie et al. [55], resulting in the electronic heat capacity coefficient estimation shown in Figure 25. The third order polynomial, fit to the electronic heat capacity coefficient in Figure 25, is used in the following γ-U-Zr alloy figures in order to add the estimated conduction electron effects to the heat capacities.

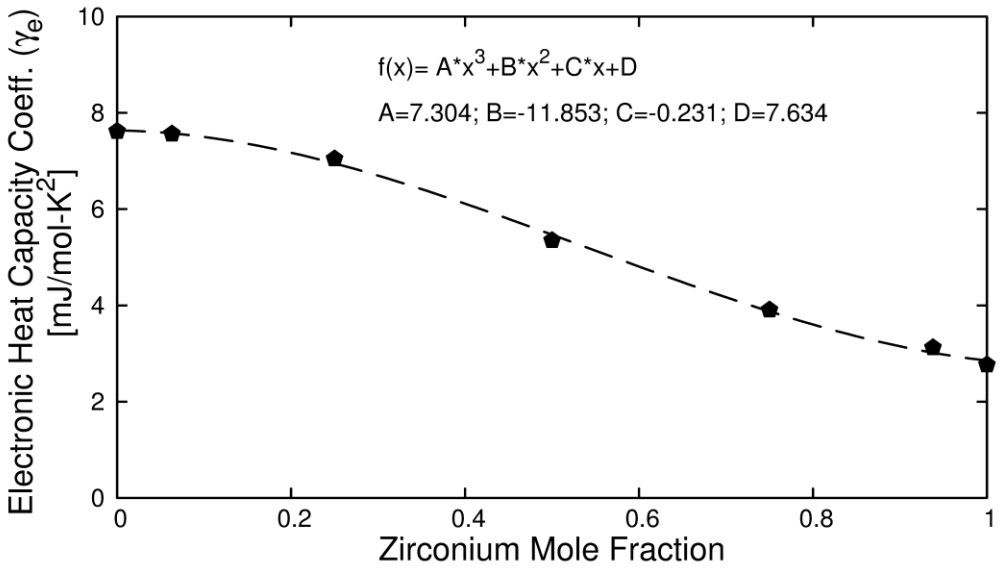

Figure 25: Electronic Heat Capacity Coefficient versus the Zr mole fraction for the γ-U-Zr alloy.

Figure 26 shows the heat capacity calculated using the MEAM potential. Two MEAM results are plotted, one with γ_e contributions, the other without. In addition, experimental values are also plotted.

There are only a few published heat capacity measurements for the high temperature U-Zr alloys. It can be noted that the experimental heat capacity values of the bcc U and Zr tend to be higher than most other bcc metals. The first U-Zr heat capacity measurements were published by Fedorov and Smirnov who used a heat pulsed method [21]. Next, Takahashi et al. measured the high temperature heat capacity for a few concentrations of U-Zr by laser-flash method [261]. The values from Takahashi et al. were found to be lower than the ones reported by Fedorov and Smirnov. Since Takahashi, there have been four additional experimental heat capacity values published for two different U-Zr compositions. Matsui et al. [262] determined the heat capacity of $U_{0.8}Zr_{0.2}$ alloy from 300 K to 1300 K by heating-pulse Calorimetry, which corresponds reasonably well with Fedorov's data. The rest of the heat capacity values were determined using

a heat flux type differential scanning calorimetry (DSC). Kaity et al. [45] determined the heat capacity of U–14.3 at.% Zr alloy which was significantly different from both Fedorov's and Takahashi's values. Lee et al. [263] determined the heat capacity of U-40 wt.% Zr in both irradiated and unirradiated samples, and the unirradiated results were similar to those of Takahashi and the current MEAM potential. Most recently, Dash et al. [264] determined the heat capacity of U-7 wt.% Zr alloys, which were found to be similar to the results of Matsui et al. [262] and Kaity et al. [45].

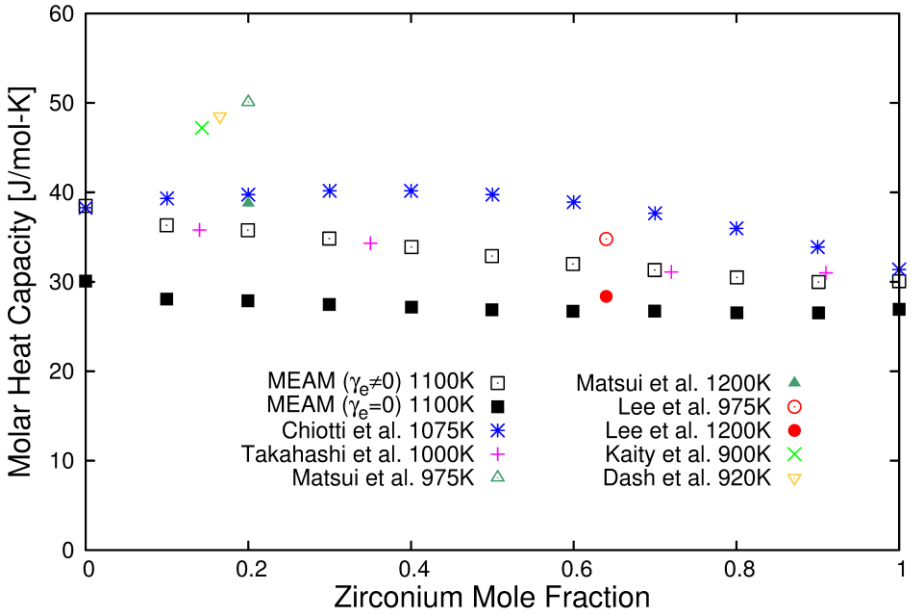

Figure 26: The molar heat versus zirconium mole fraction for the γ-U-Zr phase [22, 45, 261-264]. The $\gamma_e \neq 0$ versus $\gamma_e = 0$ represents the value with the electronic heat capacity coefficients obtained from Figure 25 versus without, respectively. The MEAM potential, while slightly underestimating the average experimental values, is in good agreement with the experimental values and trend obtained from Takahashi et al. [261] and Lee et al. [263].

The molar heat capacity reported by the Fedorov and Smirnov, Chiotti et al. and Matsui et al. using the heat pulse method has a concave shape across the U-Zr alloy concentration

spectrum, while the molar heat capacity from the MEAM potential and molar heat capacity from Takahashi et al. using the laser-flash method show a convex shape. The MEAM potential results match up well with the convex shape of the molar heat capacity versus mole fraction obtained by Takahashi et al.

Additional U-Zr Thermodynamic Properties

Figure 27 shows the MEAM molar heat capacities for the γ-U-Zr phase calculated at 1100 K, by fixing either the volume for the constant volume heat capacity or by fixing the pressure for the constant pressure heat capacity. This allows for the change in enthalpy and the change in energy with respect to temperature to be calculated.

The instantaneous volumetric heat capacity (C_V) is calculated by the change in internal energy over the change in temperature at a constant volume. The change in energy over temperature is accomplished by first equilibrating the system at a specific temperature and then fixing the volume of the system and varying the temperature by 10 K above and below the volume equilibrated system temperature, resulting in the equation below.

$$C_V = \left(\frac{\partial E}{\partial T} \right)_V \qquad (49)$$

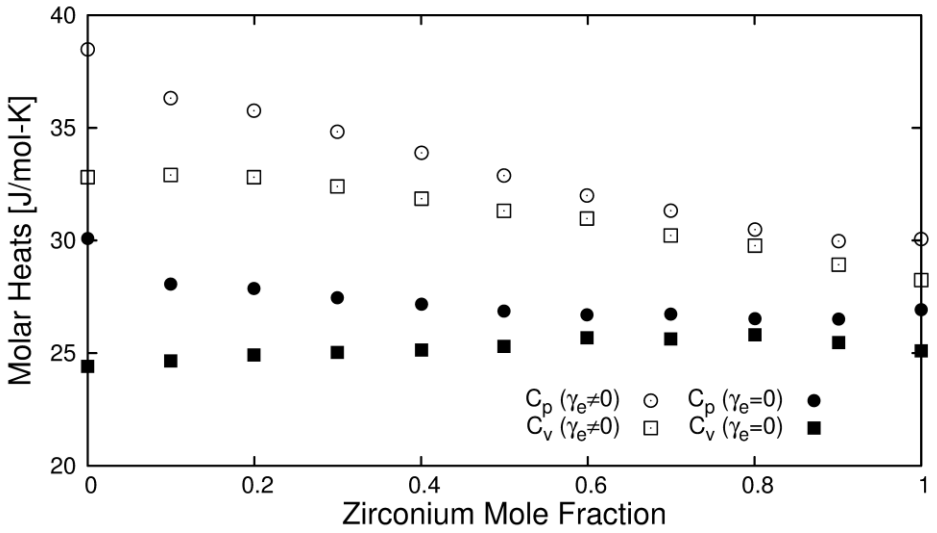

Figure 27: The constant pressure heat capacity and the constant volume heat capacity versus zirconium mole fraction for the γ-U-Zr phase obtained using the MEAM potential. The $\gamma_e \neq 0$ versus $\gamma_e = 0$ represents the value with the electronic heat capacity coefficients obtained from Figure 25 versus without, respectively.

The U-Zr volumetric heat capacity ($\gamma_e = 0$) obtained is around the value one would expect from harmonic oscillator theory and from other metals. Simple harmonic oscillator theory combined with the equipartition principle allows for a basic estimation of volumetric heat capacity of solids at non-low temperatures and non-high temperatures, as seen below [265].

$$C_V \approx \frac{\partial}{\partial T}\left(\frac{f}{2} k_B T N_A\right) = 3R = 24.94 \frac{J}{mol * K} \quad (50)$$

In the equation above f is the degrees of freedom per atom, R is the gas constant, N_A is Avogadro's number, and k_B is the Boltzmann's constant.

Figure 28 shows the MEAM heat capacity ratio (or adiabatic index) for the U-Zr system. The heat capacity ratio is calculated by taking the constant pressure heat capacity over the constant volume heat capacity.

$$\frac{C_p}{C_V} = \frac{\beta_T}{\beta_S} = \frac{B_S}{B_T} = \gamma \qquad (51)$$

In the above equations, γ is the heat capacity ratio or adiabatic index, β_T is the isothermal compressibility, β_S is the isentropic compressibility, B_T is the isothermal bulk modulus, B_S is the adiabatic bulk modulus, and S refers to entropy.

The heat capacity ratio of the γ-U-Zr phase for the MEAM potential was calculated at 1100 K, while the heat capacity ratio of the liquid-U phase was calculated at 1810 K to allow direct comparison to the experimental result by Boivineau et al. [266].

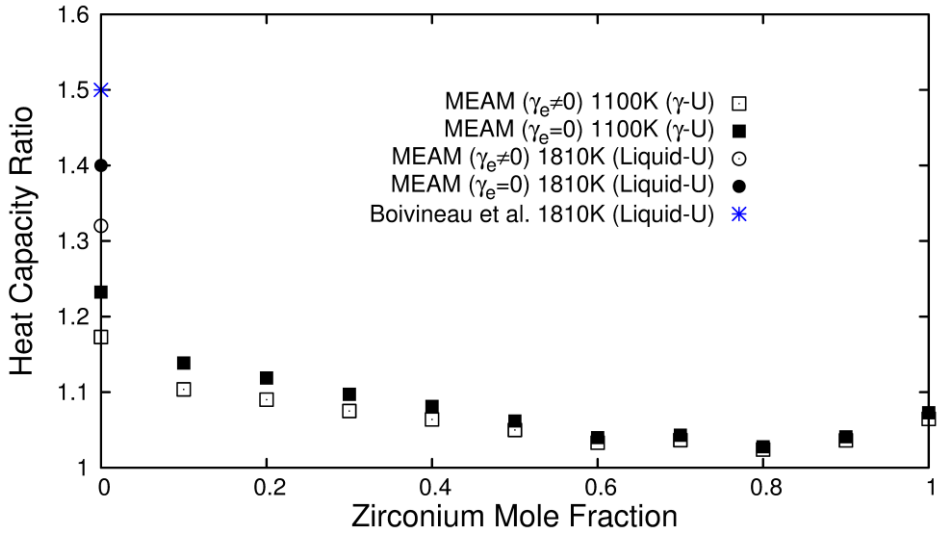

Figure 28: The heat capacity ratio (or adiabatic index) versus zirconium mole fraction for the γ-U-Zr phase and the liquid-U phase. The $\gamma_e \neq 0$ versus $\gamma_e = 0$ represents the value with the electronic heat capacity coefficients obtained from Figure 25 versus without, respectively.

Even though the heat capacity is slightly undervalued for the MEAM potential, the heat capacity ratio is in reasonably good agreement with the liquid-U phase experimental value presented by Boivineau et al. [266].

Figure 29 shows the isothermal compressibility of the γ-U-Zr alloy at 1100 K. The isothermal compressibility was calculated by scaling the simulation size volume in an NVT ensemble and equilibrating with a 100 ps MD run, then finding the inverse of the bulk modulus obtained from the Birch-Murnaghan EOS. The relationship between β_T and B_T can be seen in Equation (52) below. In addition, the relationship between β_S and B_S can be seen in Equation (53) below.

$$\beta_T = \frac{1}{B_T} = \frac{-1}{V}\left(\frac{\partial V}{\partial P}\right)_T \quad (52)$$

$$\beta_S = \frac{1}{B_S} = \frac{-1}{V}\left(\frac{\partial V}{\partial P}\right)_S \quad (53)$$

The isothermal bulk modulus is found to decrease with temperature for the γ-U-Zr phase, which agrees well with the experimental decrease found for Zr [169].

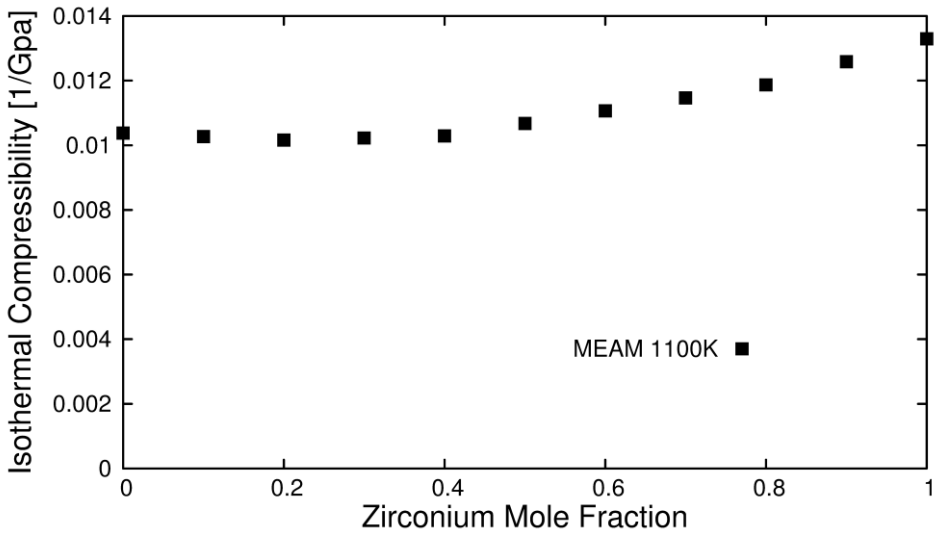

Figure 29: The isothermal compressibility versus zirconium mole fraction for the γ-U-Zr phase at 1100 K. The isothermal compressibility can also be recognized as the inverse of the isothermal bulk modulus.

Grüneisen Parameter

The Grüneisen parameter (γ_G) can also be predicted for the U-Zr system at temperature. The Grüneisen parameter was predicted at 1100 K and 0 GPa using the heat capacity ratio to convert the isothermal compressibility to the adiabatic bulk modulus, then the adiabatic bulk modulus, equilibrium volume, instantaneous volumetric thermal expansion coefficient (α_V), and the constant pressure heat capacity were used in Equation (54) below.

$$\gamma_G = V\left(\frac{\partial P}{\partial E}\right)_V = \frac{V}{C_V}\left(\frac{\partial P}{\partial T}\right)_V = \frac{V\alpha_V B_T}{C_V} = \frac{V\alpha_V B_S}{C_p} \quad (54)$$

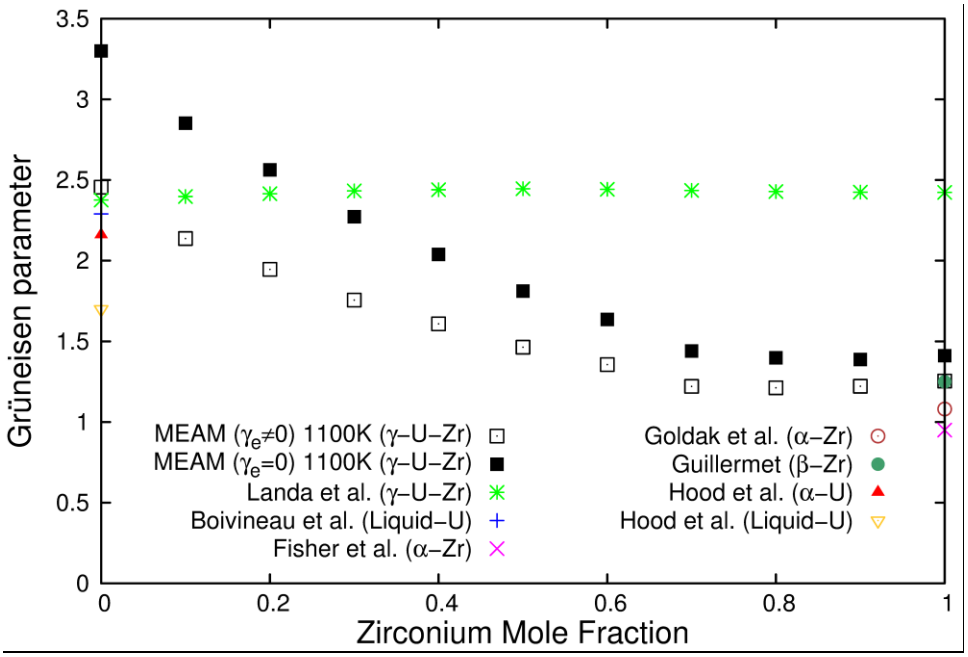

Figure 30: The Grüneisen parameter versus zirconium mole fraction for the γ-U-Zr phase, the α-Zr phase, the β-Zr phase, the α-U phase, and the liquid-U phase [51, 167, 192, 245, 266, 267]. The $\gamma_e \neq 0$ versus $\gamma_e = 0$ represents the value with the electronic heat capacity coefficients obtained from Figure 25 versus without, respectively.

The Grüneisen parameters for α-Zr [167, 267, 268] and for β-Zr [192] suggest that the γ-U-Zr DFT ground state Grüneisen parameter obtained by Landa et al. [51] using the Debye-Grüneisen quasi-harmonic model is too high. However, the MEAM obtained Grüneisen parameter for β-Zr agrees well with the Guillermet [192] experimental value at 1000 K.

CHAPTER 10

DISCUSSION OF γ-U-ZR THERMODYNAMICS

Previous simulations of U-Zr alloys have had some disagreements in their results [26, 51, 55, 57, 269]. In addition, the enthalpy of mixing for 0 K and temperature simulations versus the experimental high temperature results for the γ-U-Zr alloys show significantly different trends. There has been some debate on the entropy of mixing for the γ-U-Zr alloy [22, 26, 31, 270]. Initially it was believed that the U-Zr bcc solid solution phase was entropy stabilized. However, the values obtained by Chiotti et al. [22] suggest that the γ-U-Zr phase may be more complex than originally postulated.

Landa et al. [51] performed geometry optimization calculations using DFT-GGA and 1728 site Metropolis MC simulations from effective cluster interactions (ECI) and effective pair interactions (EPI) to obtain the ground state configuration and enthalpy of mixing curve, which was used to justify possible separation effects seen in the metallic fuel. In 2013, Xiong et al. [26] performed a summary of thermodynamic modeling of the U-Zr system [26] using the CALPHAD method [271] to obtain a set of self-consistent thermodynamic parameters to describe the phase equilibria of the U-Zr system. The paper noted some of the experimental and modeling discrepancies of the U-Zr system and calls into question the accuracy of some of the experimental results. A DFT study by Xie et al. [55] in 2013 showed the mechanical instability of γ-U-Zr at low temperatures where the 0 K U-Zr simulations were performed with only volume relaxation due to the mechanical instability of the phase. Then in 2014, Söderlind et al. [269] contested the studies performed by Xie et al. and Xiong et al. due to their negative enthalpies and their volume expansions, particularly for the γ-U phase.

DFT simulation results [26, 51, 55, 57, 269] show 0 K enthalpy of mixing for the γ-U-Zr solution to be positive, which suggests that the high temperature bcc phase is entropy stabilized. This positive enthalpy of mixing also supports the existence of the miscibility gap. However, the experimental enthalpy of mixing curve given by Chiotti et al. [22] has negative values for most of the U-Zr compositions in the bcc phase at temperature. This signifies that there exists complex bonding and electron behavior for the high temperature bcc phase. This complex phenomenon is believed to be due to the delocalized f-electron behavior [57, 272-275]. From the previous first principle simulations [26, 55, 57], it has been noticed that the enthalpy of mixing is highly dependent upon spin orbit coupling (SOC) and correlation effects (DFT vs. DFT-U). The first principles ground state enthalpy of mixing values vary widely, most of which are positive, but some even show a slight negative trend. The MEAM potential and Chiotti et al. [22] enthalpy of mixing results are closer in nature to the enthalpy of mixing obtained by Xiong et al. [26] and Xie et al. [55] which begin to approach negative values, rather than Landa et al. [51]. In addition, the miscibility gap can be explained through the non-regular anisotropic behavior of the entropy and enthalpy of mixing.

In 2013, Moore et al. [56] constructed a preliminary MEAM semi-empirical potential for the U-Zr system. This potential was constructed using DFT simulations for ground state elastic constants and defect formation energies from Beeler et al. [131] as well as Landa's decomposition curve [51]. The potential was shown to match the low temperature unstable U-Zr bcc properties as well as show the overall ground state energy configuration of the atoms. However, this previous MEAM potential's enthalpy of mixing curve did not vary drastically with temperature and does not satisfy the experimental high temperature enthalpy of mixing values. The new potential is able to mimic the experimental thermodynamic enthalpy of mixing trend.

Transitioning the MEAM potential from matching the 0 K behavior to the experimental enthalpy of mixing shows the change in the f-electron symmetry parameter t^3 and therefore the f-electron behavior as well as the reference alloy bulk modulus. These changes could indicate how the bonding interactions change with temperature.

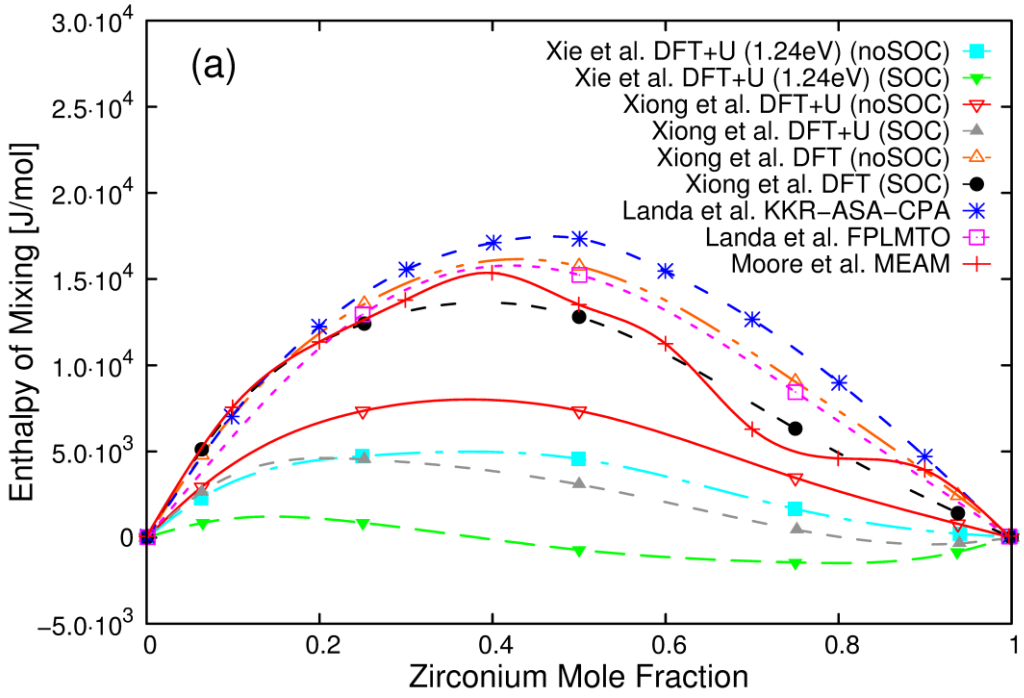

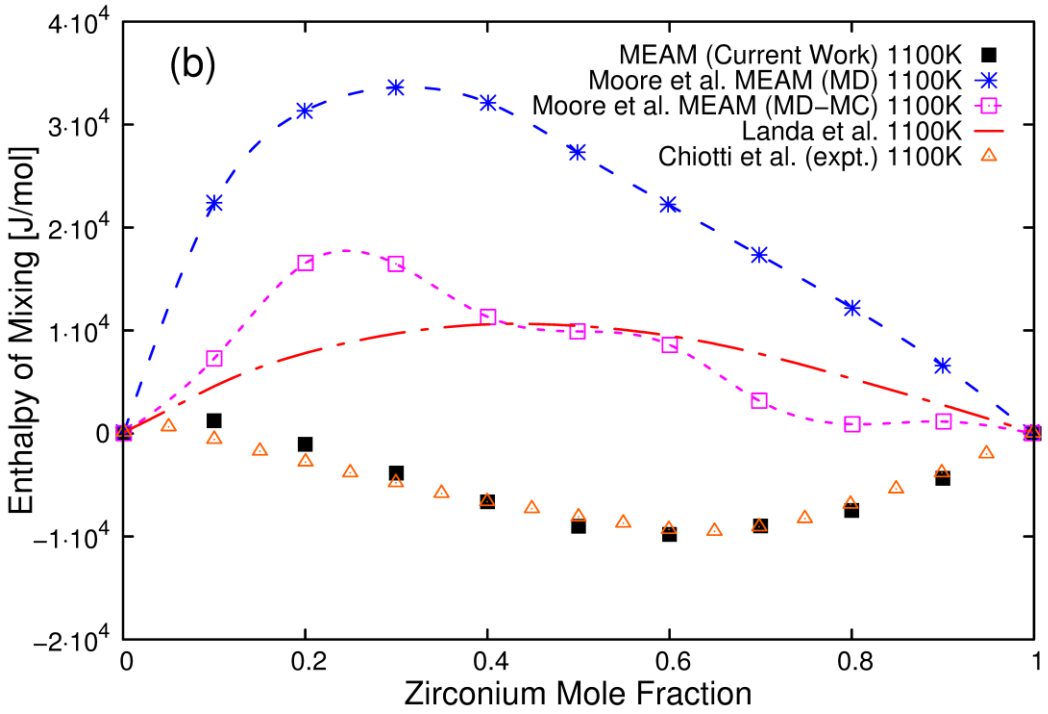

Figure 31: Enthalpy of mixing versus zirconium mole fraction for the γ-U-Zr alloys (a) for the 0 K ground state values obtained from published simulation results [26, 51, 55, 56] and (b) the high temperature values obtained from simulations and the experimental results [22, 51, 56].

Expansion of the U-Zr thermodynamics using the MEAM potential could include finding the Gibbs energy of the γ-U-Zr alloy simulation, but this is a challenging problem. This could be accomplished by combining a number of methods. The Gibbs energy of mixing can be calculated if the enthalpy of mixing, the temperature, and the entropy of mixing are known. The temperature and enthalpy of mixing are easily obtained. The entropy of mixing for the U-Zr configuration can be obtained by going back to the probability for each differing atomistic configurational state or by simplifying the configurations to only consider local environment and using the cluster variational method (CVM) [276]. After the Gibbs energy of mixing has been obtained for a single temperature, thermodynamic integration can be used to find the values at other temperatures inside the phase region.

CHAPTER 11

ORDERED/DISORDERED COMPARISON OF THE γ-U-ZR ALLOY

Now we focus attention on the thermodynamics, kinetics, and structure of the U-Zr configurations. We start with a random U-Zr configuration (also known as disordered configuration), which is allowed to naturally order with the given potential. Here we simulate the U-Zr alloy with iterative MC and MD simulations. The MC moves the ensemble to the lowest energy in an NVT ensemble. The same configuration is relaxed in MD to enable volumetric relaxation. The simulation begins with a 100 ps MD simulation in an isothermal-isobaric (NPT) ensemble. The resulting atomistic configuration is then used in an MC simulation in a canonical (NVT) ensemble for 500 steps per atom. Then the atomistic configuration is exchanged between the NPT MD simulation and the NVT MC simulation until the MC simulation has less than a 5 meV energy per atom change over the 500 MC steps per atom. The simulation ends with a final NPT MD simulation, resulting in the final structure and properties that are reported. The evolution of the average energy per atom in the system during the MC simulations as the ordering progresses can be seen in Figure 32.

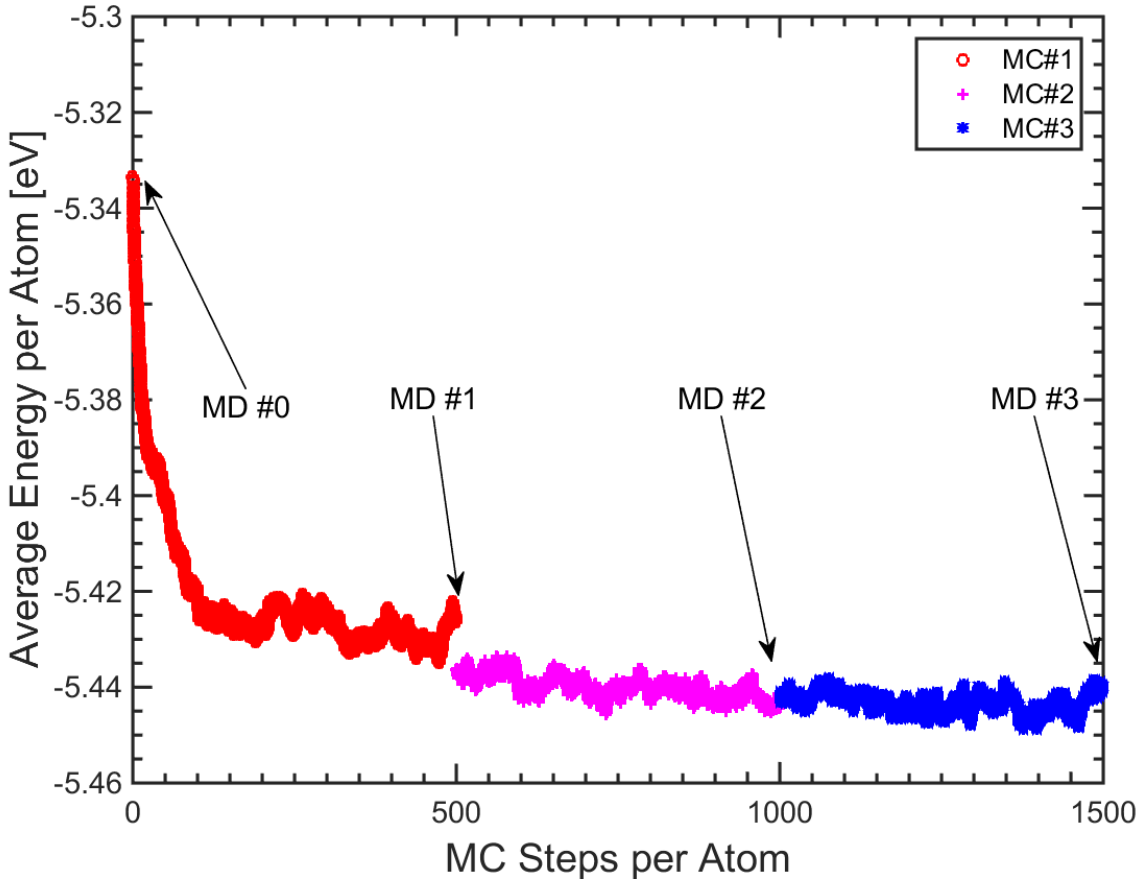

Figure 32: Average energy per atom of the U-20 at.% Zr system at 1100 K versus the number of MC steps per atom for each of the three MC simulations. The arrows show the configurations that are volumetrically relaxed using MD simulations.

The MD/MC simulations result in an ordered atomistic U-Zr configuration, which lowers the energy of the system. The average energy per atom is calculated at the end of the final MD simulation and the enthalpy of mixing, presented in Figure 33, shows a significant change from a disordered (random) U-Zr configuration to an ordered configuration. Thus, there is a thermodynamic driving force to order the U-Zr alloy, which could explain some of the separation and microstructural effects seen experimentally.

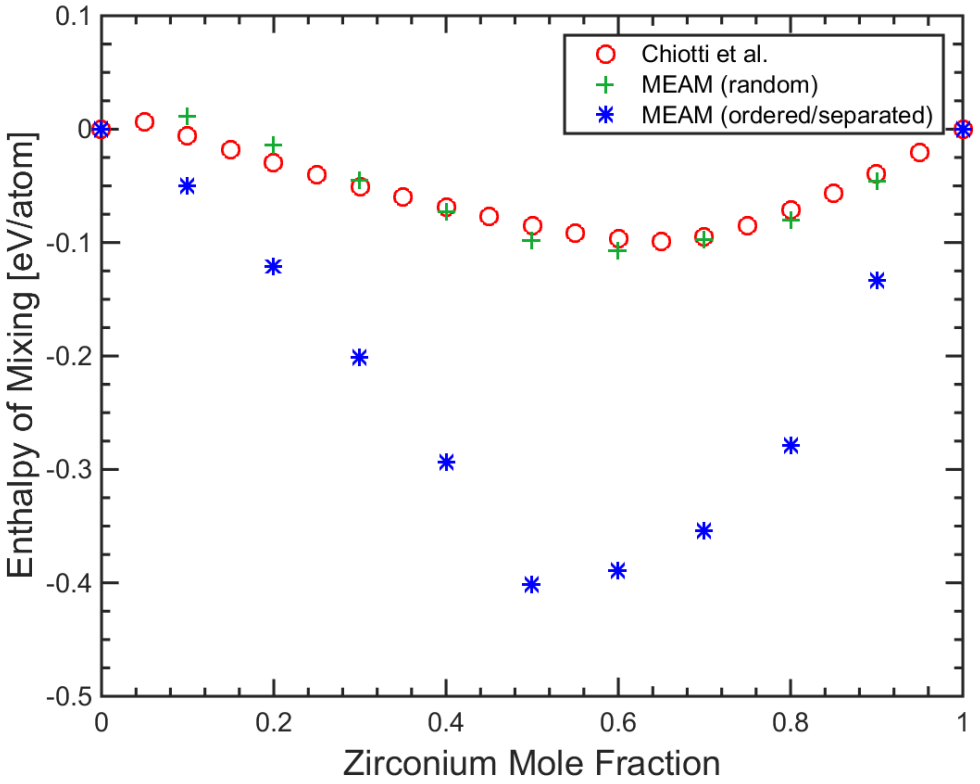

Figure 33: The enthalpy of mixing at 1100 K versus Zr mole fraction comparison for the random U-Zr configuration and the ordered/separated atomistic U-Zr configuration obtained using the MD/MC iterative simulations.

Configurational Short Range Order

In order to investigate the structure further, we compute the configurational SRO. The SRO of a few U-Zr alloys with respect to temperature gives an overview of the overall separation or ordering and how it is affected by temperature and concentration. The SRO parameter (σ) considers only 1NN [277-279].

$$\sigma = -\frac{P_{AA}-n_A}{1-n_A} \qquad (55)$$

P_{AA} is the fraction of the nearest neighbor sites of atom type A that is occupied by A type atoms (averaged over all A atoms). n_A is the atomic fraction of A type atoms in the entire

system. The SRO allows a single number to represent a large amount of order/disorder phenomena. Complete atomic separation of an infinite system results in $\sigma=-1$, while an ordered system of opposite 1NN results in $\sigma=1$.

In Figure 34 it is seen that, in the U-rich composition region, the SRO parameter is negative and hence there is U and Zr separation. Then as the Zr concentration increases, the SRO also begins to increase, leading to the more ordered section around the intermediate composition region. The ordering around the intermediate composition region is due to the thermodynamic driving force to partial ordering seen in the δ-UZr_2 C32 phase. Lastly, the SRO begins to decrease due to the partially ordered sections beginning to separate from the Zr bcc matrix in the Zr-rich composition region.

As seen in Figure 34, the SRO of the bcc solid solutions tends to increase with temperature. This increase in SRO can be attributed to the changing morphology and the deviation away from alternating (111) planes of atoms, which causes a push of the SRO closer to zero. The liquid solutions tend to be more random, causing the SRO to approach a zero value.

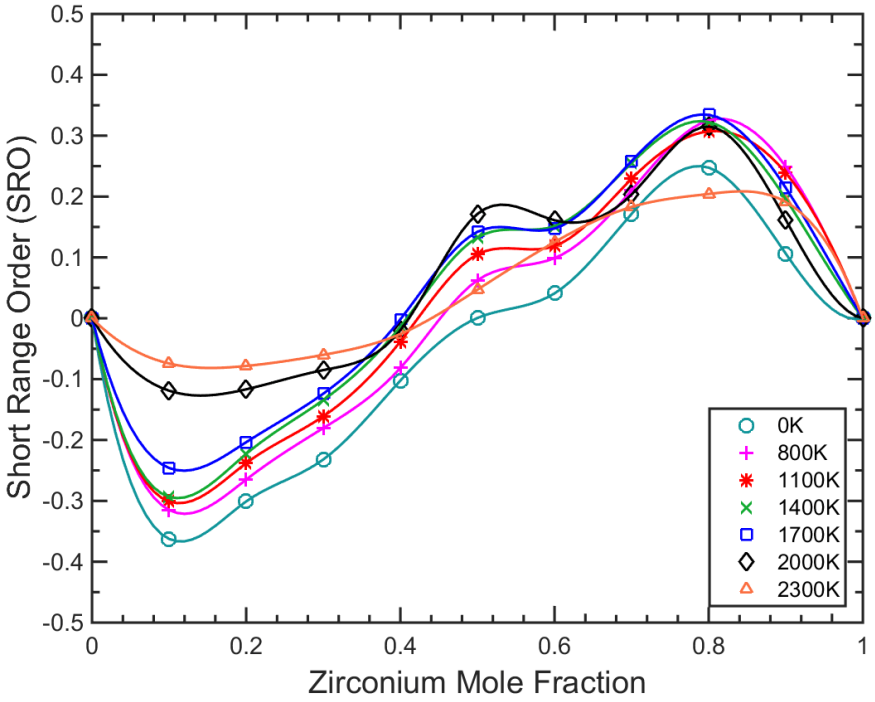

Figure 34: The SRO parameter of U-Zr alloy at 0 K, 1100 K, 1700 K, 2000 K, and 2300 K versus mole fraction of zirconium.

CHAPTER 12

ORDERING, SEPARATION, AND PRECIPITATE MORPHOLOGY IN THE γ-U-ZR SYSTEM

We can also study the ordering and separation morphology of the U-rich, intermediate, and Zr-rich U-Zr alloys. The ordering and precipitate morphology can be visualized as seen from the cross-sections of the atomistic configurations. These visualizations show the thermodynamic driving force toward certain separation or ordering behavior.

Atomistic configurations can be broken up into three regions: the U-rich region corresponding to the U-Zr concentrations on the U-rich side of the δ-UZr_2 phase (around 2 to 63 at.% Zr), the intermediate region within the δ-UZr_2 phase concentrations (around 64 to 78 at.% Zr), and the Zr-rich region corresponding to the concentrations on the Zr-rich side of the δ-UZr_2 phase (around 78 to 91 at.% Zr).

Ordering analysis is conducted using four methods: the SRO parameter allowing for general ordering and separation trends, RDFs, BADFs, and visual analysis. Full and partial g(r) and $g_3(\theta)$ distributions were calculated at various temperatures for the U-Zr alloys, offering more information on the structure and ordering of the U-Zr system. The partial BADFs consisted of six unique atomistic local configurations: U-U-U, U-Zr-U, U-U-Zr, Zr-Zr-Zr, Zr-U-Zr, and U-Zr-Zr. The BADFs were calculated using a 4.2 Å R_m.

Uranium-Rich Compositions

The atomistic configurations (Figure 35) of the U-rich U-Zr alloys show the spheroidization of the precipitates at lower temperatures versus the band-like lamellar

precipitation at high temperatures, while Figure 36 and Figure 37 show the complimentary RDFs and BADFs respectively. The U-10at.%Zr alloy is used to illustrate the typical U-rich precipitation phenomena. The atomistic configuration of the U-10at.%Zr at 0 K (Figure 35a) illustrates alternating U and Zr (111) planes of atoms in a faceted spherical-like arrangement that has precipitated from the U-Zr alloy. The faceted precipitate was found to have an approximately 25 Å size in the <100> directions and 21 Å size in the <110> directions. This behavior shows the thermodynamic driving force toward the spherical precipitates observed experimentally [44, 46, 47, 253, 256, 259, 280] and shown in Figure 2c. The precipitate has some preferred surfaces of separation on the (111), $(\bar{2}21)$, and (110) surfaces. As the Zr concentration increases, the faceted separation continues at low temperatures; however the morphology changes from the alternating planes being surrounded by U atoms to the U atoms being surrounded by alternating planes.

As the temperature increases, the morphology of the (111) alternating U and Zr planes begin to change. The precipitate begins to form band-like arrangements. The atomistic configuration of U-10at.%Zr at 1400 K illustrates alternating U and Zr (111) planes of atoms in a band-like arrangement (Figure 35c). The band-like precipitate was found to have an average thickness of about 12 Å in the [001] direction. These (111) atom planes can also be seen in the Zr-Zr-Zr, U-Zr-U, and Zr-U-Zr $g_3(\theta)$ (Figure 37). The Zr-Zr-Zr shows a distinctive singular peak around 109º, indicating 1NN Zr atoms lining up in a particular direction, and the Zr-Zr g(r) (Figure 36) shows that the Zr atoms are 1NN. Evidence of the 1NN Zr atoms lining up in a particular direction is also given by the U-Zr-U and Zr-U-Zr figures with their larger than average 90º peaks. These bands are easily seen in the [100] direction; however, the surfaces of preferred separation are still (111) and (110). As the temperature increases even higher, the

precipitation remains in the stable bcc band-like structure, but the separated uranium begins to change from bcc to a more liquid state. The band-like atomistic configuration shows the thermodynamic driving force to the lamellar [41-43] and acicular [16, 44, 46, 47, 256, 259, 281] microstructures observed experimentally and shown in Figure 2a and Figure 2b.

Above the melting point, there is an increase in atomistic motion, leading to an increase in atomic diffusion, that results in a random configuration of U and Zr atoms in the liquid structure (Figure 35d). The transition into atomistic randomness is captured by the $g_3(\theta)$ in Figure 37, where both the total and partial BADFs move to the characteristic shape of a binomial distribution with peaks around 55º and 110º with a trailing tail, indicating the liquid phase consists of a network of tetrahedrals.

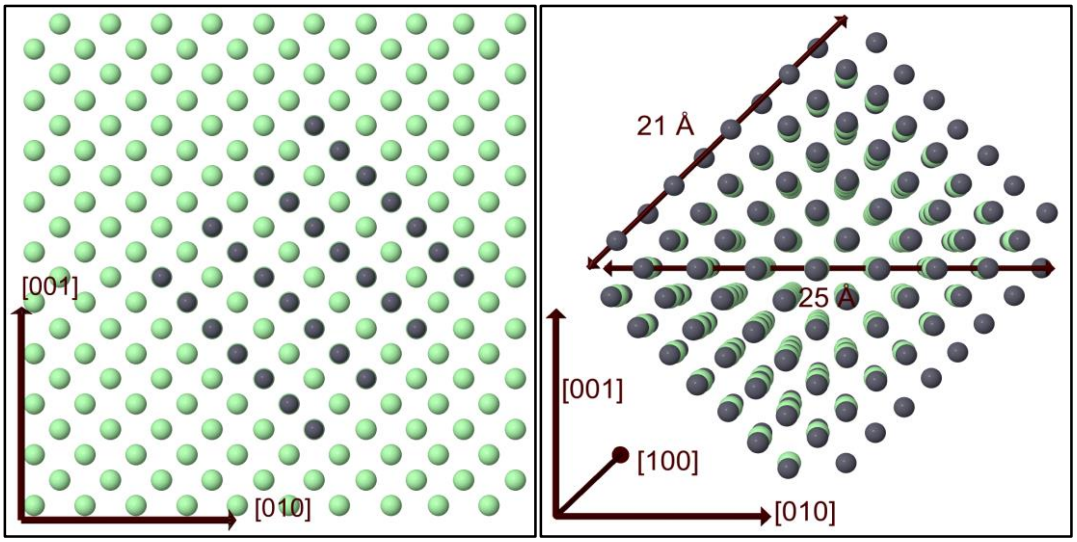

(a) **(b)**

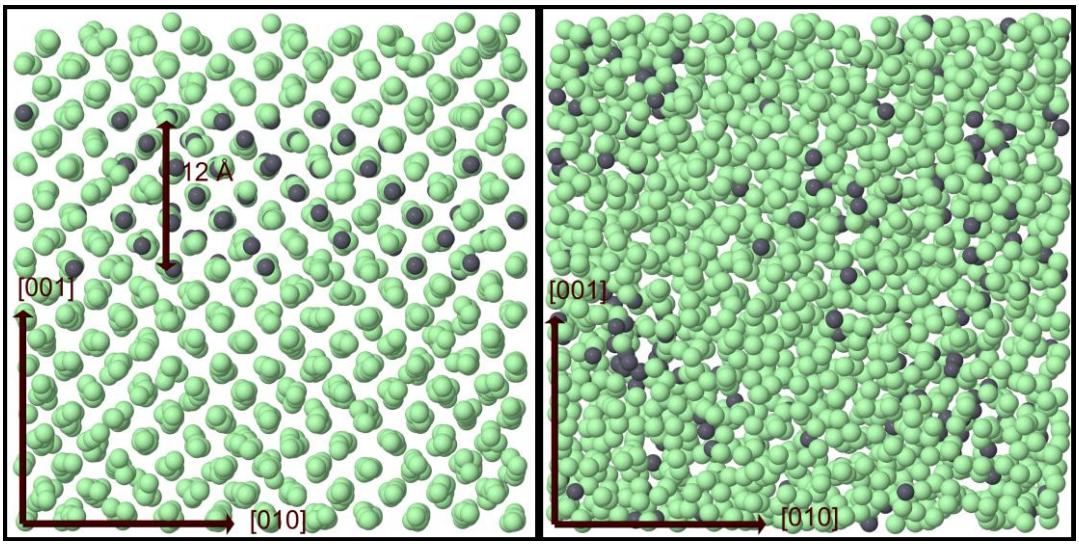

(c) **(d)**

Figure 35: [100] Snapshots of equilibrium U(light-green)-10at.%Zr(dark-grey) configurations at (a) 0 K, (b) 0 K precipitate, illustrating the alternating U and Zr (111) planes of atoms in a faceted spherical-like morphology, (c) 1400 K illustrating the band-like separation of the alternating U and Zr (111) planes, and (d) 2000 K illustrating the random liquid phase atomistic configuration.

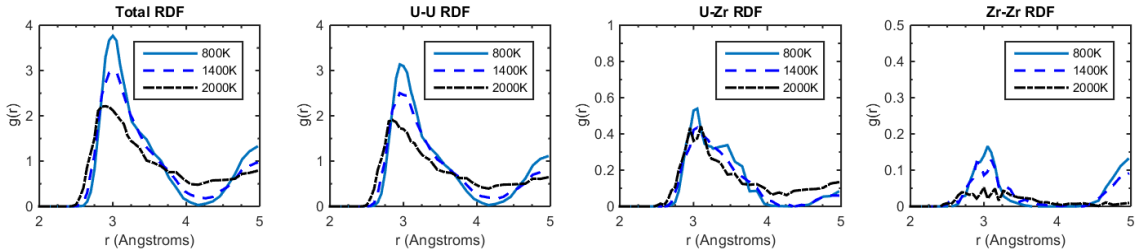

Figure 36: Full and partial RDFs of U-10at.%Zr at 800 K, 1400 K, and 2000 K.

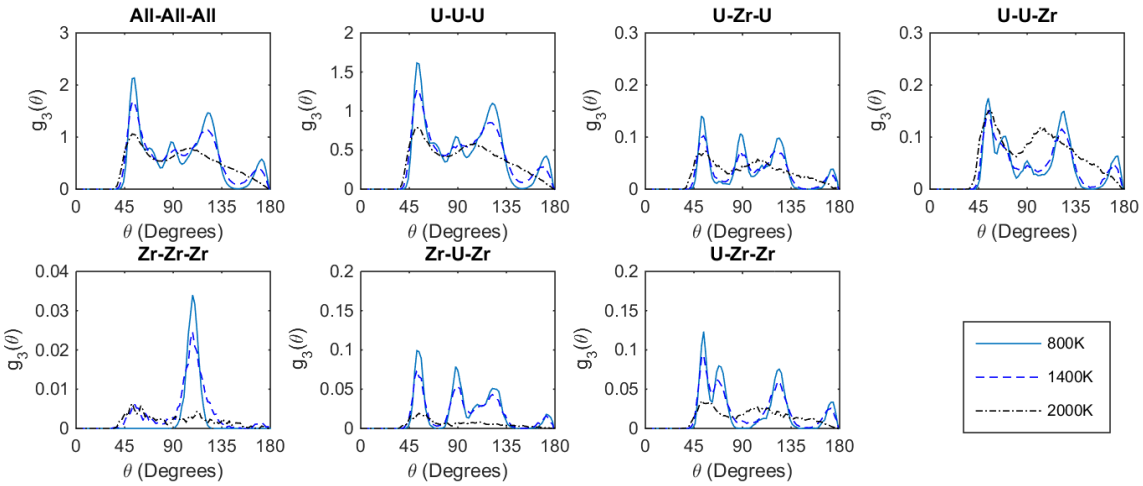

Figure 37: Full and partial BADFs of U-10at.%Zr at 800 K, 1400 K, and 2000 K.

The atomistic configurations of U-20at.%Zr, U-30at.%Zr, and U-40at.%Zr at 1400 K (Figure 38) are used to illustrate the typical morphological transition as Zr concentration increases at temperature. As the Zr concentration increases, the alternating U and Zr (111) planes forming the band-like precipitates begin to broaden with U-20at.%Zr having an average thickness of approximately 17 Å, and U-30at.%Zr having an average thickness of approximately 22 Å. Then as the zirconium content increases to U-40at.%Zr, the band-like separation transitions to a tubular morphology with an average diameter of about 17 Å. This tubular separation behavior, when taken as two-dimensional cross-sections, can be likened to the microstructure of the U-rich region approaching the compositions just outside of the intermediate region, which tends to have small discs and globules of separated U [47, 48].

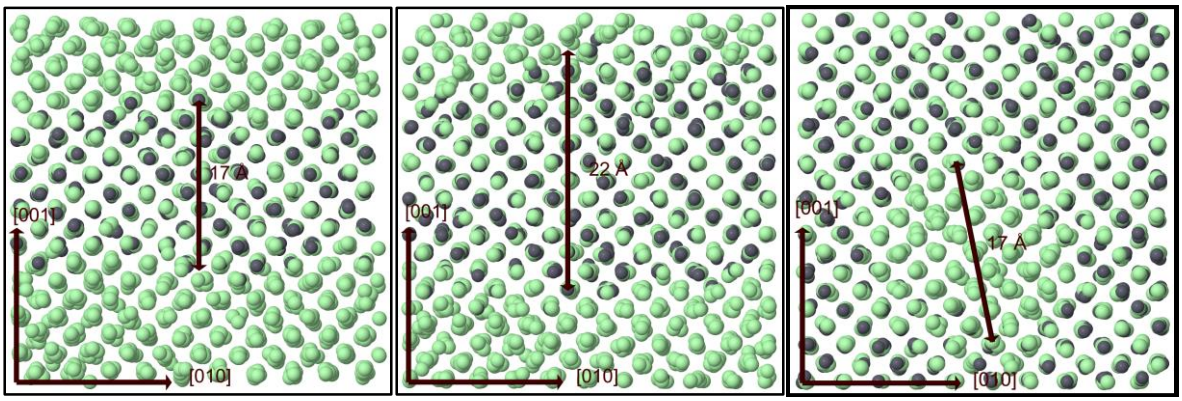

(a) **(b)** **(c)**

Figure 38: [100] Snapshots of 1400 K equilibrium configurations of (a) U(light-green)-20at.%Zr(dark-grey), (b) U-30at.%Zr, and (c) U-40at.%Zr. The atomistic configurations of U-20at.%Zr and U-30at.%Zr illustrate the broadening of the band-like separation morphology consisting of alternating (111) U and Zr planes of atoms as Zr concentration increases, and U-40at.%Zr illustrates the tubular separation morphology of pure U.

Intermediate Compositions

The atomistic configurations of the intermediate U-Zr alloy within the δ-UZr_2 phase concentration show more ordered atomic arrangement without precipitates (Figure 39), while Figure 40 and Figure 41 show the complimentary RDFs and BADFs respectively. The U-70at.%Zr alloy is used to illustrate the typical intermediate U-Zr alloy ordering phenomena. The atomistic configurations of U-70at.%Zr from 0 K-1400 K show the bcc structure with a preference for short sections of U and Zr (111) alternating planes and an overall preference for alternate 1NN types as seen in the SRO parameter (Figure 34) and the partial U-U g(r) (Figure 40). The atomistic snapshots in Figure 39 and the partial U-U g(r) depict that there is an ordering preference for U atoms to be 3NN and 4NN. This overall preference for opposite type 1NN, but still occasionally having U atoms as 1NN, and most often having them as 3NN, 4NN,

or even further, is important when considering the transition from bcc to the δ-UZr_2 phase through the omega transformation mechanism. If the bcc unit cells have U atoms with only one or two U 1NN, then this allows for the omega transformation to the ordered δ-UZr_2 phase seen in Figure 42. However, if the bcc unit cells have no U 1NN, the transition to the delta phase is still possible, but will result in a more random arrangement. During the omega transformation mechanism, alternating (111) planes of the bcc phase collapse to form the AlB_2 type hexagonal crystal structure, which has been documented by Basak et al. [250]. In the partially ordered δ-UZr_2 phase, the Zr atoms were found to occupy the (0,0,0) position, and a random mixture of U and Zr atoms were found to occupy the (2/3,1/3,1/2) and (1/3,2/3,1/2) positions. The current atomistic configuration in the bcc structure facilitates a more direct transition to the partially ordered δ-UZr_2 phase. No atomistic precipitation is witnessed in this intermediate region, allowing the microstructure to result in equiaxed grains as observed experimentally and shown in Figure 2d.

The RDFs (Figure 40) and BADFs (Figure 41) of the intermediate U-Zr system show the characteristic 55º and 110º peaks, indicating the liquid phase consists of a network of tetrahedrals. In addition, the partial RDFs and BADFs show the transition to atomistic randomness as temperature increases.

An ordered bcc phase with the U atoms having only one U 1NN and the rest of the 1NN and 2NN being Zr can be reoriented with the bcc $Pm\bar{3}m$ [111] direction equating to the $P\bar{3}m1$ [0001] of an equivalent trigonal unit cell (Figure 42). Using this equivalent unit cell, the collapsing of the alternate bcc (111) planes can be easily visualized.

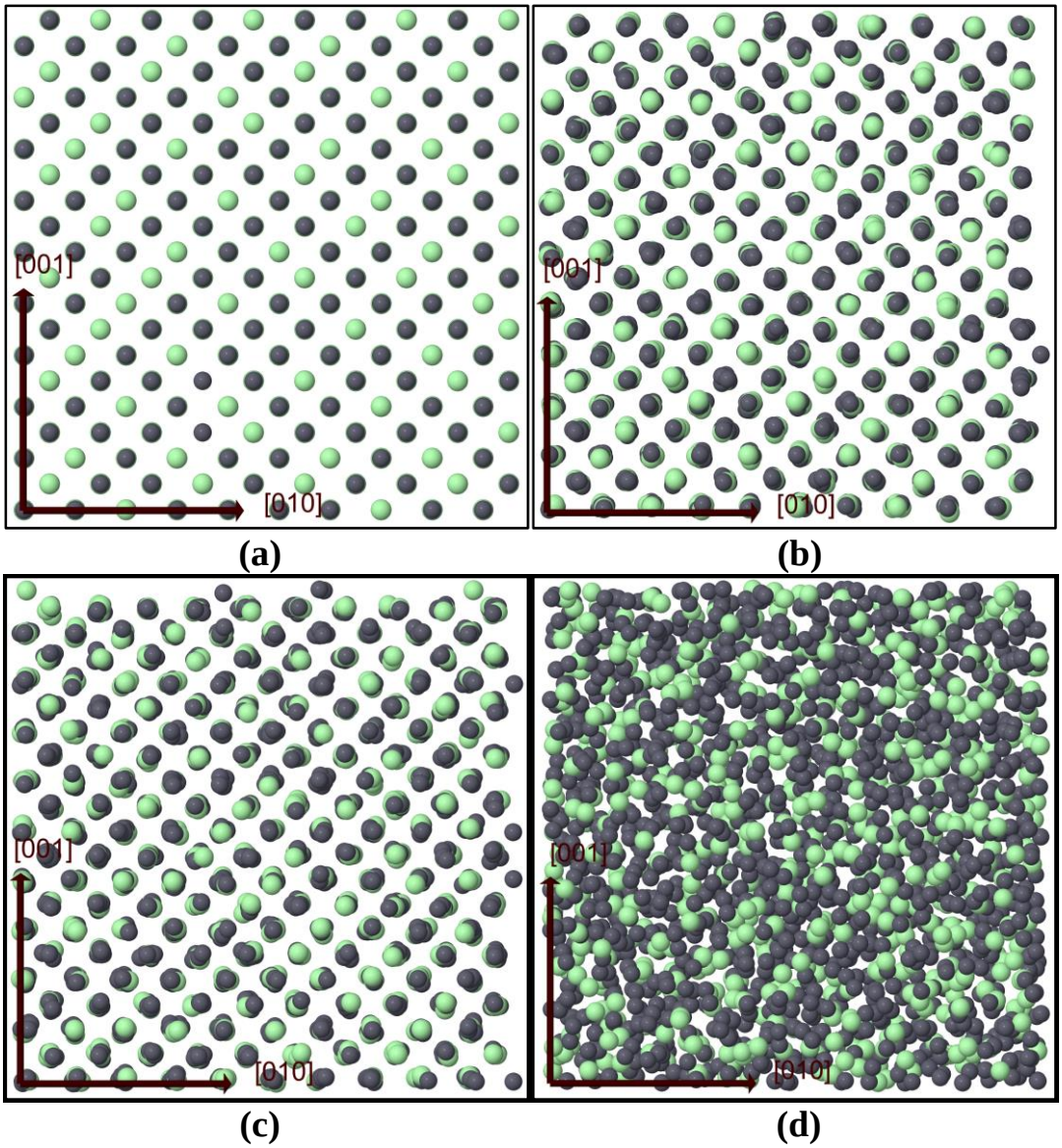

Figure 39: [100] Snapshots of equilibrium U(light-green)-70at.%Zr(dark-grey) configurations at (a) 0 K, (b) 800 K, (c) 1400 K, and (d) 2000 K. The 0 K-1400 K snapshots illustrate the ordered atomistic configurations where there is a preference for U atoms to be 3NN or 4NN, while the 2000 K snapshot illustrates the transition to melting.

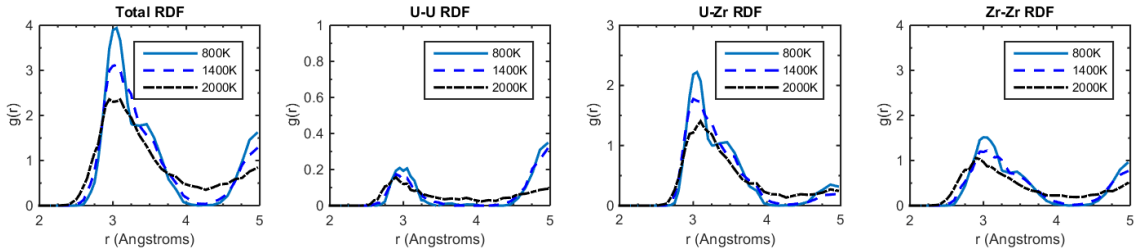

Figure 40: Full and partial RDFs of U-70at.%Zr at 800 K, 1400 K, and 2000 K.

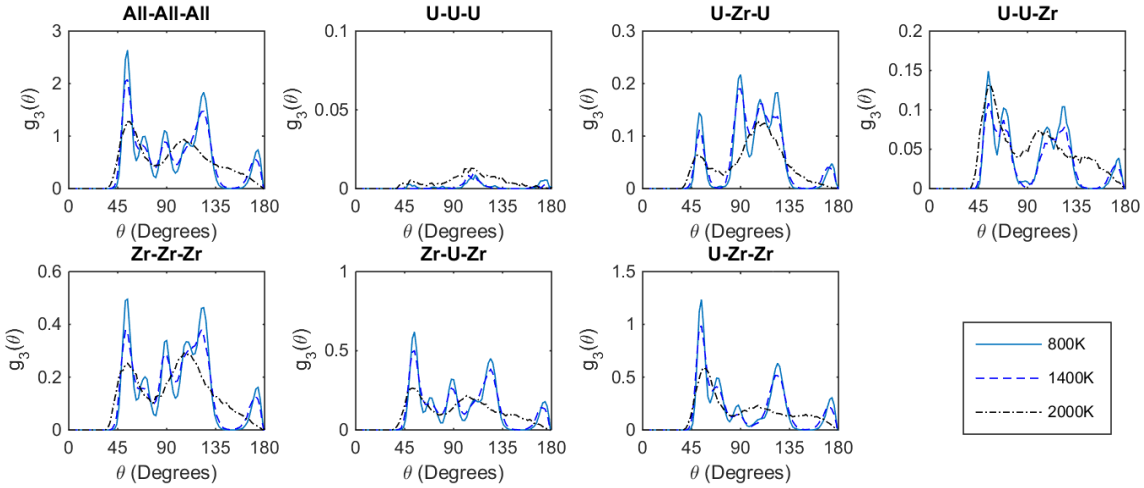

Figure 41: Full and partial BADFs of U-70at.%Zr at 800 K, 1400 K, and 2000 K.

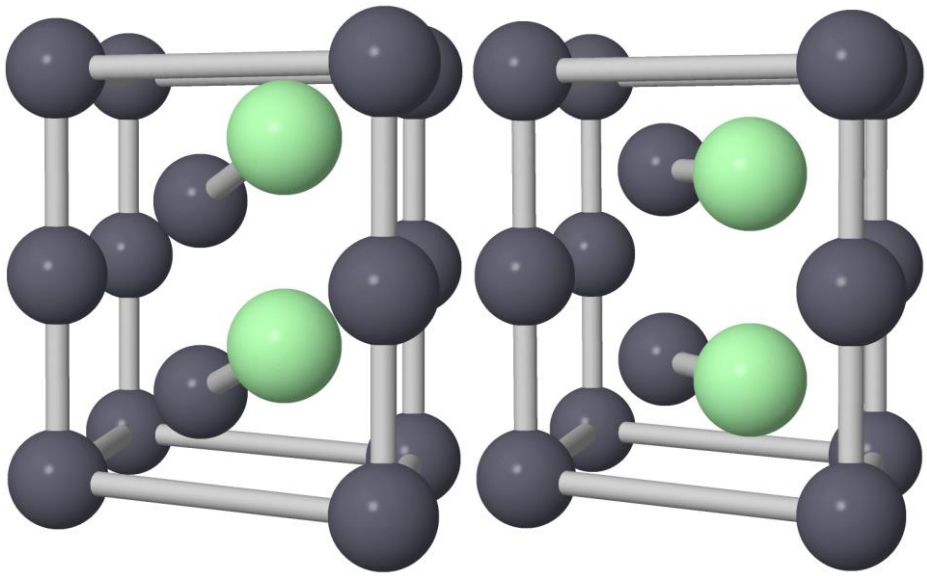

Figure 42: Snapshot of the (a) $P\bar{3}m1$ space group equivalent to a reoriented bcc structure with the U atoms (light-green) to (b) the P6/mmm space group of a partially ordered δ-UZr_2 phase.

Zirconium-Rich Compositions

The atomistic configurations of the Zr-rich U-Zr alloys (Figure 43) show the precipitation of more band-like behavior from 0 K-2000 K, while Figure 44 and Figure 45 show the complimentary RDFs and BADFs respectively. The U-90at.%Zr alloy is used to illustrate the typical Zr-rich precipitation phenomena. The band-like separation is easily viewed from the [100] direction, and consists of regions of Zr atoms and regions of U and Zr atoms in differing arrangements where the U atoms are not 1NN. The band-like structure has an average thickness of about 16 Å at 800 K which becomes less defined as temperature increases, resulting in a chaotic band-like structure at 2300 K. The preference of U atoms to not be 1NN can also be seen in the U-U g(r) (Figure 44) and the U-U-U, U-U-Zr, U-Zr-U, and Zr-Zr-Zr $g_3(\theta)$ (Figure 45). The U-U-U and the U-U-Zr $g_3(\theta)$ BADFs' lack of bond angles and the U-U g(r) figure's lack of radial information indicates that there are very few U-U 1NN or 2NN. However, from the U-Zr-U $g_3(\theta)$ figure, it can be seen that the U-Zr-U configuration has a tendency to line up in a single 1NN and a single 2NN direction from the 109º and 122º peaks. The U-Zr-U $g_3(\theta)$ figure and the atomistic configurations indicate that U atoms prefer to be 3NN and 4NN. As explained in the Intermediate section above, the U atoms' preference to not be 1NN, but instead 3NN or 4NN, makes for an easier transition to the partially ordered δ-UZr_2 phase. The band-like precipitation behavior shows the thermodynamic driving force to the acicular, Widmanstätten, and martensitic needle microstructures observed experimentally [46, 47] and shown in Figure 2e.

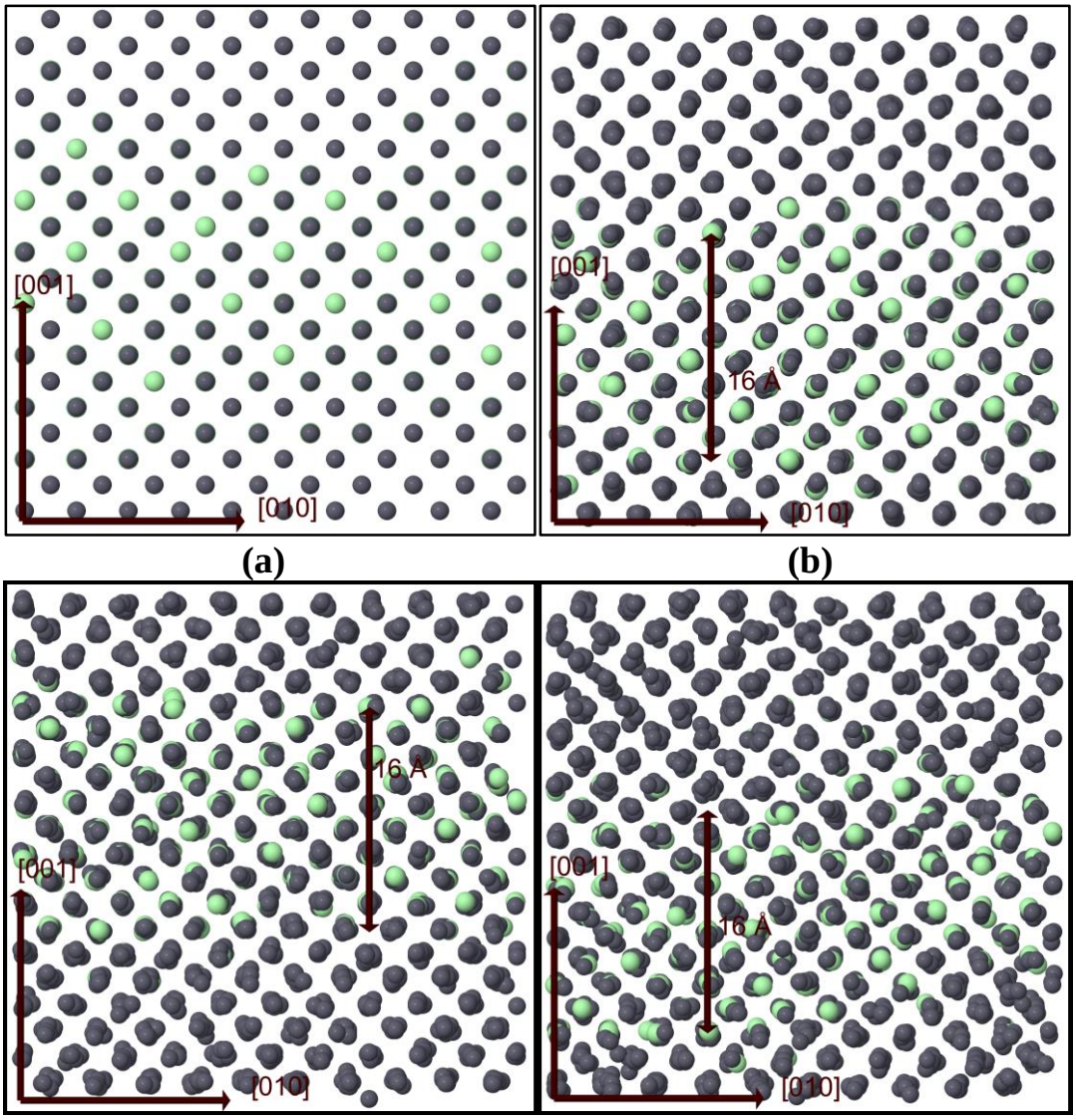

Figure 43: [100] Snapshots of equilibrium U(light-green)-90at.%Zr(dark-grey) configurations at (a) 0 K, (b) 800 K, (c) 1400 K, and (d) 2000 K. The snapshots illustrate the band-like separation behavior of the regions where U atoms prefer to be 3NN or 4NN from the regions of pure Zr.

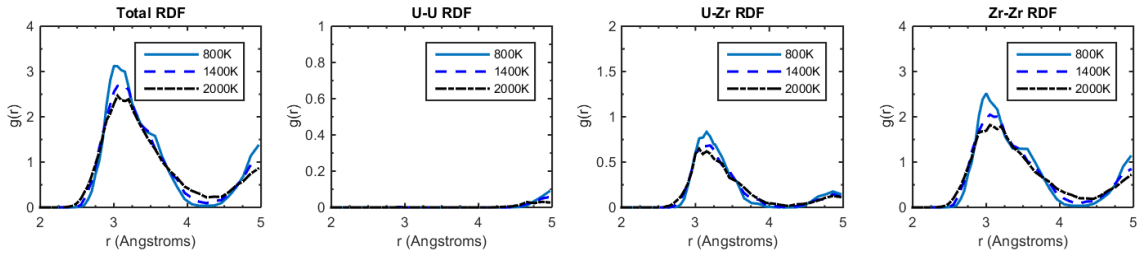

Figure 44: Full and partial RDFs of U-90at.%Zr at 800 K, 1400 K, and 2000 K.

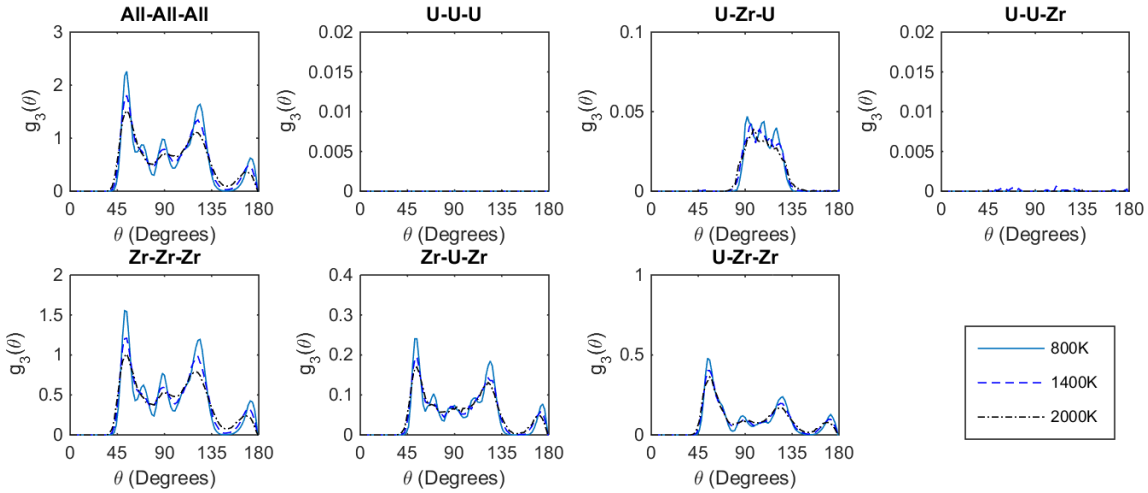

Figure 45: Full and partial BADFs of U-90at.%Zr at 800 K, 1400 K, and 2000 K.

CHAPTER 13

MEAM SENSITIVITY AND UNCERTAINTY ANALYSIS FOR THE U-ZR SYSTEM

Interatomic potentials have become a useful tool in modeling atomic forces for various materials. Interatomic potentials have advanced from generic radial distances of Lennard Jones potentials, to multi-body potentials (EAM, extended Finnis-Sinclair, airebo), and more recently to include angular bonding effects (MEAM, COMB, AMEAM, MS-MEAM, Tersoff, and other Angular-Dependent Potentials (ADP)). The increase in the complexities of these potentials allows more materials to be better simulated and understood. However, with the increase in complexities, the cause/effect relationship of potential parameters to material properties can become blurred and is poorly understood. Therefore, this research performs a sensitivity analysis on the parameters of a few MEAM potentials in the hope of better understanding the sensitivity of more complex interatomic potentials.

The sensitivity of the MEAM potential on the ground state and thermal properties is thoroughly examined. The MEAM potential is a very commonly used interatomic potential whose format allows the research to extend somewhat to EAM, AMEAM, MS-MEAM, and other ADPs. The sensitivity analysis is conducted using the uranium, zirconium, and uranium-zirconium MEAM potentials. Previous 0 K sensitivity analyses have been performed using MEAM potentials [91, 282, 283]. However, so far no thermal analysis has been conducted. Sensitivity analyses on thermal properties require much longer simulations and often multiple runs for property determination. In addition, this is the first reported sensitivity analysis for alloys, for which a new method of analyzing the effects that parameters have on the alloy

properties was developed. These sorts of sensitivity analyses are helpful in potential development and the understanding of these interatomic potentials.

Sensitivity Analysis Methodology

A sensitivity analysis was performed on the degree to which the MEAM parameters affect the ground state and thermal properties of the elemental and alloy systems. In the past, there have been a few sensitivity analyses of the MEAM potential performed on ground state properties [91, 283, 284], but this is the first reported sensitivity analysis of the MEAM potential performed on the thermal properties, which tend to be more complex and somewhat chaotic due to their nonindependent spatial parameters. The thermal motion combined with the complexity of the angular partial electron densities and the screening parameters does not allow for a directly quantitative sensitivity analysis. Therefore, a semi-quantitative approach was used to describe the potential significance of how a change in the MEAM parameters could affect the ground state and thermal properties of the system. The sensitivity analysis performed uses one-at-a-time (OAT) sampling [285] where one parameter changes values between consecutive simulations, after which the results are analyzed. However, the input parameters are non-independent input factors creating seemingly random fluctuations or jumps over ranges of input parameters. In addition, the range of acceptable inputs for the parameters in this case is unknown, since changes in the parameters may lead to a destabilization of the phase of interest. Therefore, the maximum parameter change examined is set to be a percentage of the initial parameter value, and after each simulation the phase stability is examined ensuring the input change did not cause phase changes.

The OAT sampling is computationally expensive, therefore, the sensitivity analysis was conducted fully on the uranium potential, after which a more detailed analysis was conducted on the parameters determined to be significant with both the U and Zr potential.

Sensitivity Analysis of the Elemental Ground State Properties

We begin by examining the ground state sensitivity analysis and comparing it to those previously published. The bcc phase elastic constants and bulk modulus are calculated, as well as the relative phase stability in terms of change in energy. The properties were calculated using the same methodology as described in Chapter 5.

Table 12: bcc MEAM Sensitivity Table: Effect of uranium elemental parameters on elastic constants, bulk modulus, and relative phase energies.

MEAM Parameters (15% change)													
Properties	A	B^0	B^1	B^2	B^3	t^1	t^2	t^3	C_{min}	C_{max}	δ	α	E_C
bcc C_{11} and C_{12}	+	-	/	-	/	/	-	/	-	-	+	+	+
(+>Δ2GPa)	↓	↑	/	↑	/	/	↑	/	↑	↑	↓	↑	↑
bcc C_{44}	+	+	/	+	/	/	+	/	-	-	-	+	+
(+>Δ2GPa)	↓	↓	/	↑	/	/	↑	/	↑	↑	↓	↑	↑
bcc Bulk Modulus	+	+	/	/	/	/	/	/	-	-	-	+	+
(+>Δ2GPa)	↓	↑	/	/	/	/	/	/	↓	↑	↓	↑	↑
ΔE bcc → fcc	+	+	/	/	/	/	/	/	-	-	-	+	/
(+>Δ0.01eV/atom)	↓	↑	/	/	/	/	/	/	↑	↓	↑	↓	/
ΔE bcc → hcp	+	+	/	-	-	/	-	-	-	-	-	+	/
(+>Δ0.01eV/atom)	↓	↑	/	↑	↓	/	↑	↑	↑	↓	↑	↓	/

In Table 12 above, the "+" sign means that the effect of a 15% parameter change was significant, while a "-" sign means the change was less significant, and the "/" symbol means there was either no effect or almost no effect. The effects of the parameter changes on the bcc elastic constants and bulk modulus (C_{11}, C_{12}, C_{44}, and B) were deemed to be significant if the

resulting change was greater than 2 GPa, and the change in energy between phases was deemed to be significant if they resulted in an energy change greater than 0.01eV/atom.

In addition to the significance of the parameter change on the ground state properties, the directionality of the relationship is also noted for the 15% parameter variations. In the table above, a "↑" designated a directional relationship where an increase in the MEAM parameter resulted in an increase in the thermal property; a "↓" designated an indirect relationship where an increase in the MEAM parameter resulted in a decrease in the thermal property; and a "↕" designated a mixed relationship.

The ground state sensitivity analysis matches up fairly well with those of Lee et al. [284] for the bcc elastic constants and Kim et al. [91] for the change in energy between the phases. However, this time a directionality was applied as well as the significance. The analysis performed on other crystal phase elastic constants shows different trends indicating the ground state properties of different phases are often dependent on different parameters [91, 283].

Lee et al. [284] performed a sensitivity analysis on the ground state properties for bcc elements. In this publication it was found that the A, B^0, and C_{min} parameters all had a significant impact on the elastic constants and the relative phase energies, yet the significance was never quantified in terns if degree of change or its direction. Similarly, we found that the A, B^0, and C_{min}, as well as others, had an impact on the properties and attribute some of the difference in less versus more significant to the cut-off used as well as the potential. While Kim et al. [91] performed her sensitivity analyses on the hcp ground state phase, she also included the change in the energy between phases in her analysis. In that publication the A, B^0, and t^3 parameters were found to cause significant changes in the energy difference between the hcp and

bcc phases. Once again we find that our results are consistent with those of Kim et al. [91], where the same parameters were found to cause a change in the relative energies between the bcc and hcp phases.

Sensitivity Analysis of the Elemental Thermal Properties

The heat capacity was calculated by the average change in the enthalpy over the change in temperature between 1000 K-1400 K for bcc uranium and 1600 K-2100 K for bcc zirconium. The thermal expansion reported is the average instantaneous thermal expansion coefficient between 1000 K-1400 K for bcc uranium and 1600 K-2100 K for bcc zirconium. However, the lattice constant was calculated by taking the average unit cell size at 1273 K. Lastly, the melting temperature of the potential was determined within 25 K increments using the interface method described by Moore et al. [50]. The properties were calculated using the same methodology as described in Chapter 6.

The OAT sampling was performed for the table below by implementing a 15% change, both in the positive and negative direction, in each MEAM parameter on the uranium potential. Then the system was analyzed on the significance of how the change in the MEAM parameter affected the specific heat, the melting temperature, and the thermal expansion of the system.

Table 13: bcc MEAM Sensitivity Table: Effect of uranium elemental parameters on elemental thermal properties.

Elemental Properties	MEAM Parameters (15% change)												
Heat Capacity	A	B^0	B^1	B^2	B^3	t^1	t^2	t^3	C_{min}	C_{max}	δ	α	E_C
(+≥1 J/mol-K)	+	-/+	-	-	-	-	-	-	-/+	-	-	-/+	+
(-<1 J/mol-K)	↑	↑	↑	↓	↓	↑	↓	↓	↕	↑	↓	↑	↓
	L		L	L			L				L		
T_{melt}	A	B^0	B^1	B^2	B^3	t^1	t^2	t^3	C_{min}	C_{max}	δ	α	E_C
(+≥100K)	+	+	+	+	-	-/+	-/+	-/+	+	+	-/+	+	+
(-<100K)	↓	↓	↕	↑	↑	↕	↑	↑	↑	↑	↓	↑	↑
Thermal Expansion	A	B^0	B^1	B^2	B^3	t^1	t^2	t^3	C_{min}	C_{max}	δ	α	E_C
(+≥0.0004%)	+	+	+	-	-	-	+	-	+	+	+	+	+
(-<0.0004%)	↑	↓	↑	↓	↕	↕	↓	↕	↓	↓	↑	↑	↓
	L		L				L			L	L		
Lattice Constant	A	B^0	B^1	B^2	B^3	t^1	t^2	t^3	C_{min}	C_{max}	δ	α	E_C
(+≥0.1Å)	+	+	-	-	-	-	-	-	+	+	+	+	+
(-<0.1Å)	↑	↑	↑	↑	↑	↓	↓	↕	↓	↓	↑	↓	↓
	L			L		L	L		L	L	L	L	L

In

Table 13 above, the "+" designates that the 15% change in the MEAM parameter caused a significant change in the thermal property; the "–" designates that the change was less significant; and the "-/+" designates that the change in the MEAM parameter had a significantly varying effect on the thermal property from less significant to greatly significant. A change in

the elemental specific heat capacity was considered to be significant if greater than 1 J/mol-K; a change in the melting temperature was considered significant if greater than 100 K; a change in the thermal expansion was considered to be significant if greater than 0.0004%; and a change in the lattice constant was considered significant if greater than 0.1 Å.

In addition to the significance of the parameter change on the thermal properties, the directionality of the relationship is also noted for the 15% parameter variations. In

Table 13 above, a "↑" designated a directional relationship where an increase in the MEAM parameter resulted in an increase in the thermal property; a "↓" designated an indirect relationship where an increase in the MEAM parameter resulted in a decrease in the thermal property; and a "↕" designated a mixed relationship. The "L" in the table indicates whether or not the 15% parameter variations resulted in a linear change in the property of interest. The trend was determined to be linear if $R^2 > 0.90$ for the linear fit to three data points: the initial value, the 15% increased value, and the 15% decreased value. It should be noted that the melting point was determined between a range of values, making the determination of linearity of the melting point not feasible.

Since this table was constructed based on the bcc uranium and zirconium systems, it may give an expanded view of the sensitivity analysis of other bcc systems. However, due to the symmetry and complexities of the MEAM potential, it may not be applicable to other crystal structures.

The data in

Table 13 show that while there are a few parameters that affect the elemental specific heat, they tend to be fitted based on the ground state properties and greatly affect both the thermal and ground state properties of the system. Therefore, the fitting of the elemental specific heat is not performed with the MEAM potentials, but normally falls into place after the other parameter fitting has been conducted. It should be noted that the cohesive energy parameter E_C had the greatest impact on the specific heat capacity. Some of the 15% parameter changes in B^0 and α caused obvious destabilizations in the bcc phase and could not be considered.

The elemental melting temperature is affected by a great number of MEAM parameters, including cohesive energy, bulk modulus, the embedding function parameter A, the screening parameters, and the partial electron density parameters. However, the partial electron density parameters tended to have a wildly varying significance on the melting temperature.

The thermal expansion of the system was affected by the base parameters fitted from the ground state properties, as well as from some of the partial electron density parameters and the reference state parameter δ, which is often used to fit the thermal expansion values.

To give a better view of how a few of the parameters influence the thermal properties, the parameter and its effect on the specific thermal property were plotted in the following figures. Each parameter was varied by ± 5%, ±15%, and ±25% of its initial value, giving seven data points. However, some of the parameter changes caused phase destabilization and therefore

were not reported. Occasionally additional data points were added to give a better view of how the properties changed with the parameters.

Parameter sensitivity analysis can be categorized into parameters that significantly change local environment interactions like B's and C_{min} and C_{max}, in contrast to the parameters that just scale current interactions, e.g., A. The distance parameters often cause more varied results due to the fact that changing a parameter affects how much the surrounding atoms contribute to the potential, as described below.

Bcc metals modeled with the MEAM potential tend to have a t^3 parameter that is either very small or more likely negative, a t^2 parameter that is positive, and a t^1 parameter that is positive. These partial electron weighting parameters are important for the stability and structure of the MEAM potential. It has been observed that the t^3 parameter can particularly destabilize the bcc phase if increased too much. This destabilization effect can be seen in the lowering of the melting temperature with the increasing t^3 value. Similarly, a larger B^3 value causes the partial electron density to decay more quickly and therefore leads to an increase in melting temperature and at the same time a decrease in the thermal expansion and heat capacity values. This opposite behavior is a common trend for the thermal properties. Elemental parameters that affect the thermal expansion and heat capacity normally oppositely affect the melting temperature.

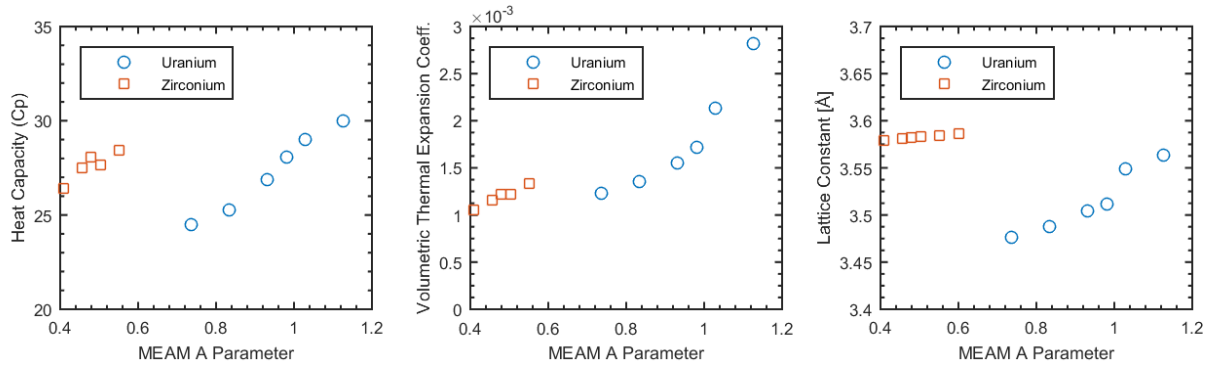

(a) (b) (c)

Figure 46: Sensitivity analysis of U's and Zr's MEAM parameter A on (a) Cp, (b) volumetric thermal expansion, and (c) lattice constant.

Figure 46 is an example of a sensitivity analysis of elemental parameter A, and its effect on some thermal properties. The parameter A is a constant multiplier to the embedding function, making it an important parameter to fit, but also one of the more simplistic ones when it comes to the thermal properties, as it does not have a direct distance relationship with the potential. The parameter and its effect on the heat capacity, thermal expansion and lattice constant can be seen in the graphs. It can be seen that an increase in the parameter A causes each of these properties to increase, often according to a mostly linear relationship.

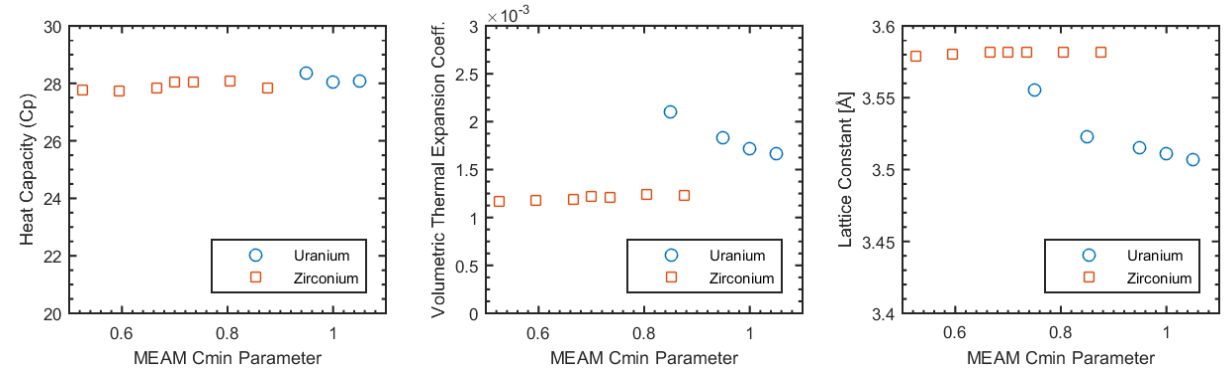

(a) (b) (c)

Figure 47: Sensitivity analysis of U's and Zr's MEAM parameter C_{min} on (a) Cp, (b) volumetric thermal expansion, and (c) lattice constant.

Figure 47 is an example of a sensitivity analysis of elemental parameter C_{min}, and its effect on some thermal properties. The parameter C_{min} is part of the bounds of the screening function, which is multiplied to the pair potential, making it a very important parameter, but it also has a very complex relationship with thermal properties. Since C_{min} is directly related to screening bounds, it directly affects how much each of the surrounding atoms contribute to the potential, making the effect on thermal properties dependent on the local environment. This is seen in the sensitivity analysis of the uranium and zirconium potentials, in that their trends do not agree with each other.

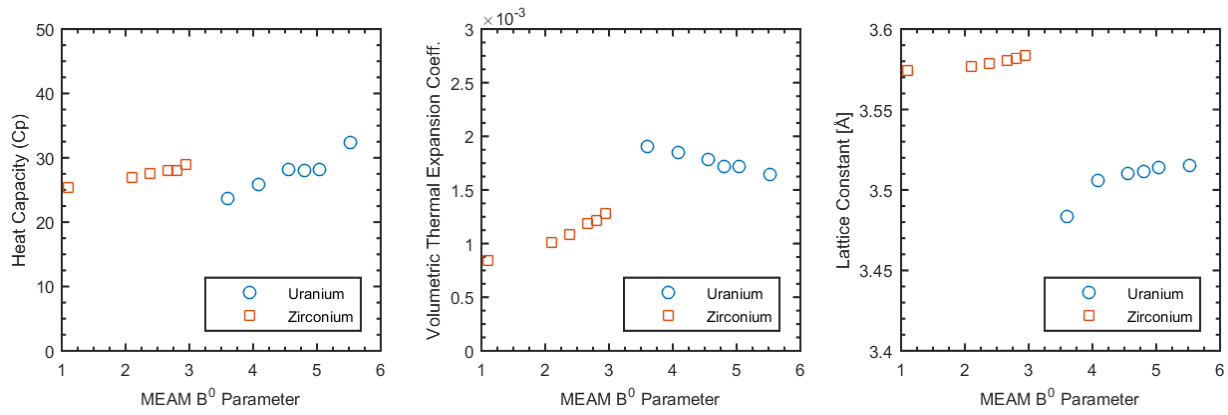

Figure 48: Sensitivity analysis of U's and Zr's MEAM parameter B^0 on (a) Cp, (b) volumetric thermal expansion, and (c) lattice constant.

Figure 48 is an example of a sensitivity analysis of elemental parameter B^0, and its effect on some thermal properties. The parameter B^0 is the distance decay function of the spherical partial electron density. Once again this parameter has a direct relationship with how much the surrounding atoms contribute to the potential, making the thermal property analysis more

complex. In addition, it is often used to fit the relative phase energies. This analysis showed that the B^0 parameter has a great effect on the bcc phase stability, since many of the parameter changes resulted in destabilizing the phase.

Sensitivity Analysis of the Elemental MEAM Parameters on Alloy Thermal Properties

Similar to the elemental thermal properties, a sensitivity analysis of the alloy's thermal properties was also performed. Once again a 15% change, both in the positive and negative direction, in each MEAM parameter was varied one at a time for the uranium potential. The system was analyzed regarding the significance of how the change in the MEAM parameter affected the alloy lattice constant versus zirconium mole fraction curve (or Vegard's law) and the enthalpy of mixing versus zirconium mole fraction curve. The properties were calculated using the same methodology as described in Chapter 8 and Chapter 9.

Previously created MEAM alloy potentials are often fitted to pure elastic constants using knowledge of the system, but guess and check methods were used with thermal properties like lattice constants and enthalpy of mixing [90-92, 97, 100, 103]. In order to solve this issue, a systematic sensitivity analysis of the alloy's structural and thermodynamic properties was conducted on the U-Zr system by examining the changes in U-20,40,60,80 at.%Zr.

Table 14: bcc MEAM Sensitivity Table: Effect of U elemental parameters on alloy thermal properties.

Properties	MEAM Parameters (15% change)												
Vegard's (+P if a≥0.35)	A	B^0	B^1	B^2	B^3	t^1	t^2	t^3	C_{min}	C_{max}	δ	α	E_C
(-P if .35>a≥.1)	+P	+P	-P	-P	-S	-P	+P	+S	-P	-P	-P	+P	+P
(+S if Σ|r_i|≥.5)	+S	+S	-S	-S		-S	+S		-S	-S	-S	-S	+S
(-S if .5>Σ|r_i|≥.1)	↕	↑	↑	↑	↓	↑	↑	↕	↑	↑	↓	↑	↓
Enthalpy of Mixing (+P if a≥0.04)	A	B^0	B^1	B^2	B^3	t^1	t^2	t^3	C_{min}	C_{max}	δ	α	E_C
(-P if .04>a≥.01)	+P	+P	/	-P	/	-P	+P	+S	-P	-S	-P	+P	+P
(+S if Σ|r_i|≥.009)	+S	+S		-S		-S	+S		-S			+S	-S
(-S if .009>Σ|r_i|≥.002)	↑	↓	↑	↓	↑	↑	↑	↑	↑	↑	↑	↓	↓

Results of the sensitivity analysis performed on the alloy's lattice parameter versus concentration (or Vegard's law) and the enthalpy of mixing for the random solid solution are provided in Table 14. Once again the "-" and the "+" symbols are used to designate that the change in the MEAM parameter causes either a less significant or more significant change to the property in question. However, this time a "P", for parabola shifted, or an "S", for shape, was added to designate how the property over concentration curve varied once the parameter had been changed. The "P", or parabola shifted, meant that the property curve could be shifted from its initial position (before the parameter change) by adding or subtracting a symmetric parabola across the mole fraction to it final position (after the parameter change). The "S", or shape shifted curve, meant that the addition or subtraction of a symmetric parabola could not entirely encompass the change in the property over concentration curve. In other words, the "S" means that the shape of the property curve had changed.

The significance of a parameter change on the enthalpy of mixing was determined using Equation (56), where the change between the initial and final curves is deconstructed into a symmetric parabola and a shape function. First the change between the initial and final curves was deconstructed by determining the constant "a" that minimized the residuals, after which the resulting residuals determined comprise the shape function.

$$\Delta H_{mix,final}(X_{Zr}) = \Delta H_{mix,initial}(X_{Zr}) + a * (1 - X_{Zr}) * X_{Zr} + S(X_{Zr}) \quad (56)$$

In Equation (56), "a" is a constant multiplier to the addition of the symmetric parabola, and $S(X_{Zr})$ is the additional change called the shape function. The degree of significance of the change was determined by the constant multiplier "a" and the shape function, $S(X_{Zr})$. The value of the constant "a" will determine if the bonding strength change is significant. After the parabola is fit, the resulting difference between the initial and final result is the shape function "S". The sum of the residuals comprising shape function "S" determine the significance of how the atoms are bonded together. The change for the enthalpy of mixing was seen as significant if the "a" constant for the parabola was greater than 0.04 or the sum of the residuals was greater than 0.009.

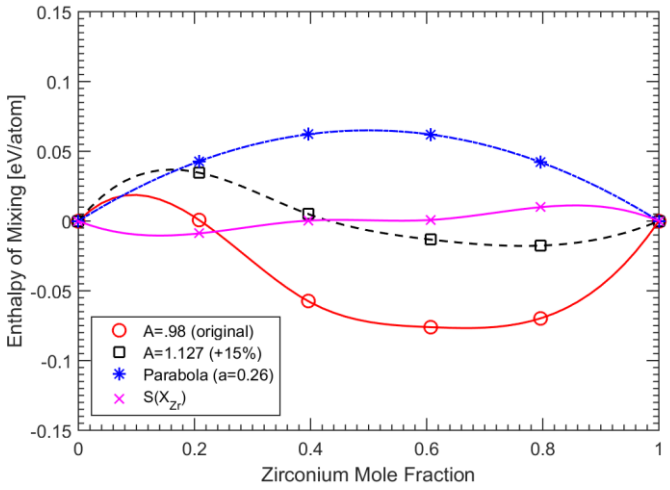

Figure 49: Visualization of the change in the enthalpy of mixing curve when U's A parameter is increased by 15% from 0.98 to 1.127, and the determination that the addition of a symmetric parabola with a=0.26 and a shape function $S(X_{Zr})$ can mimic the effect seen in the change of the enthalpy of mixing.

Figure 49 shows an example of the change in elemental parameter A for U on the alloy enthalpy of mixing curve, and how it can be deconstructed into a symmetric parabola with the constant "a" equal to 0.26 and a shape function of $S(X_{Zr})$. In this example, "a" being greater than 0.04 results in a +P relationship, and the sum of the residuals for the shape function being greater than 0.009 also results in a +S relationship.

However, for Vegard's law we had to separate the elemental thermal expansion effects from the lattice constant over concentration curve. Therefore, the lattice constant over concentration curve was first normalized between the starting point of 0 and the ending point of 1. This normalization allows for the analysis to be performed in a similar manner as the enthalpy of mixing, i.e.,

$$\omega_{bcc,inital}(X_{Zr}) = \left(\frac{a_{bcc,initial}(X_{Zr}) - a_{bcc,initial}(X_{Zr}=0)}{a_{bcc,initial}(X_{Zr}=1) - a_{bcc,initial}(X_{Zr}=0)}\right) \quad (57)$$

$$\omega_{bcc,final}(X_{Zr}) = \left(\frac{a_{bcc,final}(X_{Zr}) - a_{bcc,final}(X_{Zr}=0)}{a_{bcc,final}(X_{Zr}=1) - a_{bcc,final}(X_{Zr}=0)}\right) \quad (58)$$

$$\omega_{bcc,final}(X_{Zr}) = \omega_{bcc,initial}(X_{Zr}) + a * (1 - X_{Zr}) * X_{Zr} + S(X_{Zr}) \quad (59)$$

In Equations (56,58,59), ω was introduced as the temporary variable for the normalized lattice constant. The change for Vegard's law was seen as significant if the "a" constant for the parabola was greater than 0.35 or the sum of the residuals was greater than 0.04.

Once again a more detailed analysis was conducted on the MEAM parameters that were determined to be significant, and their effects on the alloy properties. The parameters were varied by ± 5%, ±15%, and ±25% of its initial value, starting with seven data points. However,

some of the parameter changes caused phase destabilization and therefore were not reported. All the reported properties were calculated at or around a 1100 K midpoint.

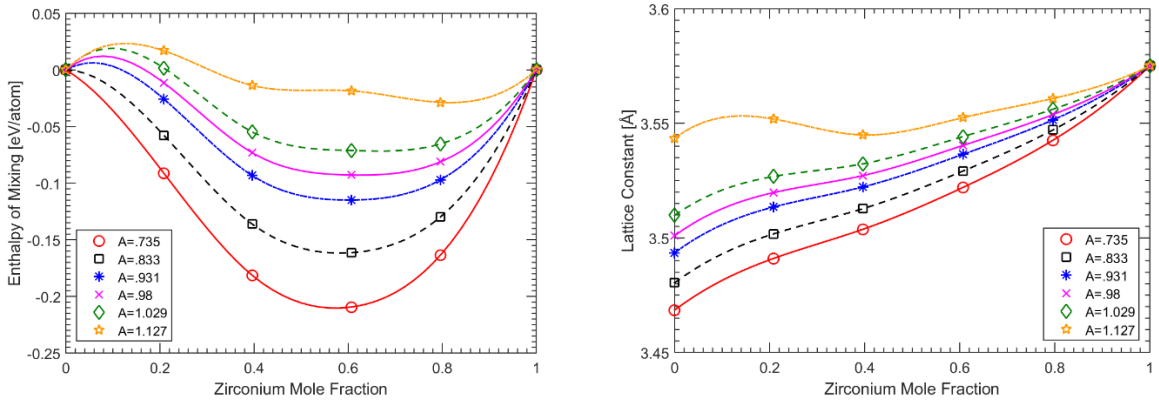

(a) (b)

Figure 50: Sensitivity analysis of U's MEAM parameter "A" on (a) enthalpy of mixing and (b) Vegard's law.

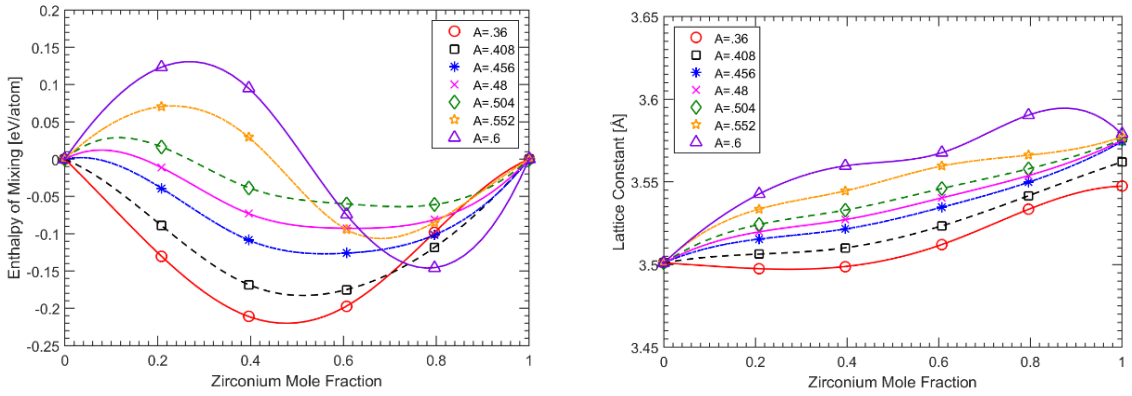

(a) (b)

Figure 51: Sensitivity analysis of Zr's MEAM parameter "A" on (a) enthalpy of mixing and (b) Vegard's law.

Figure 50 and Figure 51 show how the elemental parameter "A" affects the alloy's thermal properties. It can be seen that the change in the parameter affects the change in both the enthalpy of mixing and the Vegard's law via a symmetric parabola, as well as changes the shape

of the curve, indicating a +P and +S relationship. In addition, generally an increase in the parameter caused the curve to shift into the more positive values, indicating an overall direct (↑) relationship.

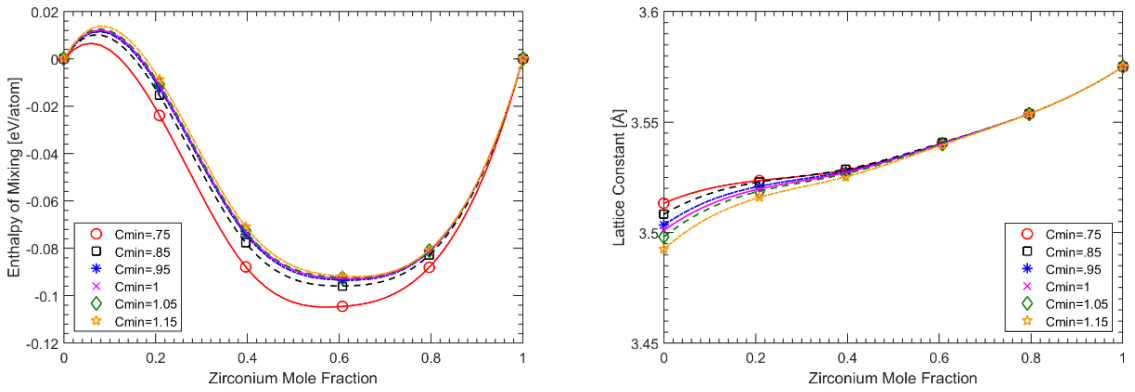

(a) (b)

Figure 52: Sensitivity analysis of U's MEAM parameter C_{min} on (a) enthalpy of mixing and (b) Vegard's law.

Figure 52 shows how the elemental parameter C_{min} of uranium affects the alloy's thermal properties. The zirconium C_{min} parameter had even less of an effect on the properties and therefore was not plotted. It can be seen that the change in the parameter minimally affects the enthalpy of mixing and the Vegard's law. However, an increase in the parameter caused the enthalpy of mixing to slightly shift upward and the Vegard's law to shift downward, indicating a direct relationship for the enthalpy of mixing and a direct relationship for Vegard's law, once the thermal expansion effects were normalized.

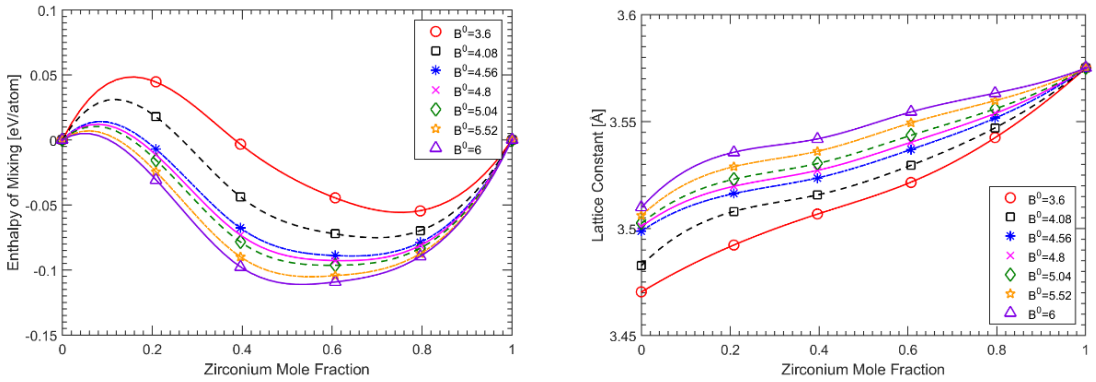

(a) (b)

Figure 53: Sensitivity analysis of U's MEAM parameter B^0 on (a) enthalpy of mixing and (b) Vegard's law.

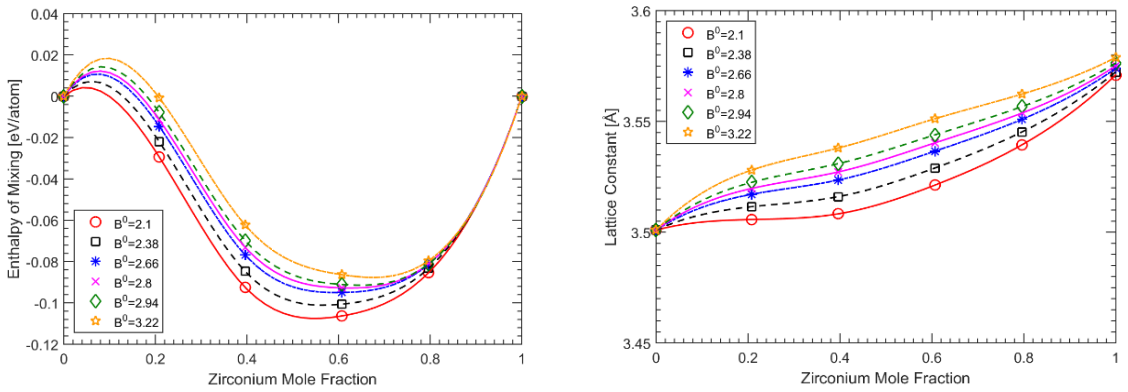

(a) (b)

Figure 54: Sensitivity analysis of Zr's MEAM parameter B^0 on (a) enthalpy of mixing and (b) Vegard's law.

Figure 53 and Figure 54 show how the elemental parameter B^0 affects the alloy's thermal properties. It can be seen that the change in the parameter affects the change in both the enthalpy of mixing and the Vegard's law via a symmetric parabola, as well as changes the shape of the curve, indicating a +P and +S relationship. In addition, generally an increase in the parameter caused the curve to shift into the more positive values, indicating an overall direct relationship.

Sensitivity Analysis of the Alloy MEAM Parameters on Alloy Thermal Properties

The effect of alloy MEAM parameters on the alloy's properties was also examined, again using a 15% change, both in the positive and negative direction, in each MEAM parameter. The system was analyzed regarding the significance of how the change in the MEAM parameter affected the alloy's lattice constant versus zirconium mole fraction curve (or Vegard's law) and the enthalpy of mixing versus zirconium mole fraction curve.

Table 15: bcc MEAM Sensitivity Table: Effect of alloy parameters on alloy thermal properties.

Properties	**MEAM Parameters (15% change)**			
Vegard's (+P if a≥0.35)	Alloy δ	Alloy α	Alloy Δ	ρ^0
(-P if .35>a≥.1)	+P	+P	+P	+P
(+S if Σ|r_i|≥.5)	-S	+S		
(-S if .5>Σ|r_i|≥.1)	↓	↓	↑	↕
Enthalpy of Mixing (+P if a≥0.04)	Alloy δ	Alloy α	Alloy Δ	ρ^0
(-P if .04>a≥.01)	+P	+P	+P	+P
(+S if Σ|r_i|≥.009)	-S	-S	-S	+S
(-S if .009>Σ|r_i|≥.002)	↓	↑	↑	↕

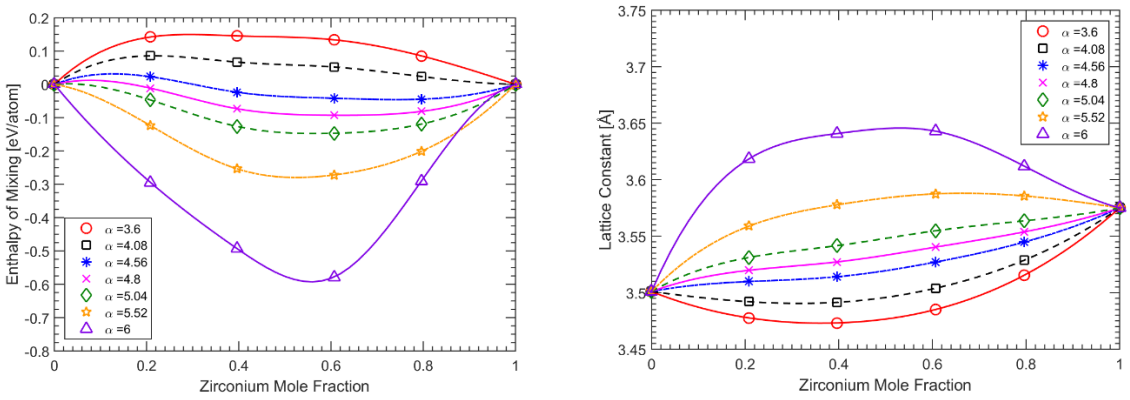

(a) (b)

Figure 55: Sensitivity analysis of U-Zr alloy MEAM parameter α on (a) enthalpy of mixing and (b) Vegard's law.

Figure 55 shows how the alloy parameter α affects the alloy's thermal properties. It can be seen that the change in the parameter affects the change in both the enthalpy of mixing and

the Vegard's law mostly via a symmetric parabola, and only slightly changes the shape of the curve, indicating a +P and -S relationship. This parameter shows great potential for calculated MEAM alloy property adjustment using a symmetric parabola only.

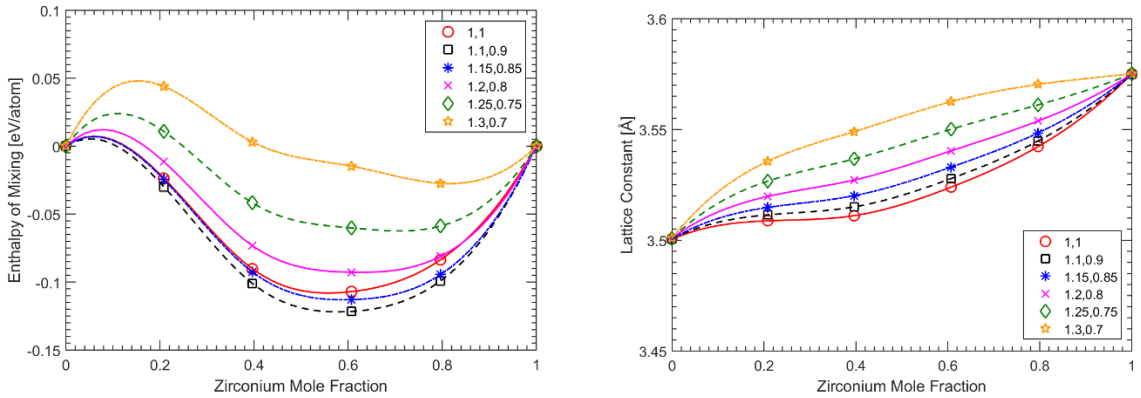

(a) (b)

Figure 56: Sensitivity analysis of U-Zr alloy MEAM parameters ρ_U,ρ_{Zr} on (a) enthalpy of mixing and (b) Vegard's law.

Figure 56 shows how the parameters ρ_U,ρ_{Zr} affect the alloy's thermal properties. These parameters are often used to fit the alloy properties. It can be seen that the change in the parameter affects the change in both the enthalpy of mixing and the Vegard's law mostly via a symmetric parabola, and only slightly changes the shape of the curve, indicating a +P and -S relationship.

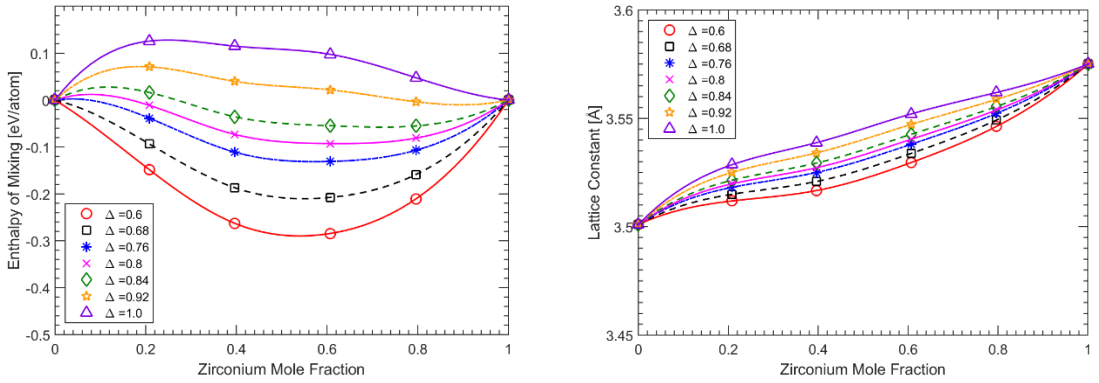

(a) (b)

Figure 57: Sensitivity analysis of U-Zr alloy MEAM parameter Δ on (a) enthalpy of mixing and (b) Vegard's law.

Figure 57 shows how the alloy parameter Δ affects the alloy's thermal properties. It can be seen that the change in the parameter affects the change in both the enthalpy of mixing and the Vegard's law mostly via a symmetric parabola, and only slightly changes the shape of the curve, indicating a +P and -S relationship. This parameter shows great potential for calculated MEAM alloy property adjustment using only a symmetric parabola.

CHAPTER 14

SUMMARY and CONCLUSIONS

A MEAM potential focused on the high temperature γ-U-Zr solid solution alloy was developed, which is virtually inaccessible to first principles calculations. In addition, the U-Zr potential developed was able to closely mimic the experimental thermodynamics, e.g., the enthalpy of mixing at temperature, which has evaded multiple ground state first principles simulations.

The validity and transferability of the high temperature U-Zr MEAM potential was tested against numerous first principles and experimental properties. The simulation results concur with the experimental or first principles elastic constants, lattice parameters, thermal expansion, defect formation energies, enthalpy of fusion, and melting temperatures, while the heat capacity tends to be a little undervalued for both U and Zr until the conduction electronic heat capacity contributions were added, resulting in values between the experimental results.

The potential resulted in a $5.41*10^{-5}$ volumetric thermal expansion coefficient for γ-U, which is 3.4% off the $5.61*10^{-5}$ experimental value [251], and a $3.27*10^{-5}$ volumetric thermal expansion coefficient for β-Zr, which is 10.7% off the $2.92*10^{-5}$ experimental value [258]. The U potential resulted in a melting temperature between 1325 K-1350 K, which is around 60 K off the experimental 1408 K; an enthalpy of fusion of 8.519 J/mol-K that matches the more recent experimental result of 8.518 J/mol-K [189]; and a 2.66 volume percent change upon melting that is 20.9% off the 2.2% experimental value [180]. The Zr potential resulted in a melting

temperature between 2150 K-2175 K, which is around 25 K off the experimental 2125 K; an enthalpy of fusion of 14.844 J/mol-K that is in agreement with most of the experimental values [181, 193-195, 198]; and a 3.06 volume percent change upon melting which is 21.5% off the 3.9% experimental value [181].

Next, a comparison of γ-U and liquid-U structures is conducted and compared to previously published QMD and EAM results. The QMD and MEAM results show similar behaviors for both the bcc and liquid phases. The liquid-U phase was found to have a characterizable structure of a local network of tetrahedrals.

The potential was also able to replicate trends and values seen in the alloy's thermodynamic properties. It was able to replicate Vegard's law for the lattice constants (with an almost perfectly linear fit) and the experimental thermal expansion for the U-Zr alloy, and it is the first to match the experimental enthalpy of mixing for the γ-U-Zr phase at temperature. In addition, the heat capacity trend versus zirconium mole fraction mimics the experimental trend seen in the laser-flash method used by Takahashi et al. [261].

The newly created MEAM potential was used to explore new thermodynamic properties for the γ-U-Zr phase, e.g., constant volume heat capacity, the isothermal compressibility, adiabatic index, and the Grüneisen parameters. Where alloy experimental data is available, the model appears to agree quite well.

Then atomistic simulations of the thermodynamic ordering in a mixture are shown to be able to mimic and contribute to the deeper understanding of precipitation morphology and microstructure evolution in U-Zr alloys. The MEAM potential was used to investigate the

preferential ordering behavior of U-Zr alloys to relate the ordering behavior to observed microstructures.

Atomistic simulations of the U-rich alloys show a tendency towards separation resulting in precipitates whose shape depends on temperature. At lower temperatures the precipitates tend to form in more faceted and spherical arrangements, while at higher temperatures precipitates form in more of a band-like structure. Previous experimental research has shown this precipitate behavior change from spherical to lamellar microstructure as temperature increased, but until now this transition was not well understood.

Intermediate alloys, around the δ-UZr_2 phase concentration, show a preference to ordering where the U atoms are not 1NN, but 3NN or 4NN. This kind of ordering behavior allows for a more direct transition to the partially ordered δ-UZr_2 phase seen experimentally. Lastly, simulations of the Zr-rich alloys show a mix of ordering and separation behaviors.

The Zr-rich systems show ordered sections where U atoms are 3NN or 4NN, allowing more of a direct transformation to the partially ordered δ-UZr_2 phase, separated by bands from the regions of pure Zr. These bands mimic the acicular, Widmanstätten, and martensitic needle microstructures seen in the previous experimental research. These simulations are able to successfully replicate some of the fundamental thermo-physical and microstructural characteristics following fabrication and irradiation of the U-Zr metallic fuels.

A sensitivity analysis was conducted using OAT sampling of the MEAM interatomic potential parameters and how changes in parameters propagate throughout the system, causing changes to numerous structural and thermodynamic properties. This analysis is key to unravelling the cause/effect relationship of interatomic potentials, as well as discovering their

benefits and drawbacks. This sensitivity analysis shows how physical properties can be fitted when using interatomic potentials, as well as the properties which cannot be adjusted. This research gives insight into the overall transferability and uncertainty when fitting and using interatomic potentials such as the MEAM.

The analysis begins on the thirteen elemental MEAM parameters and how they affect the bcc ground state elastic constants and relative phase energies. The sensitivity analysis performed is shown to agree well with previously published results. However, our analysis takes the sensitivity of the ground state properties a bit further by including more parameters that were varied, adding a quantitative indication of the significance of a change, and adding the directionality of the parameter effects on the observed properties.

Next, the effect the elemental parameters had on the thermal properties was examined. The trends in which MEAM parameters affect the thermal properties of the bcc metal have been successfully analyzed and categorized. The thermal properties examined include heat capacity, melting point temperature, thermal expansion, and lattice constant. The melting point, lattice constant, and thermal expansion all seem to be moderately dependent on a number of MEAM parameters. However, the heat capacity was shown to have little variance with many of the properties and could not be easily adjusted. The parameters that had much of any significance on the values Ec and A are usually fit to ground state properties of cohesive energy and relative phase stability.

Then the effect the elemental parameters had on alloys was examined. The alloy properties examined were the Vegard's law for lattice constants and the enthalpy of mixing. The sensitivity analysis of alloy properties has never been previously published, and therefore a

method of deconstructing the effects was developed. The method developed allowed the change to be broken up by the magnitude that the strength or length of bonding between the atoms changed and how the elements were being bonded together changed. From this analysis it was determined that before alloy parameters are fit, it is important that the elemental parameters be fit well first, as many of the alloy properties can change significantly with changes to the elemental parameters.

Finally, the effect the alloy parameters had on the alloy properties was examined. The alloy properties examined include Vegard's law for lattice constants and the enthalpy of mixing. The analysis showed that a few key parameters exist that allow for shifts in either the Vegard's law curve or enthalpy of mixing curve, like the alloy Δ and α parameters, making the fitting of most alloy thermodynamics relatively simple.

Metallic fuel in fast reactors can undergo compositional variation changes and large irradiation swelling and growth due to irradiation damage, and the MEAM potential allows the study of each of these phenomena. In this study, we focus on the structure, thermodynamics, and the compositional variation, resulting in different morphologies, following fabrication of the U-Zr metallic fuel. This compositional variation can also occur during reactor operation, leading to additional complexities that need to be accounted for, and can be studied using the MEAM potential and atomistic methods developed.

The MEAM potential enables atomistic results to be compared to experimental results, allowing the atomistic mechanisms contributing to the experimental results to be witnessed and understood for the first time. The atomistic study allowed the heat capacity of U and Zr to be broken up into the lattice, anharmonic, and expansion effects versus the contributions of the

conduction electrons. It also obtained new values for the enthalpy of fusion and percent volume change upon melting, which are important for fuel transient codes. The calculated thermal expansion, heat capacity, isothermal compressibility, and Grüneisen parameter allow the knowledge gained from atomistic simulations to be directly tied to macroscopic properties. The heat capacity, thermal expansion, and isothermal compressibility can all be used in continuum models for a more complete fuel modelling code. The Grüneisen parameter is important for equations of state (EOS), as well as understanding and modelling transients, as it often shows up in equations that describe the thermoelastic properties of materials at high pressures and temperatures [286].

The study of the U-Zr morphological evolution not only provides a new methodology for using atomistics to understand microstructure, but also supplies valuable information on the thermodynamic driving mechanisms for U-Zr alloys, which is important for both fabrication and behavior during reactor operation. If the U-Zr fuel has sections that are more uranium-rich than others, this changes the neutronics of the fuel due to its non-homogeneous nature. Failing to take into account non-homogeneity could result in the underestimation of a reactor's reactivity and criticality. The fabrication of the U-Zr fuel pellets can also benefit from this research, by modifying the fuel production process and annealing temperatures in order to obtain a desired U-Zr morphology.

In addition, the creation of this potential provides a tool for further atomistic research of the U-Zr alloy through the study of the larger scale atomistic simulations of defect properties, radiation damage, void/bubble energetics, coalescence, and plasticity. In addition, the MEAM potential can be expanded to include fission products, cladding, and other minor actinides,

permitting the study of ternary metallic fuel, fuel-cladding interactions, and how fission products can affect fuel properties.

APPENDIX A: Common Thermodynamic Equations

$$G(T,x) = H(T,x) - T * S(T,x) \tag{A1}$$

$$H(T,x) = E(T,x) + P(T,x)V(T,x) \tag{A2}$$

$$H(T,x) = G(T,x) - T\left[\frac{\partial G(T,x)}{\partial T}\right]_P \tag{A3}$$

$$\frac{G(T,x)}{T} = \frac{G^{ref}\left(T^{ref},x\right)}{T^{ref}} - \int_{T^{ref}}^{T} \frac{H(T',x)}{T'^2} dT' \tag{A4}$$

$$S(T,x) = -\left[\frac{\partial G(T,x)}{\partial T}\right]_P \tag{A5}$$

$$\alpha_V(T,x) = \frac{1}{V}\left[\frac{\partial V(T,x)}{\partial T}\right]_{P,x} \tag{A6}$$

Heat Capacity Equations:

$$C_p(T,x) = -T\left[\frac{\partial^2 G(T,x)}{\partial T^2}\right]_{P,x} = \left[\frac{\partial H(T,x)}{\partial T}\right]_{P,x} \tag{A7}$$

$$C_V = \left(\frac{\partial E}{\partial T}\right)_V \tag{C8}$$

$$C_p - C_V = T\left(\frac{\partial P}{\partial T}\right)_{V,N}\left(\frac{\partial V}{\partial T}\right)_{P,N} = VT\frac{\alpha^2}{\beta_T} \tag{A9}$$

Partition Function:

$$P_{i,NPT} = \frac{e^{-\beta(E-pV_i)}}{Z_{NPT}} \tag{A10}$$

$$Z_{NPT} = \sum_i e^{-\beta pV_i} Z_{NVT} \quad Z_{NVT} = \sum_i e^{-\beta E_i(N,V)} \tag{A11}$$

Gibbs-Duhem Equations:

$$dG = \sum_{i=1}^{I} \mu_i dN_i + \sum_{i=1}^{I} N_i d\mu_i = Vdp - SdT + \sum_{i=1}^{I} \mu_i dN_i \tag{A12}$$

At constant pressure and temperature, equation becomes:

$$0 = N_1 d\mu_1 + N_2 d\mu_2 \tag{A13}$$

$$x_1 \left.\frac{\partial \ln \gamma_1}{\partial x_1}\right|_{p,T} = x_2 \left.\frac{\partial \ln \gamma_2}{\partial x_2}\right|_{p,T} \tag{A14}$$

APPENDIX B: Notations and Symbols

Basic Notations

E: Internal Energy

ΔE: Change in Energy

U: Potential Energy

V: Volume

P: Pressure

H: Enthalpy

G: Gibbs Energy

S: Entropy

T: Temperature

N: Moles

R: Gas Constant

k_B: Boltzmann's Constant

X: Composition

N_A: Avogadro's Number

1NN: 1st Nearest Neighbor

2NN: 2nd Nearest Neighbor

3NN: 3rd Nearest Neighbor

4NN: 4th Nearest Neighbor

MS: Molecular Statics

MD: Molecular Dynamics

MC: Monte Carlo

DFT: Density Functional Theory

DOS: Density of States

Potentials

EAM: Embedded Atom Method

MEAM: Modified Embedded Atom Method

COMB: Charge Optimized Multi-Body

Equations and Distribution Functions

RDF: Radial Distribution Function g(r)

BADF: Bond Angle Distribution Function $g_3(\theta)$

EOS: Equation of State

Thermodynamic Statistics

P_i: Probability the System Occupies a Microstate i

Z: Partition Function

β: Inverse Temperature Term in the Partition Function

NPT: Thermodynamic Ensemble where the Moles (N), the Pressure (P), and the Temperature (T) are Held Constant

NVT: Thermodynamic Ensemble where the Moles (N), the Volume (V), and the Temperature (T) are Held Constant

Thermodynamic Quantities

C_p: Heat Capacity at Constant Pressure

C_v: Heat Capacity at Constant Volume

α_V: Volumetric Thermal Expansion Coefficient

β_T: Isothermal Compressibility

β_S: Isentropic Compressibility

B_T: Isothermal Bulk Modulus

B_S: Adiabatic Bulk Modulus

γ: Heat Capacity Ratio

γ_i: Activity

γ_e: Electronic Heat Capacity Coefficient

γ_G: Grüneisen Parameter

Crystallography

C_{ij}: Elastic Constants

E_c: Cohesive Energy

E_v^f: Vacancy Formation Energy

E_i^f: Interstitial Formation Energy

Short Range Order

SRO: Short Range Order

σ: Short Range Order Parameter

P_{AA}: Fraction of the Nearest Neighbor Sites of Atom Type A that is occupied by A Type Atoms (Averaged over all A Atoms)

n_A: Atomic Fraction of A Type Atoms in the Entire System

Sensitivity and Uncertainty Analysis

a: Constant multiplier for the symmetric parabola

$S(X_{Zr})$: Shape Function

OAT: One-at-a-Time

REFERENCES

[1] J. Kittel, B. Frost, J. Mustelier, K. Bagley, G. Crittenden, and J. Van Dievoet, *Journal of Nuclear Materials,* vol. 204, pp. 1-13, 1993.

[2] J. Malone, A. Totemeier, N. Shapiro, and S. Vaidyanathan, *Nuclear technology,* vol. 180, pp. 437-442, 2012.

[3] G. L. Hofman, L. C. Walters, and T. H. Bauer, *Progress in Nuclear Energy,* vol. 31, pp. 83-110, 1997.

[4] C. E. Till, Y. I. Chang, and W. H. Hannum, *Progress in Nuclear Energy,* vol. 31, pp. 3-11, 1997.

[5] D. R. Olander, "Fundamental aspects of nuclear reactor fuel elements," California Univ., Berkeley (USA). Dept. of Nuclear Engineering1976.

[6] R. G. Pahl, D. L. Porter, C. E. Lahm, and G. L. Hofman, *Metallurgical Transactions A,* vol. 21, pp. 1863-1870, 1990.

[7] R. Pahl, D. Porter, D. Crawford, and L. Walters, *Journal of Nuclear Materials,* vol. 188, pp. 3-9, 1992.

[8] L. C. Walters, B. Seidel, and J. H. Kittel, *Nuclear Technology,* vol. 65, pp. 179-231, 1984.

[9] W. J. Carmack, D. L. Porter, Y. I. Chang, S. L. Hayes, M. K. Meyer, D. E. Burkes, C. B. Lee, T. Mizuno, F. Delage, and J. Somers, *Journal of Nuclear Materials,* vol. 392, pp. 139-150, 2009.

[10] T. Ogata, M. Kurata, K. Nakamura, A. Itoh, and M. Akabori, *Journal of Nuclear Materials,* vol. 250, pp. 171-175, 1997.

[11] Y. S. Kim, G. Hofman, S. Hayes, and Y. Sohn, *Journal of nuclear materials,* vol. 327, pp. 27-36, 2004.

[12] G. Ondracek and B. Schulz, *Journal of Nuclear Materials,* vol. 46, pp. 253-258, 1973.

[13] B. Blumenthal, *Journal of Nuclear Materials,* vol. 2, pp. 23-30, 1960.

[14] G. Hofman and L. Walters, *Materials Science and Technology: A Comprehensive Treatment* vol. 10. New York: VCH Publishers Inc, 1994.

[15] C. E. Lahm, J. F. Koenig, R. G. Pahl, D. L. Porter, and D. C. Crawford, *Journal of Nuclear Materials,* vol. 204, pp. 119-123, 1993.

[16] D. Summers-Smith, *J. Inst. Metals,* vol. 83, 1955.

[17] J. Huber and P. Ansari, *Physica B+ C*, vol. 135, pp. 441-444, 1985.

[18] M. Akabori, T. Ogawa, A. Itoh, and Y. Morii, *Journal of Physics: Condensed Matter*, vol. 7, p. 8249, 1995.

[19] W. B. Pearson, *A handbook of lattice spacings and structures of metals and alloys*: Pergamon Press, New York, 1967.

[20] G. B. Fedorov and E. A. Smirnov, *Soviet Atomic Energy*, vol. 21, pp. 837-840, 1966.

[21] G. B. Fedorov and E. A. Smirnov, *Soviet Atomic Energy*, vol. 25, pp. 795-797, 1968.

[22] P. Chiotti, V. Akhachinskij, I. Ansara, and M. Rand, "The Chemical Thermodynamics of Actinide Elements and Compounds, part 5, The Actinide Binary Alloys, IAEA, Vienna," STI/PUB/424/51981.

[23] M. Kanno, M. Yamawaki, T. Koyama, and N. Morioka, *Journal of Nuclear Materials*, vol. 154, pp. 154-160, 1988.

[24] Y. A. Shevchuk, E. A. Smirnov, and G. B. Fedorov, *Soviet Atomic Energy*, vol. 71, pp. 642-646, 1991.

[25] L. Leibowitz, R. A. Blomquist, and A. D. Pelton, *Journal of Nuclear Materials*, vol. 167, pp. 76-81, 1989.

[26] W. Xiong, W. Xie, C. Shen, and D. Morgan, *Journal of Nuclear Materials*, vol. 443, pp. 331-341, 2013.

[27] H. Okamoto, *Journal of Phase Equilibria and Diffusion*, vol. 28, pp. 499-500, 2007.

[28] "Thermo-Calc Software AB," in *TCBin/Binary Solutions Database*, ed. Stockholm: Thermo-Calc Software AB, 2013.

[29] B. Sundman, B. Jansson, and J.-O. Andersson, *Calphad*, vol. 9, pp. 153-190, 1985.

[30] A. T. Dinsdale, *Calphad*, vol. 15, pp. 317-425, 1991.

[31] P.-Y. Chevalier, E. Fischer, and B. Cheynet, *Calphad*, vol. 28, pp. 15-40, 2004.

[32] H. L. Yakel, "Review of x-ray diffraction studies in uranium alloys," Oak Ridge National Lab., Tenn.(USA)1973.

[33] F. A. Rough and A. A. Bauer, *Constitution of uranium and thorium alloys*: Battelle Memorial Institute, 1958.

[34] B. W. Howlett, *Journal of Nuclear Materials,* vol. 1, pp. 289-299, 1959.

[35] A. Knapton, *Acta Crystallographica,* vol. 7, pp. 457-458, 1954.

[36] D. Peterson and D. Beernstein, *TRANS. AMER. SOC. METALS,* vol. 52, pp. 763-80, 1960.

[37] R. Rundle and A. Wilson, *Acta Crystallographica,* vol. 2, pp. 148-150, 1949.

[38] E. Boyko, *Acta Crystallographica,* vol. 10, pp. 712-713, 1957.

[39] H. Okamoto, *Journal of Phase Equilibria and Diffusion,* vol. 34, pp. 167-168, 2013.

[40] J. Silcock, "Intermediate Phase In The Uranium-Zirconium System-Discussion," vol. 209, ed: Minerals Metals Materials Soc. 420 Commonwealth Dr, Warrendale, PA 15086, 1957, pp. 521-521.

[41] C. Basak, G. J. Prasad, H. S. Kamath, and N. Prabhu, *Journal of Alloys and Compounds,* vol. 480, pp. 857-862, 2009.

[42] J. McKeown, S. Irukuvarghula, S. Ahn, M. Wall, L. Hsiung, S. McDeavitt, and P. Turchi, *Journal of Nuclear Materials,* vol. 436, pp. 100-104, 2013.

[43] J. Kim, H. Song, H. Kim, K. Kim, C. Lee, and R. S. Fielding, *Journal of Radioanalytical and Nuclear Chemistry,* vol. 299, pp. 103-109, 2014.

[44] G. Lagerberg, *Journal of Nuclear Materials,* vol. 9, pp. 261-276, 1963.

[45] S. Kaity, J. Banerjee, M. R. Nair, K. Ravi, S. Dash, T. R. G. Kutty, A. Kumar, and R. P. Singh, *Journal of Nuclear Materials,* vol. 427, pp. 1-11, 2012.

[46] A. A. Bauer, "An Evaluation of the Properties and Behavior of Zirconium-Uranium Alloys," Battelle Memorial Inst., Columbus, Ohio1959.

[47] F. Rough, "An Evaluation of Data on Zirconium-Uranium Alloys," Battelle Memorial Inst., Columbus, Ohio1955.

[48] M. Akabori, A. Itoh, T. Ogawa, F. Kobayashi, and Y. Suzuki, *Journal of Nuclear Materials,* vol. 188, pp. 249-254, 1992.

[49] A. C. Bagchi, G. J. Prasad, K. B. Khan, and R. P. Singh, *Transactions of the Indian Institute of Metals,* vol. 67, pp. 123-130, 2014.

[50] A. P. Moore, B. Beeler, C. Deo, M. I. Baskes, and M. A. Okuniewski, *Journal of Nuclear Materials,* 2015.

[51] A. Landa, P. Söderlind, and P. E. A. Turchi, *Journal of Alloys and Compounds,* vol. 478, pp. 103-110, 2009.

[52] G. Bozzolo, H. O. Mosca, A. M. Yacout, G. L. Hofman, and Y. S. Kim, *Computational Materials Science,* vol. 50, pp. 447-453, 2010.

[53] G. Bozzolo, H. O. Mosca, A. M. Yacout, and G. L. Hofman, *Journal of Nuclear Materials,* vol. 414, pp. 101-108, 2011.

[54] G. Bozzolo, G. L. Hofman, A. M. Yacout, and H. O. Mosca, *Journal of Nuclear Materials,* vol. 425, pp. 188-192, 2012.

[55] W. Xie, W. Xiong, C. A. Marianetti, and D. Morgan, *Physical Review B,* vol. 88, 2013.

[56] A. P. Moore, B. Beeler, M. Baskes, M. Okuniewski, and C. S. Deo, "Atomistic Ordering in Body Centered Cubic Uranium-Zirconium Alloy," in *MRS Proceedings*, 2013, pp. 27-35.

[57] P. Söderlind, B. Sadigh, V. Lordi, A. Landa, and P. E. A. Turchi, *Journal of Nuclear Materials,* vol. 444, pp. 356-358, 2014.

[58] B. Beeler, C. Deo, M. Baskes, and M. Okuniewski, *Journal of Physics: Condensed Matter,* vol. 24, 2012.

[59] J. R. Fernández and M. I. Pascuet, *Modelling and Simulation in Materials Science and Engineering*, vol. 22, 2014.

[60] R.-S. Li, B. He, and Q.-H. Zhang, *Chinese Journal of Chemical Physics*, vol. 24, pp. 405-411, 2011.

[61] Y. Li, T.-R. Shan, T. Liang, S. B. Sinnott, and S. R. Phillpot, *Journal of Physics: Condensed Matter,* vol. 24, p. 235403, 2012.

[62] M. I. Pascuet, G. Bonny, and J. R. Fernández, *Journal of Nuclear Materials,* vol. 424, pp. 158-163, 2012.

[63] D. Smirnova, S. Starikov, and V. Stegailov, *Journal of Physics: Condensed Matter,* vol. 24, p. 015702, 2012.

[64] D. E. Smirnova, A. Y. Kuksin, S. V. Starikov, V. V. Stegailov, Z. Insepov, J. Rest, and A. M. Yacout, *Modelling and Simulation in Materials Science and Engineering,* vol. 21, p. 035011, 2013.

[65] Y. Li, T. Liang, S. B. Sinnott, and S. R. Phillpot, *Journal of Physics: Condensed Matter,* vol. 25, p. 505401, 2013.

[66] M. Baskes, K. Muralidharan, M. Stan, S. Valone, and F. Cherne, *JOM,* vol. 55, pp. 41-50, 2003.

[67] M. I. Baskes, *Physical Review B,* vol. 62, pp. 15532-15537, 2000.

[68] M. I. Baskes, S. Y. Hu, S. M. Valone, G. F. Wang, and A. C. Lawson, *Journal of Computer-Aided Materials Design,* vol. 14, pp. 379-388, 2007.

[69] M. I. Baskes, A. C. Lawson, and S. M. Valone, *Physical Review B,* vol. 72, p. 014129, 2005.

[70] M. I. Baskes, K. Muralidharan, M. Stan, S. M. Valone, and F. J. Cherne, *JOM,* vol. 55, pp. 41-50, 2003.

[71] L. Berlu, G. Jomard, G. Rosa, and P. Faure, *Journal of Nuclear Materials,* vol. 372, pp. 171-176, 2008.

[72] L. Berlu, G. Jomard, G. Rosa, and P. Faure, *Journal of Nuclear Materials,* vol. 374, pp. 344-353, 2008.

[73] A. Kubota, W. Wolfer, S. Valone, and M. Baskes, *Journal of Computer-Aided Materials Design,* vol. 14, pp. 367-378, 2007.

[74] M. Robinson, S. D. Kenny, R. Smith, M. T. Storr, and E. McGee, *Nuclear Instruments and Methods in Physics Research Section B: Beam Interactions with Materials and Atoms,* vol. 267, pp. 2967-2970, 2009.

[75] S. M. Valone, M. I. Baskes, and R. L. Martin, *Physical Review B,* vol. 73, p. 214209, 2006.

[76] S. M. Valone, M. I. Baskes, and S. P. Rudin, *Journal of Nuclear Materials,* vol. 422, pp. 20-26, 2012.

[77] M. S. Daw and M. I. Baskes, *Physical Review B,* vol. 29, p. 6443, 1984.

[78] M. Baskes, S. M. Foiles, and M. Daw, "Application of the Embedded Atom Method to Interfaces in Metals," in *Materials Science Forum*, 1991, pp. 187-198.

[79] M. I. Baskes, *Physical Review Letters,* vol. 59, pp. 2666-2669, 1987.

[80] S. M. Foiles, *Physical Review B,* vol. 32, pp. 3409-3415, 1985.

[81] R. A. Johnson, *Physical Review B,* vol. 39, pp. 12554-12559, 1989.

[82] X. W. Zhou, H. N. G. Wadley, J. S. Filhol, and M. N. Neurock, *Physical Review B,* vol. 69, p. 035402, 2004.

[83] M. I. Baskes, J. S. Nelson, and A. F. Wright, *Physical Review B,* vol. 40, pp. 6085-6100, 1989.

[84] M. Baskes, *Physical Review B,* vol. 46, p. 2727, 1992.

[85] Z. Cui, F. Gao, Z. Cui, and J. Qu, *Journal of Power Sources,* vol. 207, pp. 150-159, 2012.

[86] H. Deng, W. Hu, X. Shu, L. Zhao, and B. Zhang, *Surface science,* vol. 517, pp. 177-185, 2002.

[87] W.-P. Dong, H.-K. Kim, W.-S. Ko, B.-M. Lee, and B.-J. Lee, *Calphad,* vol. 38, pp. 7-16, 2012.

[88] B. Jelinek, J. Houze, S. Kim, M. Horstemeyer, M. Baskes, and S.-G. Kim, *Physical Review B,* vol. 75, p. 054106, 2007.

[89] H.-K. Kim, W.-S. Jung, and B.-J. Lee, *Acta Materialia,* vol. 57, pp. 3140-3147, 2009.

[90] J. Kim, Y. Koo, and B.-J. Lee, *Journal of Materials Research,* vol. 21, pp. 199-208, 2006.

[91] Y.-M. Kim, N. J. Kim, and B.-J. Lee, *Calphad,* vol. 33, pp. 650-657, 2009.

[92] Y.-M. Kim and B.-J. Lee, *Materials Science and Engineering: A,* vol. 449–451, pp. 733-736, 2007.

[93] Y.-M. Kim and B.-J. Lee, *Journal of Materials Research,* vol. 23, pp. 1095-1104, 2008.

[94] Y.-M. Kim and B.-J. Lee, *Acta Materialia,* vol. 56, pp. 3481-3489, 2008.

[95] Y.-M. Kim, Y.-H. Shin, and B.-J. Lee, *Acta Materialia,* vol. 57, pp. 474-482, 2009.

[96] B.-J. Lee, B. D. Wirth, J.-H. Shim, J. Kwon, S. C. Kwon, and J.-H. Hong, *Physical Review B,* vol. 71, p. 184205, 2005.

[97] J. Luyten, J. De Keyzer, P. Wollants, and C. Creemers, *Calphad,* vol. 33, pp. 370-376, 2009.

[98] J. Luyten, M. Schurmans, C. Creemers, B. S. Bunnik, and G. J. Kramer, *Surface Science,* vol. 601, pp. 2952-2961, 2007.

[99] S. I. Park, B.-J. Lee, and H. M. Lee, *Scripta Materialia,* vol. 45, pp. 495-502, 2001.

[100] I. Sa and B.-J. Lee, *Scripta Materialia,* vol. 59, pp. 595-598, 2008.

[101] T. Sato, K. Saitoh, and N. Shinke, *Materials Science and Engineering: A,* vol. 481–482, pp. 250-253, 2008.

[102] J.-H. Shim, S. I. Park, Y. W. Cho, and B.-J. Lee, *Journal of Materials Research,* vol. 18, pp. 1863-1867, 2003.

[103] H. Wangyu, X. Huaide, S. Xiaolin, Y. Xiaojian, G. Bingxiang, and Z. Bangwei, *Journal of Physics D: Applied Physics,* vol. 33, p. 711, 2000.

[104] W. G. Hoover, *Physical Review A,* vol. 31, p. 1695, 1985.

[105] S. Nosé, *Molecular physics,* vol. 52, pp. 255-268, 1984.

[106] P. E. Blöchl, O. Jepsen, and O. K. Andersen, *Physical Review B,* vol. 49, pp. 16223-16233, 1994.

[107] P. Hohenberg and W. Kohn, *Physical Review,* vol. 136, p. B864, 1964.

[108] W. Kohn and L. J. Sham, *Physical Review,* vol. 140, p. A1133, 1965.

[109] G. Kresse and J. Furthmüller, *Physical Review B,* vol. 54, pp. 11169-11186, 1996.

[110] G. Kresse and D. Joubert, *Physical Review B,* vol. 59, p. 1758, 1999.

[111] J. P. Perdew, K. Burke, and M. Ernzerhof, *Physical Review Letters,* vol. 77, pp. 3865-3868, 1996.

[112] N. Metropolis, A. W. Rosenbluth, M. N. Rosenbluth, A. H. Teller, and E. Teller, *The Journal of Chemical Physics,* vol. 21, pp. 1087-1092, 1953.

[113] G. Wang, M. A. Van Hove, P. N. Ross, and M. I. Baskes, *Progress in surface science,* vol. 79, pp. 28-45, 2005.

[114] J. Bartnick, M. Heinen, A. V. Ivlev, and H. Löwen, *Journal of Physics: Condensed Matter,* vol. 28, p. 025102, 2015.

[115] M. Baskes, "Presentation: Atomistic Models of Metals and Alloys for Nuclear Energy Applications," ed. Georgia Institute of Technology, Atlanta, GA, 2013.

[116] M. S. Daw and M. Baskes, *Physical Review Letters,* vol. 50, pp. 1285-1288, 1983.

[117] M. Born, K. Huang, M. Born, M. Born, and G. Britain, *Dynamical theory of crystal lattices*: Clarendon Press Oxford, 1954.

[118] J. H. Rose, J. R. Smith, and J. Ferrante, *Physical Review B,* vol. 28, p. 1835, 1983.

[119] J. H. Rose, J. R. Smith, F. Guinea, and J. Ferrante, *Physical Review B,* vol. 29, p. 2963, 1984.

[120] M. Baskes, "Title," unpublished|.

[121] B.-J. Lee, M. Baskes, H. Kim, and Y. K. Cho, *Physical Review B,* vol. 64, p. 184102, 2001.

[122] Y. Li, D. J. Siegel, J. B. Adams, and X.-Y. Liu, *Physical Review B,* vol. 67, p. 125101, 2003.

[123] S. Ryu, C. R. Weinberger, M. I. Baskes, and W. Cai, *Modelling and Simulation in Materials Science and Engineering,* vol. 17, p. 075008, 2009.

[124] D. Smirnova, A. Y. Kuksin, S. Starikov, V. Stegailov, Z. Insepov, J. Rest, and A. Yacout, *Modelling and Simulation in Materials Science and Engineering,* vol. 21, p. 035011, 2013.

[125] Z. Cui, F. Gao, Z. Cui, and J. Qu, *Modelling and simulation in materials science and engineering,* vol. 20, p. 015014, 2012.

[126] M. Baskes and R. Johnson, *Modelling and Simulation in Materials Science and Engineering,* vol. 2, p. 147, 1994.

[127] P. Söderlind, *Physical Review B,* vol. 66, p. 085113, 2002.

[128] C.-S. Yoo, H. Cynn, and P. Söderlind, *Physical Review B,* vol. 57, pp. 10359-10362, 1998.

[129] P. Söderlind, L. Nordström, Y. Lou, and B. Johansson, *Physical Review B,* vol. 42, pp. 4544-4552, 1990.

[130] H. Matter, J. Winter, and W. Triftshäuser, *Journal of Nuclear Materials,* vol. 88, pp. 273-278, 1980.

[131] B. Beeler, C. Deo, M. Baskes, and M. Okuniewski, *Journal of Nuclear Materials,* vol. 433, pp. 143-151, 2013.

[132] J. H. Li, Q. B. Ren, C. H. Lu, L. Lu, Y. Dai, and B. X. Liu, *Journal of Alloys and Compounds,* vol. 516, pp. 139-143, 2012.

[133] B. Beeler, B. Good, S. Rashkeev, C. Deo, M. Baskes, and M. Okuniewski, *Journal of Physics: Condensed Matter,* vol. 22, p. 505703, 2010.

[134] S. L. Shang, A. Saengdeejing, Z. G. Mei, D. E. Kim, H. Zhang, S. Ganeshan, Y. Wang, and Z. K. Liu, *Computational Materials Science,* vol. 48, pp. 813-826, 2010.

[135] C. D. Taylor, *Physical Review B,* vol. 77, p. 094119, 2008.

[136] S. Xiang, H. Huang, and L. Hsiung, *Journal of Nuclear Materials,* vol. 375, pp. 113-119, 2008.

[137] J. P. Crocombette, F. Jollet, L. T. Nga, and T. Petit, *Physical Review B,* vol. 64, p. 104107, 2001.

[138] M. Jones, J. Boettger, R. Albers, and D. Singh, *Physical Review B,* vol. 61, p. 4644, 2000.

[139] J. Blomqvist, J. Olofsson, A.-M. Alvarez, and C. Bjerkén. (2012, Structure and Thermodynamical Properties of Zirconium hydrides from first-principle.

[140] B.-T. Wang, P. Zhang, H.-Y. Liu, W.-D. Li, and P. Zhang, *Journal of Applied Physics,* vol. 109, p. 063514, 2011.

[141] W. Zhu, R. Wang, G. Shu, P. Wu, and H. Xiao, *The Journal of Physical Chemistry C,* vol. 114, pp. 22361-22368, 2010.

[142] Y.-J. Hao, L. Zhang, X.-R. Chen, Y.-H. Li, and H.-L. He, *Journal of Physics: Condensed Matter,* vol. 20, p. 235230, 2008.

[143] W. Liu, B. Li, L. Wang, J. Zhang, and Y. Zhao, *Journal of Applied Physics,* vol. 104, pp. 076102-076102-3, 2008.

[144] G. Vérité, F. Willaime, and C. C. Fu, *Solid State Phenomena,* vol. 129, pp. 75-81, 2007.

[145] M. I. Mendelev and G. J. Ackland, *Philosophical Magazine Letters,* vol. 87, pp. 349-359, 2007.

[146] I. Schnell, M. Jones, S. Rudin, and R. Albers, *Physical Review B,* vol. 74, p. 054104, 2006.

[147] Y.-M. Kim, B.-J. Lee, and M. Baskes, *Physical Review B,* vol. 74, p. 014101, 2006.

[148] Y. Zhao, J. Zhang, C. Pantea, J. Qian, L. L. Daemen, P. A. Rigg, R. S. Hixson, G. T. Gray III, Y. Yang, and L. Wang, *Physical Review B,* vol. 71, p. 184119, 2005.

[149] C. Greeff, *Modelling and Simulation in Materials Science and Engineering,* vol. 13, p. 1015, 2005.

[150] H. Ikehata, N. Nagasako, T. Furuta, A. Fukumoto, K. Miwa, and T. Saito, *Physical Review B,* vol. 70, p. 174113, 2004.

[151] C. Domain, R. Besson, and A. Legris, *Acta Materialia,* vol. 50, pp. 3513-3526, 2002.

[152] E. Clouet, J.-M. Sanchez, and C. Sigli, *Physical Review B,* vol. 65, p. 094105, 2002.

[153] S. Yamanaka, K. Yamada, K. Kurosaki, M. Uno, K. Takeda, H. Anada, T. Matsuda, and S. Kobayashi, *Journal of Alloys and Compounds,* vol. 330–332, pp. 99-104, 2002.

[154] R. Pasianot and A. Monti, *Journal of Nuclear Materials,* vol. 264, pp. 198-205, 1999.

[155] L. Fast, J. Wills, B. Johansson, and O. Eriksson, *Physical Review B,* vol. 51, p. 17431, 1995.

[156] F. Cleri and V. Rosato, *Physical Review B,* vol. 48, p. 22, 1993.

[157] S. Wei and M. Chou, *Physical Review Letters,* vol. 69, p. 2799, 1992.

[158] F. Willaime and C. Massobrio, *Physical Review B,* vol. 43, p. 11653, 1991.

[159] D. J. Oh and R. A. Johnson, *Journal of Nuclear Materials,* vol. 169, pp. 5-8, 1989.

[160] E. Brandes, *Smithells metals reference book,* 6 ed. London, Butterworths, 1983.

[161] H. King, *Journal of Phase Equilibria,* vol. 3, pp. 276-276, 1982.

[162] H. R. F., *The elastic constants of crystals and other anisotropic materials*. Springer-Verlag, Berlin: K.-H. Hellwege, A.M. Hellwege (Eds.), 1979.

[163] J. Jamieson and O. C, *High Temperatures-High Pressures,* vol. 5, pp. 123-131, 1973.

[164] S. Vaidya and G. Kennedy, *Journal of Physics and Chemistry of Solids,* vol. 33, pp. 1377-1389, 1972.

[165] C. S. Menon and R. R. Rao, *Journal of Physics and Chemistry of Solids,* vol. 33, pp. 1325-1334, 1972.

[166] H. Bezdek, R. Schmunk, and L. Finegold, *Physica Status Solidi (b),* vol. 42, pp. 275-280, 1970.

[167] E. S. Fisher, M. H. Manghnani, and T. J. Sokolowski, *Journal of Applied Physics,* vol. 41, pp. 2991-2998, 1970.

[168] S. Allard, *Metals, thermal and mechanical data* vol. 16: Pergamon Press, 1969.

[169] E. S. Fisher and C. J. Renken, *Physical Review,* vol. 135, pp. A482-A494, 1964.

[170] R. Ahuja, J. M. Wills, B. Johansson, and O. Eriksson, *Physical Review B,* vol. 48, pp. 16269-16279, 1993.

[171] A. Heiming, W. Petry, J. Trampenau, M. Alba, C. Herzig, H. Schober, and G. Vogl, *Physical Review B,* vol. 43, p. 10948, 1991.

[172] H. Wen and C. Woo, *Journal of Nuclear Materials,* vol. 420, pp. 362-369, 2012.

[173] M. I. Mendelev and B. S. Bokstein, *Philosophical Magazine,* vol. 90, pp. 637-654, 2010.

[174] C. Woo and X. Liu, *Philosophical Magazine,* vol. 87, pp. 2355-2369, 2007.

[175] C. Domain and A. Legris, *Philosophical Magazine,* vol. 85, pp. 569-575, 2005.

[176] O. Le Bacq, F. Willaime, and A. Pasturel, *Physical Review B,* vol. 59, pp. 8508-8515, 1999.

[177] G. M. Hood, *Journal of Nuclear Materials,* vol. 159, pp. 149-175, 1988.

[178] T. Frolov and Y. Mishin, *The Journal of Chemical Physics,* vol. 131, p. 054702, 2009.

[179] M. Bauccio, *ASM metals reference book*. Materials Park OH: ASM international, 1993.

[180] W. G. Rohr and L. J. Wittenberg, *The Journal of Physical Chemistry,* vol. 74, pp. 1151-1152, 1970.

[181] A. Efimov, L. Belorukova, and I. Vasilkova, *Svoistva Neorganicheskih Soedinenii (in Russian)*. Leningrad: Himiia, 1983.

[182] L. S. Levinson, *The Journal of Chemical Physics,* vol. 40, pp. 3584-3585, 1964.

[183] H. Savage and R. D. Seibel, "Heat Capacity Studies of Uranium and Uranium-Fissium Alloys," Argonne National Lab., Ill.; Denver. Univ. Denver Research inst.1963.

[184] M. H. Rand and O. Kubaschewski, "The Thermochemical Properties of Uranium Compounds," ed Vienna: Oliver and Boyd Ltd., 1963, p. 70.

[185] D. Marchidan and M. Ciopec, *The Journal of Chemical Thermodynamics,* vol. 8, pp. 691-701, 1976.

[186] K. K. Kelley, *US Bur. Mines Bull.,* vol. 584, 1960.

[187] H. Stephens, "Determination of the enthalpy of liquid copper and uranium with a liquid argon calorimeter," Sandia Labs., Albuquerque, NM1974.

[188] E. Stull and G. Sinke, *Thermal Properties of the Elements*. Washington, DC: ACS, 1956.

[189] R. Hultgren, P. D. Desai, D. T. Hawkins, M. Gleiser, K. K. Kelley, and D. D. Wagman, *Selected Values of the Thermodynamic Properties of the Elements*. Metals Park, Ohio, 1973.

[190] E. G. Rauh and R. J. Thorn, *The Journal of Chemical Physics,* vol. 22, pp. 1414-1420, 1954.

[191] A. Radenac and C. Berthaut, *High Temp. - High Pressures,* vol. 4, pp. 485-491, 1972.

[192] A. F. Guillermet, *International Journal of Thermophysics,* vol. 8, pp. 751-761, 1987.

[193] J. W. Arblaster, *Calphad,* vol. 43, pp. 32-39, 2013.

[194] S. A. Katz, V. Y. Chekhovskoi, and M. D. Kovalenko, *Teplofiz. Vys. Temp.,* vol. 23, 1985.

[195] S. Klein, D. Holland-Moritz, and D. M. Herlach, *Physical Review B,* vol. 80, p. 212202, 2009.

[196] F. J. Mompean, J. Perrone, and M. Illemassène, *Chemical thermodynamics of zirconium* vol. 8: Gulf Professional Publishing, 2005.

[197] C. B. Alcock, S. Zador, K. Jacob, O. V. Goldbeck, H. Nowothy, K. Seifert, and O. Kubaschewski, *Zirconium: Physico chemical properties of its compounds and alloys*. Vienna: International Atomic Energy Agency, 1976.

[198] C. Brunner, C. Cagran, A. Seifter, and G. Pottlacher, "Temperature—its measurement and control in science and industry," in *AIP Conference*, 2003, pp. 771–776.

[199] M. Rösner-Kuhn, K. Drewes, H. Franz, and M. G. Frohberg, *Journal of Alloys and Compounds,* vol. 316, pp. 175-178, 2001.

[200] M. M. Martynyuk and V. I. Tsapkov, *Fiz. Tverd. Tela,* vol. 14, pp. 1806–1807, 1972.

[201] V. N. Korobenko, A. I. Savvatimski, and K. K. Sevostyanov, *High Temperatures High Pressures(UK),* vol. 33, pp. 647-658, 2001.

[202] V. I. Elyutin, M. A. Maurakh, and G. M. Sverdlov, *Izvest. Vyssh. Uchebn. Zaved. Tsvetnaya Metall.,* vol. 2, pp. 87–88, 1967.

[203] M. W. Chase and J. A. N. A. Force, *NIST-JANAF thermochemical tables*. Washington, DC: American Chemical Society, 1998.

[204] R. Hultgren, R. L. Orr, P. D. Anderson, and K. K. Kelley, *Selected Values of Thermodynamic Properties of Metals and Alloys*. Berkeley, California: University of California, Lawrence Radiation Laboratory, 1967.

[205] V. N. Korobenko and A. I. Savvatimski, *High Temp.*, vol. 29, pp. 693–696, 1991.

[206] J. Crangle and J. Temporal, *Journal of Physics F: Metal Physics,* vol. 3, p. 1097, 1973.

[207] J. C. Ho, N. E. Phillips, and T. Smith, *Physical Review Letters,* vol. 17, p. 694, 1966.

[208] L. Schachinger and I. Lamprecht, *Thermochimica Acta,* vol. 151, pp. 203-217, 1989.

[209] M. Mortimer, *Le Journal de Physique Colloques,* vol. 40, pp. C4-124-C4-129, 1979.

[210] S. D. Bader, N. E. Phillips, and E. S. Fisher, *Physical Review B,* vol. 12, pp. 4929-4940, 1975.

[211] C. W. Dempesey and J. E. Gordon, *Phys. Rev. Letters,* vol. 11, p. 547, 1963.

[212] H. E. Flotow and D. W. Osborne, *Physical Review,* vol. 151, pp. 564-570, 1966.

[213] B. B. Goodman, J. Hilliaret, J. J. Veyssie, and L. Weil, in *Proc. of Seventh Int. Conf. on Low Temperature Physics*, Toronto, 1960.

[214] J. Gordon, H. Montgomery, R. Noer, G. Pickett, and R. Tobón, *Physical Review,* vol. 152, p. 432, 1966.

[215] G. R. Stewart, *Review of Scientific Instruments,* vol. 54, pp. 1-11, 1983.

[216] M. Shimizu and A. Katsuki, *Journal of the Physical Society of Japan,* vol. 19, pp. 1856-1861, 1964.

[217] C. Stassis, J. Zarestky, D. Arch, O. D. McMasters, and B. N. Harmon, *Physical Review B,* vol. 18, pp. 2632-2642, 1978.

[218] C. Holley and E. Storms, "Thermodynamics of nuclear materials," in *Proc. IAEA Symp.(50th Ed.), IAEA, Vienna*, 1968, p. 397.

[219] D. C. Ginnings and R. Corruccini, *J. Res. Nat. Bur. Stand,* vol. 39, pp. 309-316, 1947.

[220] R. N. R. Mulford and R. I. Sheldon, *Journal of Nuclear Materials,* vol. 154, pp. 268-275, 1988.

[221] J.-I. Nakamura, Y. Takahashi, S.-I. Izumi, and M. Kanno, *Journal of Nuclear Materials,* vol. 88, pp. 64-72, 1980.

[222] G. E. Moore and K. K. Kelley, *Journal of the American Chemical Society,* vol. 69, pp. 2105-2107, 1947.

[223] I. Barin, *Thermochemical Data of Pure Substances*, 3rd ed. vol. 2. Weinheim ; New York: Wiley-VCH, 1995.

[224] J. North, "A High Temperature Adiabatic Calorimeter The Specific Heat of Uranium between 100 and 800C," Atomic Energy Research Establishment, Harwell, Berks (England)1952.

[225] J. P. Coughlin and E. G. King, *Journal of the American Chemical Society,* vol. 72, pp. 2262-2265, 1950.

[226] G. B. Skinner and H. L. Johnston, *Journal of the American Chemical Society,* vol. 73, pp. 4549-4550, 1951.

[227] A. Cezairliyan and F. Righini, *National Bureau of Standards,* vol. 79A, pp. 81-84, 1974.

[228] M. Murabayashi, S. Tanaka, and Y. Takahashi, *Journal of Nuclear Science and Technology,* vol. 12, pp. 661-662, 1975.

[229] P.-F. Paradis and W.-K. Rhim, *Journal of Materials Research,* vol. 14, pp. 3713-3719, 1999.

[230] V. N. Korobenko and A. I. Savvatimskii, *High Temperature,* vol. 39, pp. 659-665, 2001.

[231] B. Guo, G. Teodorescu, R. Overfelt, and P. Jones, *International Journal of Thermophysics,* vol. 29, pp. 1997-2005, 2008.

[232] I. Petrova, V. Peletskii, and B. Samsonov, *High Temperature,* vol. 38, pp. 560-565, 2000.

[233] J. L. Scott, "A Calorimetric Investigation of Zirconium, Titanium, and Zirconium Alloys from 60 to 960° C," Oak Ridge National Lab., Tenn. ORNL-2328, 1957.

[234] T. B. Douglas and A. C. Victor, *J. Res. Natl. Bur. Stand,* vol. 61, pp. 13-23, 1958.

[235] T. B. Douglas, *J. Res. Natl. Bur. Std.*, vol. 67, 1963.

[236] I. Fieldhouse and J. Lang, "Measurement of thermal properties," Armour Research Foundation, Chicago IL WADD-TR-60-904, 1961.

[237] L. V. Gurvich, *Thermodynamical Properties of Elements* vol. 2. Nauka, Moscow, 1962.

[238] O. Vollmer, M. Braun, and R. Kohlhaas, *Z. Naturforsch,* vol. 22A, 1967.

[239] V. E. Zinovyev, in *Metallurgia,* ed. Nauka, Moscow, 1989.

[240] J. Fink and L. Leibowitz, *Journal of Nuclear Materials,* vol. 226, pp. 44-50, 1995.

[241] N. Milošević and K. Maglić, *International journal of thermophysics,* vol. 27, pp. 1140-1159, 2006.

[242] N. D. Milošević and K. D. Maglić, *International Journal of Thermophysics,* vol. 27, pp. 1140-1159, 2006.

[243] L. Filippov and R. Yurchak, *Journal of Engineering Physics and Thermophysics,* vol. 21, pp. 1209-1220, 1971.

[244] R. Redmond and J. Lones, "Enthalpies and heat capacities of stainless steel (316), zirconium, and lithium at elevated temperatures," Oak Ridge National Lab. ORNL-1342, 1952.

[245] R. Q. Hood, L. Yang, and J. A. Moriarty, *Physical Review B,* vol. 78, p. 024116, 2008.

[246] G. Kresse and J. Hafner, *Physical Review B,* vol. 47, p. 558, 1993.

[247] J. Thewlis, *Nature,* vol. 168, pp. 198-199, 1951.

[248] A. Wilson and R. Rundle, *Acta Crystallographica,* vol. 2, pp. 126-127, 1949.

[249] R. I. Sheldon and D. E. Peterson, *Bulletin of Alloy Phase Diagrams,* vol. 10, pp. 165-171, 1989.

[250] C. B. Basak, N. Prabhu, and M. Krishnan, *Intermetallics,* vol. 18, pp. 1707-1712, 2010.

[251] P. Chiotti, H. Klepfer, and R. White, *Trans. Am. Soc. Met,* vol. 51, pp. 772-782, 1959.

[252] W. Pearson, *Lattice spacings and structures of metals and alloys* vol. 884: Pergamon, Oxford, 1958.

[253] C. B. Basak, *Journal of Nuclear Materials,* vol. 416, pp. 280-287, 2011.

[254] C. Basak, R. Keswani, G. J. Prasad, H. S. Kamath, N. Prabhu, and S. Banerjee, *Journal of Nuclear Materials,* vol. 393, pp. 146-152, 2009.

[255] C. Basak, S. Neogy, D. Srivastava, G. Dey, and S. Banerjee, *Philosophical Magazine,* vol. 91, pp. 3290-3306, 2011.

[256] W. D. Wilkinson, *Uranium Metallurgy: Uranium corrosion and alloys* vol. 2: Interscience Publishers, 1962.

[257] V. Korobenko, M. Agranat, S. Ashitkov, and A. Savvatimskiy, *International Journal of Thermophysics,* vol. 23, pp. 307-318, 2002.

[258] G. B. Skinner and H. L. Johnston, *The Journal of Chemical Physics,* vol. 21, pp. 1383-1384, 1953.

[259] H. Chiswik, A. Dwight, L. Lloyd, M. Nevitt, and S. Zegler, "Advances in the physical metallurgy of uranium and its alloys," Argonne National Lab., Lemont, Ill. A/CONF. 15/P/713, 1958.

[260] F. Heiniger, E. Bucher, and J. Muller, *Physik der Kondensierten Materie,* vol. 5, pp. 243-284, 1966.

[261] Y. Takahashi, K. Yamamoto, T. Ohsato, H. Shimada, T. Terai, and M. Yamawaki, *Journal of Nuclear Materials,* vol. 167, pp. 147-151, 1989.

[262] T. Matsui, T. Natsume, and K. Naito, *Journal of Nuclear Materials,* vol. 167, pp. 152-159, 1989.

[263] B.-H. Lee, J.-S. Cheon, Y.-H. Koo, J.-Y. Oh, J.-S. Yim, D.-S. Sohn, M. Baryshnikov, and A. Gaiduchenko, *Journal of Nuclear Materials,* vol. 360, pp. 315-320, 2007.

[264] S. Dash, K. Ghoshal, and T. R. G. Kutty, *Journal of Thermal Analysis and Calorimetry,* vol. 112, pp. 179-185, 2013.

[265] C. H. Lupis, *Elsevier Science Publishing Co., Inc., 1983,* p. 581, 1983.

[266] M. Boivineau, L. Arlès, J. M. Vermeulen, and T. Thévenin, *Physica B: Condensed Matter,* vol. 190, pp. 31-39, 1993.

[267] J. Goldak, L. Lloyd, and C. Barrett, *Physical Review,* vol. 144, p. 478, 1966.

[268] Y. Nie and Y. Xie, *Physical Review B,* vol. 75, p. 174117, 2007.

[269] P. Söderlind, A. Landa, and P. E. A. Turchi, *Physical Review B,* vol. 90, p. 157101, 2014.

[270] M. Kurata, *IOP Conference Series: Materials Science and Engineering,* vol. 9, p. 012022, 2010.

[271] N. Saunders and A. P. Miodownik, *CALPHAD (Calculation of Phase Diagrams) A Comprehensive Guide* vol. 1: Elsevier, 1998.

[272] R. C. Albers, *Nature,* vol. 410, pp. 759-761, 2001.

[273] C. H. Booth, Y. Jiang, D. L. Wang, J. N. Mitchell, P. H. Tobash, E. D. Bauer, M. A. Wall, P. G. Allen, D. Sokaras, D. Nordlund, T.-C. Weng, M. A. Torrez, and J. L. Sarrao, *Proceedings of the National Academy of Sciences,* vol. 109, pp. 10205-10209, 2012.

[274] B. Johansson, *Physical Review B,* vol. 11, pp. 2740-2743, 1975.

[275] A. N. Yaresko, V. N. Antonov, and P. Fulde, *Physical Review B,* vol. 67, p. 155103, 2003.

[276] J. M. Sanchez, F. Ducastelle, and D. Gratias, *Physica A: Statistical Mechanics and its Applications,* vol. 128, pp. 334-350, 1984.

[277] J. Cowley, *Journal of Applied Physics,* vol. 21, pp. 24-30, 1950.

[278] F. Ducastelle and F. Ducastelle, *Order and phase stability in alloys*: North-Holland Amsterdam, 1991.

[279] C. Deo and D. Srolovitz, *Physical Review B,* vol. 63, p. 165411, 2001.

[280] C.-T. Lee, J.-H. Park, T.-K. Kim, U.-J. Lee, B.-S. Lee, and D.-S. Sohn, *Journal of Nuclear Materials,* vol. 373, pp. 275-279, 2008.

[281] M. Kasnan, *Applied Mechanics and Materials,* vol. 376, pp. 23-29, 2013.

[282] B.-J. Lee, *Calphad,* vol. 31, pp. 95-104, 2007.

[283] B.-J. Lee, J.-H. Shim, and M. Baskes, *Physical Review B,* vol. 68, p. 144112, 2003.

[284] B.-J. Lee and M. Baskes, *Physical Review B,* vol. 62, p. 8564, 2000.

[285] A. Saltelli, M. Ratto, T. Andres, F. Campolongo, J. Cariboni, D. Gatelli, M. Saisana, and S. Tarantola, *Global sensitivity analysis: the primer*: John Wiley & Sons, 2008.

[286] L. Vočadlo, D. P. Dobson, and I. G. Wood, *Earth and Planetary Science Letters,* vol. 288, pp. 534-538, 2009.